Development of a Realistic Event Generator for In-Medium and QGP Dileptons

Entwicklung eines realistischen Event-Generators für In-Medium und QGP Dileptonen

Master-Thesis von Florian Seck

October 2015

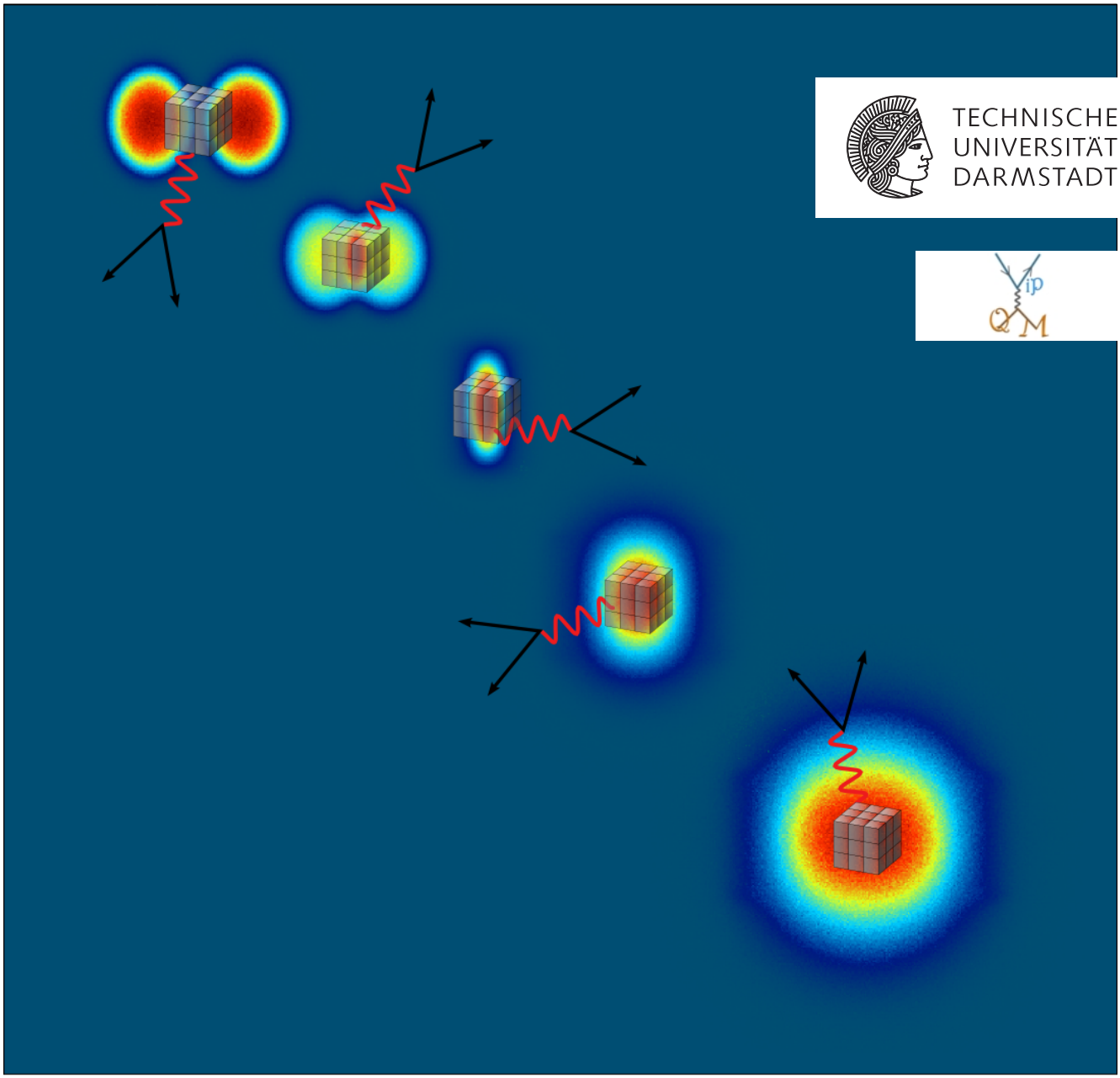

TECHNISCHE UNIVERSITÄT DARMSTADT

Development of a Realistic Event Generator for In-Medium and QGP Dileptons
Entwicklung eines realistischen Event-Generators für In-Medium und QGP Dileptonen

Vorgelegte Master-Thesis von Florian Seck

1. Gutachten: Prof. Dr. Tetyana Galatyuk
2. Gutachten: Prof. Dr. Joachim Stroth

Tag der Einreichung:

Abstract

Heavy-ion collisions at relativistic and ultra-relativistic energies provide the intriguing opportunity to create hot and dense nuclear or quark matter in the laboratory. Experiments studying heavy-ion collisions are the only possibility on earth to explore strongly interacting matter under conditions similar to those realized a few microseconds after the “Big Bang”, or still existing today in the interior of compact stellar objects. The aim is to explore unknown territories in the phase diagram of strongly interacting matter and to understand the microscopic structure of the matter under extreme conditions. Dileptons are a special tool in this respect, as their interaction rate is small enough to let them escape from the strongly interacting interior of the collision zone and carry invaluable information in form of their invariant mass to the detector.

As dileptons are radiated from all stages of a heavy-ion collision a realistic modeling of the space-time evolution is mandatory. In this work a coarse-graining approach is used to convert hadronic transport simulations of heavy-ion events in the SIS to SPS energy range into local temperature and baryon densities. These serve as input parameters to the Rapp-Wambach in-medium ρ meson spectral function which describes the available experimental data accurately. Before one can calculate the thermal dilepton emission, the degree of thermalization inside the system has to be checked. Then one can determine the local temperature, baryon density and pion chemical potential. The resulting dilepton spectra are implemented into the event generator Pluto which in turn enables a fast sampling of dilepton masses and momenta according to the spectra calculated in this work.

The final goal of this thesis is to provide an easy to use framework in which the users can pick a collision system of interest and simulate the contribution of thermal radiation from in-medium ρ mesons and the QGP to their spectra.

Besides that, several insights related to the lifetime of the fireball and the use of dileptons as a fireball thermometer have emerged over the course of this thesis and will be presented.

The thesis is structured as following: chapter 1 will give a general introduction into the exciting topic of relativistic heavy-ion physics and electromagnetic probes in particular. In chapter 2 various tools needed for the simulations and different models to describe the fireball evolution will be discussed. In addition the theoretical approach to calculate the dilepton emission is introduced. Chapter 3 will focus on the specific methods used in this thesis to coarse-grain the transport events and determine the input parameters of the thermal emission rates. At the end of that chapter the calculation of different dilepton spectra in this approach and their implementation into Pluto will be explained. In chapter 4 the additional insights which emerged during this work will be discussed, while chapter 5 gives a short summary and an outlook.

Zusammenfassung

Kollisionen zweier schwerer Atomkerne bei relativistischen und ultra-relativistischen Energien bieten die faszinierende Möglichkeit heiße und dichte Kern- oder Quarkmaterie im Labor zu erzeugen. Experimente zur Untersuchung von Schwerionenkollisionen stellen die einzige Gelegenheit auf der Erde dar die stark wechselwirkende Materie unter ähnlichen Bedingungen zu untersuchen, wie sie wenige Mikrosekunden nach dem „Big Bang“ vorherrschten oder noch heute im Inneren von Neutronensternen existieren. Ziel ist die Erschließung der bisher unerforschten Regionen im Phasendiagramm stark wechselwirkender Materie und das Verständnis der mikroskopischen Struktur der Materie unter solch extremen Bedingungen. Dileptonen stellen in dieser Hinsicht ein besonderes Hilfsmittel dar. Ihre Wechselwirkungsrate ist so klein, dass sie ohne weitere Streuung aus dem Inneren des Feuerballs entkommen können. Dabei tragen sie mit ihrer invarianten Masse wertvolle Information aus dem Feuerball zum Detektor.

Da Dileptonen während des kompletten zeitlichen Verlaufs einer Schwerionenkollision abgestrahlt werden, ist eine realistische Modellierung der Feuerball Raum-Zeit Evolution unerlässlich. In dieser Arbeit wird von einem „coarse-graining“- Ansatz (zu deutsch etwa „Grob-Körnung“) Gebrauch gemacht. Hadronische Transport-Simulationen von Schwerionenkollisionen bei Energien im Bereich von SIS zu SPS werden dabei in lokale Größen wie Temperatur und baryonische Dichte übersetzt, welche wiederum als Parameter in die Rapp-Wambach In-Medium ρ Meson Spektralfunktion eingehen. Diese Funktion bietet eine gute Beschreibung der bisher veröffentlichten experimentellen Daten.

Vor der Berechnung der thermischen Dileptonen-Emission muss überprüft werden, ob das System bereits im thermischen Gleichgewicht ist. Dann können die Temperatur, die baryonische Dichte und das chemische Potential der Pionen bestimmt werden. Die daraus resultierenden Dileptonen-Spektren können in den Event-Generator Pluto als Plug-in eingefügt werden, wodurch schnelle Simulationen von Dileptonen möglich sind. Die Massen und Impulse werden dabei gemäß der berechneten Spektren zufällig an die einzelnen Lepton-Paare verteilt.

Das Ziel dieser Arbeit ist die Entwicklung eines Software-Pakets, das es den Benutzern ermöglicht für ein Kollisionssystem ihrer Wahl die Beiträge thermischer Strahlungsquellen (Zerfälle von ρ Meson im Medium und QGP-Strahlung) in ihre Spektren einzufügen.

Desweiteren haben sich im Laufe der Arbeit am Event-Generator für Dileptonen aus dem heißen und dichten Medium neue Einsichten bezüglich der Lebensdauer des Feuerballs bei niedrigen Kollisionsenergien und zum Gebrauch von Dileptonen als Feuerball-Thermometer ergeben. Diese werden ebenfalls erläutert.

Diese Arbeit ist folgendermaßen strukturiert: Kapitel 1 gibt eine allgemeine Einführung in die spannende Physik mit relativistischen Schwerionen. Ein besonderer Fokus liegt dabei auf den elektromagnetischen Feuerballsonden. In Kapitel 2 werden einige Hilfsmittel zur Simulation und verschiedene Modelle zur Beschreibung der Feuerball-Evolution vorgestellt. Außerdem wird der theoretische Zugang zur Berechnung der Dileptonen-Emission präsentiert. In Kapitel 3 werden die einzelnen Schritte und Methoden dargestellt, die in dieser Arbeit im „Coarse-Graining“-Ansatz und zur Bestimmung der Parameter für die thermischen Emissionsraten genutzt wurden. Am Ende des Kapitels wird erklärt, wie verschiedene differentielle Spektren mit Hilfe dieses Ansatzes berechnet werden können. Außerdem wird die Eingliederung der resultierenden Spektren in den Event-Generator Pluto erläutert. Kapitel 4 ist den neuen Einsichten zur Lebensdauer des Feuerballs gewidmet. Schließlich gibt Kapitel 5 eine kurze Zusammenfassung und einen Ausblick.

Contents

1 Introduction[1]

The quest for the elementary building blocks of matter and the discovery of fundamental laws which describe the interactions between them has always been a central source of inspiration for physicists. A huge progress in our understanding was achieved in the 20th century with the development of General Relativity and the emergence of the Standard Model of particle physics. While the former describes the gravitational force as curvature of space-time, the latter deals with the other three known forces, namely electromagnetism, the weak and the strong nuclear interaction. These forces are mediated by vector bosons[2] with the photon (γ) being the force carrier of electromagnetism, while gluons (g) transmit the strong interaction. The Standard Model contains in addition 12 different fermions[3] and their anti-particles which can be subdivided into leptons and quarks. Only the latter interact also via the strong force, since they carry "color" as the charge of the strong interaction. The color charge which represents a three-valued degree of freedom is in analogy to the three primary colors of light usually labeled red, green and blue. In addition the Standard Model includes the recently discovered Higgs boson [7, 8] whose underlying quantum field is supposed to give mass to elementary particles. Figure 1.1 shows an overview of the Standard Model particles and some of their properties.

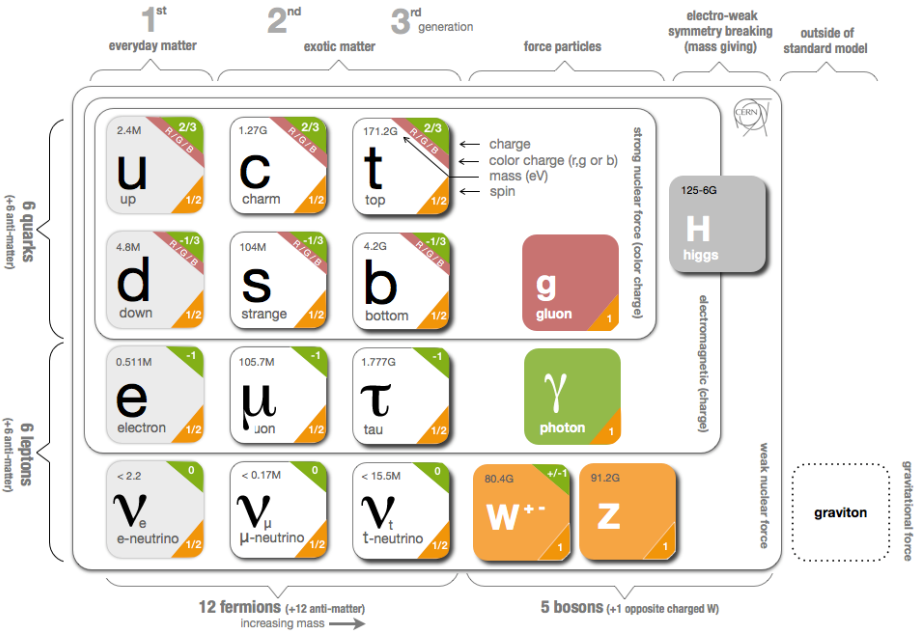

Figure 1.1: Overview of the particles described by the Standard Model of particle physics [9].

Of no less interest for the advance of physics is the formation of the complex structures and phases of matter existing in our cosmos at all scales. The aim of nuclear physics is the exploration of strongly interacting matter which accounts for 99,9% of all mass in the visible universe. Nowadays it is most commonly contained as nucleons inside atomic nuclei. However microseconds after the Big Bang, the early universe was presumably filled with a soup of quarks and gluons which condensed into the ordinary matter found today as the universe expanded and cooled down. Furthermore, the interior of compact stars may consist of extremely dense packed nuclear matter. Colliding heavy ions with each other at relativistic or ultra-relativistic[4] energies might provide a fascinating opportunity to create such exotic forms of matter in the laboratory and study them in detail.

1 As not stated otherwise, the information in this chapter is extracted from [1–6].
2 Particles with total spin 1 and odd parity (commonly noted as $J^P = 1^-$).
3 Particles with spin $\frac{1}{2}$.
4 Ultra-relativistic beam energies: $E_{lab} \gg m_N$.

1.1 Quantum Chromodynamics and its Properties

Quantum chromodynamics (QCD) is the commonly accepted and (in high energetic scattering experiments) well tested theory describing the part of the Standard Model related to the strong force. The basic equation defining the dynamics of particles carrying color charge and the interactions among them is given by the QCD-Lagrangian

$$\mathcal{L}_{QCD} = \sum_{q=u,d,s,c,b,t} \bar{q}\left(i\gamma^{\mu}D_{\mu} - \mathcal{M}_q\right)q - \frac{1}{4}G^a_{\mu\nu}G^{\mu\nu}_a. \tag{1.1}$$

The first term involving the covariant derivative $D_\mu = \partial_\mu - ig\frac{\lambda_a}{2}A^a_\mu$ accounts for the dynamics of quarks (q) and their interactions with gluon (A^a_μ) fields. The second term contains the gluon field strength tensor

$$G^a_{\mu\nu} = \partial_\mu A^a_\nu - \partial_\nu A^a_\mu + g f^{abc} A^b_\mu A^c_\nu \tag{1.2}$$

and determines the gluon dynamics as well as their possibility to interact with other gluons. This feature is expressed in the last part of $G^a_{\mu\nu}$ and due to the fact that gluons carry also the color charge. The Lagrangian of quantum electrodynamics (QED) as the part of the Standard Model describing the electromagnetism has a very similar mathematical form. However, photons carry no electric charge and the structure constants f^{abc} vanish[5], rendering self-interactions of photons impossible.

A remarkable property of QCD is the running coupling $\alpha_S = \frac{g^2}{4\pi}$ which is shown in Figure 1.2.

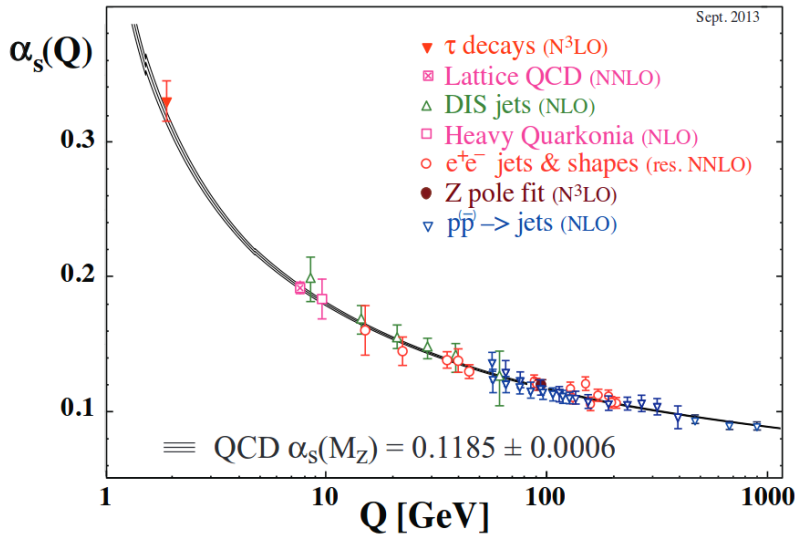

Figure 1.2: Summary of measurements of α_S as a function of the energy scale Q [10].

It decreases as the momentum which is transfered in a scattering rises. The momentum transfer is directly linked to the spacial resolution probed in the reaction. Thus, the coupling becomes small at short distances and perturbation theory can be used to make quantitative predictions which can be tested in scattering experiments at high energy. At low momentum transfer, however, the coupling α_S increases and gets so large that non-perturbative phenomena become dominant.

The force between two colored particles does not get weaker as the distance between them is increased, so that quarks cannot appear in isolation[6]. They are confined into color-neutral hadrons: baryons, e.g., protons and neutrons consist of 3 quarks (combining all three colors), while meson, e.g., pions and kaons are build up of a quark-antiquark pair (compensating color with “anti-color”). The fact that gluons carry color and interact with each other is presumably the source of the confinement, while the decrease of α_S at high collision energies allows quarks to become asymptotically free.

[5] The structure constants are determined by the underlying group structure of the theory. The symmetry group of QED is $U(1)$, while QCD has the $SU(3)$ symmetry.

[6] If one tries to separate two quarks, one has to invest so much energy that at some point a new quark-antiquark pair is created between them.

Another key feature of QCD is the dynamic generation of hadron masses. The bare masses of the up (u) and down (d) quarks[7] account only for about two percent of the mass of a nucleon[8]. Moreover, the spectrum of hadronic states starts after a gap of roughly 1 GeV with the exception of the abnormally light pions that carry a mass of $m_\pi \sim 140\,\mathrm{MeV/c^2}$. The small masses of the u and d quarks lead to an approximate invariance of QCD under certain transformations, called chiral symmetry[9]. Hadrons composed of these light quarks come in chiral pairs which convert into each other when the chiral transformations are applied. If this symmetry would be realized in nature, one would expect these partners to exhibit nearly identical mass distributions. In nature, however, one finds a large mass difference $\Delta M \sim 500\,\mathrm{MeV/c^2}$ between them: the mass of, e.g., the ρ-meson is $m_\rho = 770\,\mathrm{MeV/c^2}$, while its chiral partner, the a_1-meson, has a much larger mass of $m_{a_1} = 1260\,\mathrm{MeV/c^2}$. Another example is the nucleon with a mass of $m_N = 940\,\mathrm{MeV/c^2}$ and its chiral partner $N^*(1535)$.

This is presumably due to a condensate of quark-antiquark pairs, the so called "chiral condensate" $\langle\bar{q}q\rangle$ which fills the QCD vacuum and causes the spontaneous breaking of chiral symmetry ($SB\chi B$). An analogy for this spontaneous symmetry breaking is given by a ferromagnet in the absence of an external magnetic field. As long as it is heated above the Curie temperature, the spins point in no preferred direction and the system is rotationally symmetric. When the ferromagnet is, however, cooled below the critical point, little fluctuations cause the spins to align each other along an arbitrary direction and the rotational symmetry is spontaneously broken. The realization of a particular state breaks the symmetry, but the underlying Hamiltonian is still invariant under rotations.

The chiral condensate can not be measured directly, but the spontaneous breaking of chiral symmetry ($SB\chi B$) leaves its traces in the hadron spectrum, namely the mass splitting between chiral pairs and the existence of massless Goldstone bosons which can be identified with the nearly massless pions. Their finite mass is due to the explicit breaking of chiral symmetry by the small but finite masses of the up and down quarks. This is equivalent to applying a small external magnetic field to the analogy above which results in a preferred direction for the spins to align with. The Gell-Mann-Oakes-Renner (GOR) [11] relation interlinks the pion mass and decay constant with the bare quark mass and the chiral condensate

$$m_\pi^2 f_\pi^2 = -2m_q\langle\bar{q}q\rangle. \tag{1.3}$$

A direct evidence of spontaneous breaking of chiral symmetry in the vacuum can be found in the isovector-vector[10] channel and its chiral partner the isovector-axialvector[11] channel of the hadronic spectral functions which encode information on the mass and width of hadrons. These have been measured with high precision by the ALEPH[12] [12] and OPAL[13] [13] collaborations at the LEP[14] collider in decays of τ leptons into an even / odd number of pions for the vector (V) / axialvector (A) channel. Both spectral functions shown in Figure 1.3 exhibit a prominent peak which is caused by the ρ meson in the vector and the a_1 meson in the axialvector channel.

The difference of the vector and axialvector spectral functions (integrated over all energies) is closely related to the chiral condensate by a Weinberg sum rule [14, 15]

$$\int_0^\infty \frac{ds}{\pi}\left[\rho_V(s) - \rho A(s)\right] = m_\pi^2 f_\pi^2 = -2m_q\langle\bar{q}q\rangle. \tag{1.4}$$

For the second equality the GOR relation was utilized. If the QCD vacuum would be invariant under chiral transformations, the spectral functions of both channels should be degenerate which is clearly not the case.

7 The light up and down quarks acquire a mass of only $2-5$ MeV [10] via the Higgs mechanism.
8 The quark content of a proton is given by two up and one down quark (uud). A neutron consists of one up and two down quarks (udd).
9 Chirality is related to the spin orientation of a massless particle relative to its direction of motion ("handedness").
10 Particles with isospin 1, spin 1 and odd parity ($I\,J^P = 1\,1^-$).
11 Particles with isospin 1, spin 1 and even parity ($I\,J^P = 1\,1^+$).
12 ALEPH: Apparatus for LEP Physics.
13 OPAL: Omni-Purpose Apparatus at LEP.
14 LEP: Large Electron-Positron collider (with center-of-mass energies up to $\sqrt{s} = 209$ GeV).

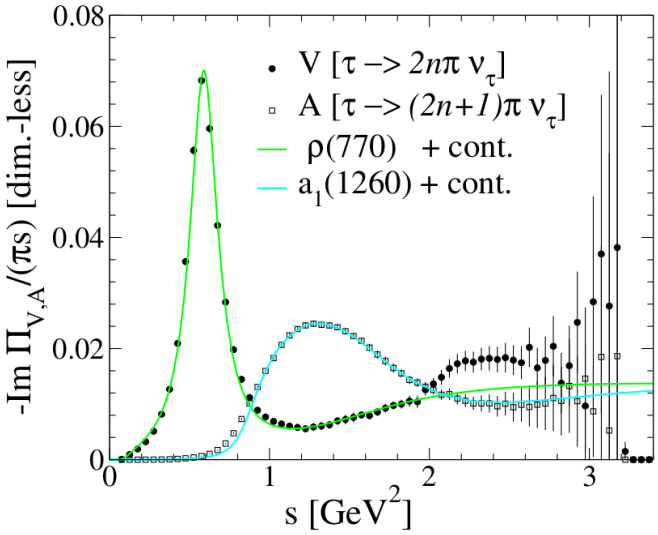

Figure 1.3: Vector (V) and axialvector (A) spectral functions measured in hadronic τ decays [12, 13] with fits using the vacuum spectral functions of the ρ and a_1 mesons [4].

1.2 Phases Transitions and the QCD Phase Diagram

Ordinary matter like, e.g., water exists in the form of vapor, liquid or solid (ice) depending on the thermodynamical parameters. The same is also true for QCD matter. Different phases are accessible by changing the temperature[15] and baryon chemical potential[16] or density[17] of the system. The structures in the QCD phase diagram are related to changes in the degrees of freedom and the symmetry properties. Differently to the case of water, however, the phase boundaries are neither understood properly nor measured. Our knowledge relies to a large extent on theoretical predictions.

If nuclear matter is compressed and heated, the hadrons inside the system progressively occupy more of the available space and begin to overlap with their surrounding neighbors. The quarks and gluons start to interpenetrate several hadrons. Finally they are liberated from their confinement. This phase of QCD matter is called quark-gluon plasma[18] (QGP) and was observed in heavy-ion experiments at RHIC[19] [17–20] and LHC[20] [21, 22]. It is assumed that the early universe, shortly after the Big Bang, was filled with this hot deconfined matter, while cold and dense quark matter may exist in the interior of a neutron star[21].

The first ideas that altering temperature T and net-baryon density ϱ could cause a phase transition came up in the mid-'70s [23, 24] and a vague notion developed of how the QCD phase diagram might look like. In our current understanding which is supported by lattice QCD (lQCD) calculations[22] there exists a smooth crossover between the hadron gas and the QGP at high temperatures and small net-baryon densities, but at high densities a true phase transition is expected to take place. The transition line might then terminate in a critical endpoint which would be a prominent landmark to discover in the QCD phase diagram. A schematic view of a possible phase diagram of strong interacting matter is shown in Figure 1.4.

[15] The typical temperature scale is given by 1 MeV $\simeq 10^{11}$ K.

[16] The baryon chemical potential μ_B is related to the amount of energy needed to add an additional baryon to the system.

[17] The typical density scale is given by ground state nuclear matter density $\varrho_0 = 0.16\,\mathrm{fm}^{-3}$ which corresponds to a mass density of roughly 10^{17} kg/m^3.

[18] The name quark-gluon plasma was coined by E. Shuryak in 1978 [16].

[19] RHIC: Relativistic Heavy-Ion Collider (with center of mass energies per nucleon $\sqrt{s_{NN}}$ up to 200 GeV) at the Brookhaven National Lab (BNL), Upton, NY (USA).

[20] LHC: Large Hadron Collider (with center of mass energies per nucleon $\sqrt{s_{NN}}$ up to 5.5 TeV) at CERN (Conseil Européen pour la Recherche Nucléaire), Geneva (Switzerland).

[21] Neutron stars are possible remnants of burned-up massive stars which collapsed under their own gravitation in a supernova. These macroscopic objects contain the highest densities known to exist in the universe. Only the quantum degeneracy pressure of the nucleons and quarks which is due to the Pauli exclusion principle supports the neutron star against collapsing into a black hole.

[22] For high temperatures and vanishing baryon chemical potential a discretized version of QCD can be solved numerically on a space-time grid.

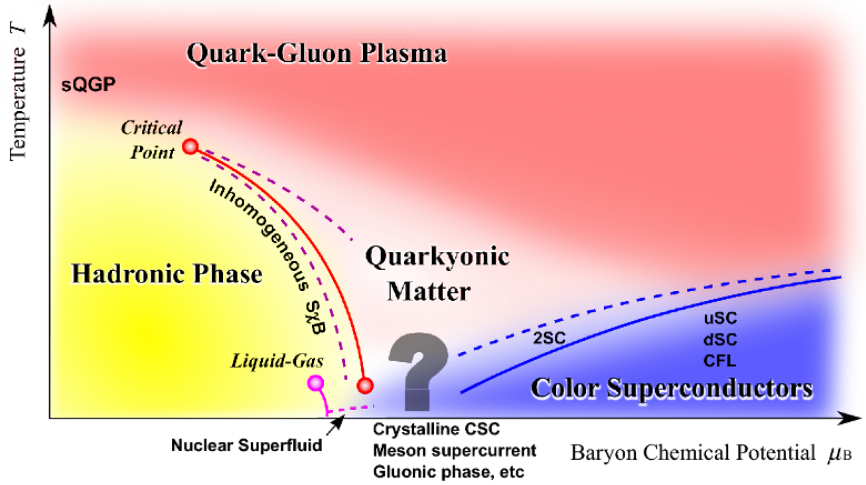

Figure 1.4: Sketch of a conjectured QCD phase diagram [25]. The hadronic phase (shown in yellow) exists at low temperatures T and baryon chemical potentials μ_B, whereas the deconfined QGP phase (shown in red) exists at high values of T and / or μ_B. Plotted is also a transition line between the phases which ends in a possible critical endpoint. In addition there are drawn some more exotic phases which have been predicted quite recently. In a quarkyonic phase (shown in white) the quarks and gluons would still be confined into colorless objects, but chiral symmetry would be restored [26–28]. In the very dense region with high μ_B there might exist a phase in which quarks couple to pairs, similar to electrons in a normal superconductor forming Cooper pairs [29]. This color-superconducting phase is shown in blue.

At around the same time or even before the deconfinement transition happens another transition restoring chiral symmetry may occur. While the chirally broken state of matter arises at low temperatures and densities, QCD inspired effective models, like the Nambu-Jona-Lasinio (NJL) model [30, 31], predict the melting of the chiral condensate. When heating the QCD vacuum the thermally excited hadrons "evaporate" the condensed $\bar{q}q$ pairs. This leads to a restoration of the spontaneously broken symmetry. Figure 1.5 shows a qualitative picture of the depletion of the chiral condensate when the temperature or baryon chemical potential are increased. Note that in the region along the temperature axis where the crossover to deconfinement happens, there is still a sizable amount of chiral condensate left, while the condensate drops quickly when the baryon chemical potential is increased beyond the point defined by the ground state of atomic nuclei.

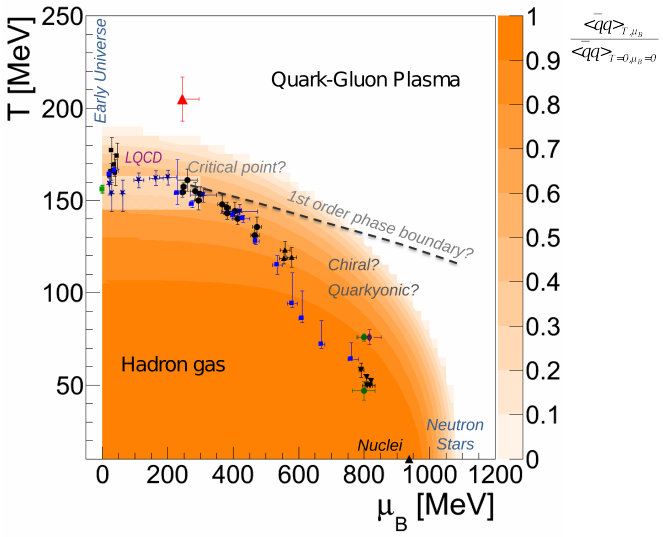

Figure 1.5: Sketch of the QCD phase diagram depicting the expectation value of the chiral condensate $\frac{\langle\bar{q}q\rangle_{T,\mu_B}}{\langle\bar{q}q\rangle_{T=0,\mu_B=0}}$ which is reduced as temperature T or baryon chemical potential μ_B are increased [32, 33]. For an explanation of the data points see section 1.4.

In the chirally restored phase, chiral partners must become degenerate implying massive modifications of the hadronic spectral functions. It is still a topic of active research to find out how exactly such a restoration of chiral symmetry is realized in nature. On one hand it has been suggested that the masses of the light hadrons scale with some power of $\langle\bar{q}q\rangle_{T,\mu_B}/\langle\bar{q}q\rangle_{T=0,\mu_B=0}$ ("Brown-Rho scaling") [34] and tend to zero as chiral symmetry gets restored, leading to a dropping mass scenario. On the other hand investigations employing hadronic many-body calculations find a strong broadening of the ρ meson spectral function resulting in a complete melting of the resonance as the chiral transition is approached [35]. These two scenarios are depicted in Figure 1.6.

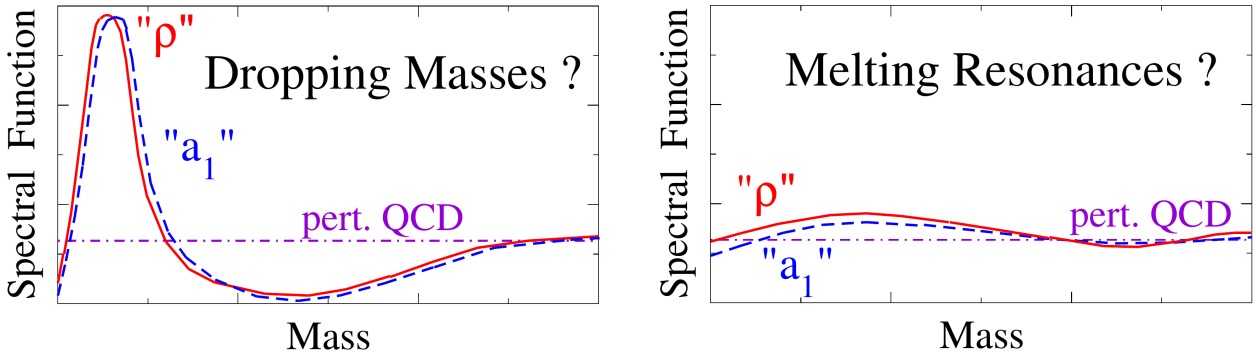

Figure 1.6: Schematic illustration of the different scenarios which can lead to a degeneration of the vector and axialvector spectral functions as chiral symmetry gets restored: Dropping mass scenario on the left, resonance melting on the right [4].

It is possible to create such a hot and dense environment in heavy-ion collisions (see section 1.3) and observe the changes to the ρ meson in the medium with dilepton spectroscopy (see section 1.4 and 1.5). The data collected by different experiments are in strong favor of a melting of the ρ meson into a flat continuum [36]. An even stronger statement about the chiral symmetry restoration could be made if the melting of the a_1 meson into a smooth continuum could be measured. Unfortunately this is hard to check in experiment[23]. Recent theoretical studies [15], using the broadening scenario of the ρ meson spectral function as input, predict an axialvector spectral function which has a smooth temperature dependence and melts into a continuum at high temperatures. A comparison of the obtained vector and axialvector spectral functions at different temperatures is given in Figure 1.7.

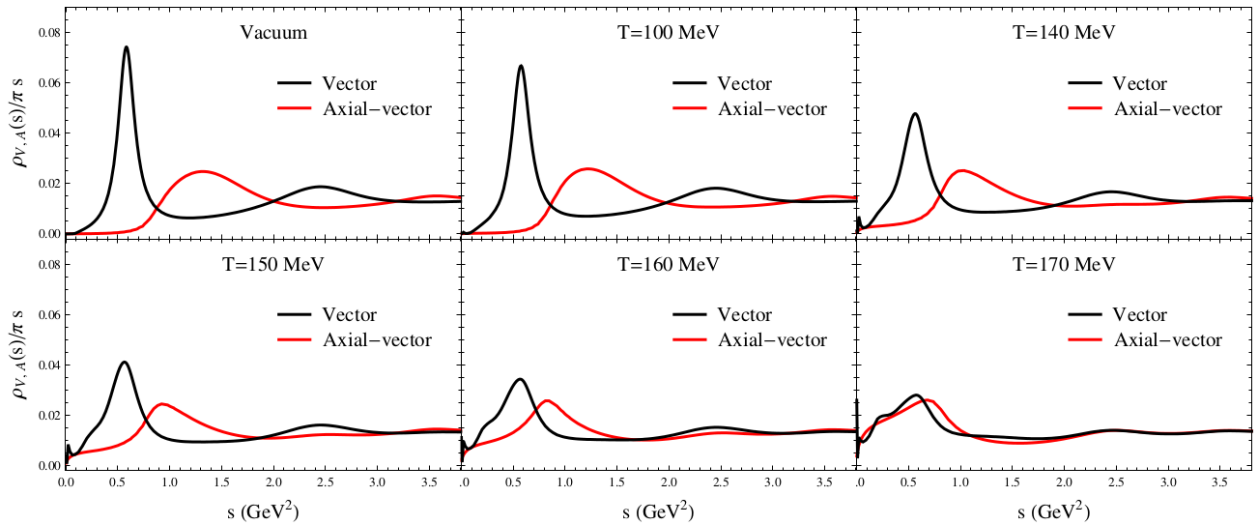

Figure 1.7: Vector (black) and axialvector (red) spectral functions in the vacuum and at different temperatures [15].

[23] The Dalitz decay of the a_1 meson involves besides a real or virtual photon also a pion which experiences rescattering and absorption in the medium and is, therefore, likely to loose its original information.

1.3 Heavy-Ion Collisions

One of the major goals in nuclear physics is the exploration of the QCD phase structure. The production of these extreme forms of matter in laboratory experiments and the systematic investigation of their properties in-depth is only feasible with heavy-ion collisions at relativistic and ultra-relativistic bombarding energies. The hot and dense fireball, generated in the collision zone, fades away on very short timescales[24] ($\sim 10\,\mathrm{fm/c}$). Thus, one can only measure the reaction products which fly into the detectors. The different attributes of the matter created in the events can later be reconstructed by analyzing the detected particles.

The time evolution of a heavy-ion collision can in general be divided into different stages which are shown in Figure 1.8. The incoming nuclei have a sizable fraction of the speed of light as their velocity and are therefore Lorentz-contracted in beam direction. The first-chance collisions can be interpreted as a superposition of hard nucleon-nucleon interactions which can be calculated using perturbative QCD (pQCD). They can also be measured independently in proton-proton ($p+p$) and proton-neutron ($p+n$) collisions[25] which serve as "control experiments". By isospin symmetry the neutron-neutron ($n+n$) contribution should be the same as $p+p$. A short time after these first-chance collisions, the particles in the collision zone have experienced enough rescattering that the medium reaches thermal equilibrium. Depending on the beam energy the matter created inside the fireball may undergo a transition into a QGP or possibly into some other exotic QCD phase. The hot and dense medium starts to expand and cools down. At some point it reaches the phase boundary to hadronic matter and hadronizes. The baryons and mesons form a hadron resonance gas in which inelastic and elastic collisions frequently occur, leading to the excitation of all sorts of hadronic resonances. The chemical freeze-out marks the point in the fireball evolution, when no more inelastic collisions happen and thus the particle composition is fixed. At kinetic freeze-out also the elastic collision stop and the momentum distributions of the particle species no longer change.

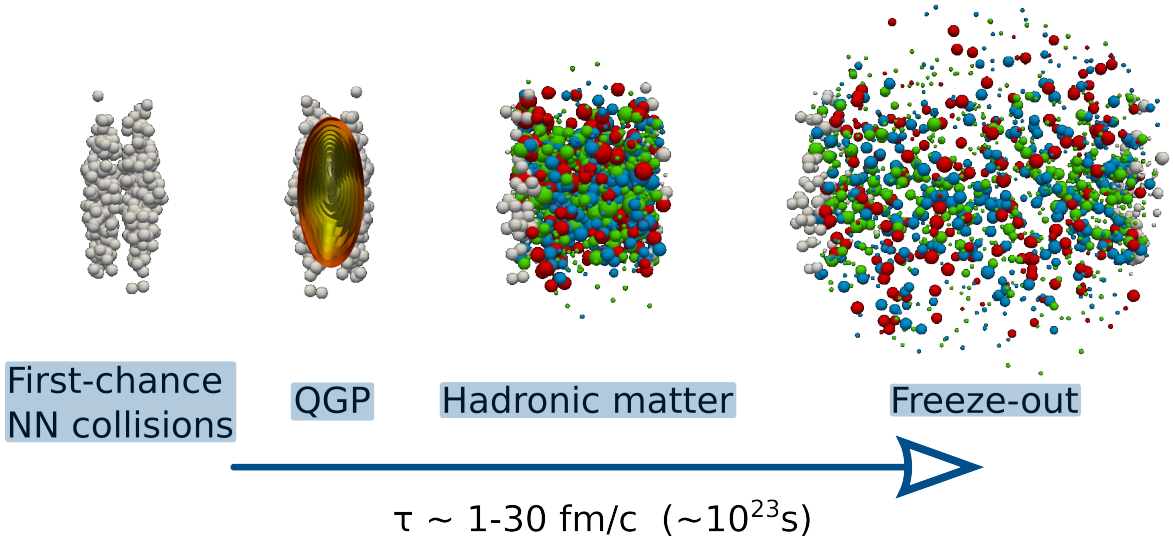

Figure 1.8: Artistic view of the evolution of an (ultra-)relativistic heavy-ion collision which can be divided into several stages: first-chance NN collisions, a deconfined QGP state and a hadron resonance gas state, followed by chemical and kinetic freeze-out. Nucleons which have not (yet) participated in the collision (spectators) are drawn as white spheres. The colored balls depict newly created hadrons with different amounts of transverse momentum p_T perpendicular to the beam direction (green: $p_T \leq 0.4\,\mathrm{GeV/c}$, blue: $0.4\,\mathrm{GeV/c} < p_T \leq 0.8\,\mathrm{GeV/c}$, red: $p_T > 0.8\,\mathrm{GeV/c}$). In the QGP phase the temperature profile of the created deconfined medium is shown. Visualizations taken from [37].

A wide temperature and density range can be investigated by changing and controlling the experimental conditions under which the fireball will be created. Those are the collision energy, the ion species used in the experiment and the centrality of the collisions (impact parameter). With high collision energies one can explore the baryon-poor, but very hot domain of the phase diagram. Since the amount of newly created particles (mostly pions) vastly exceeds

[24] $1\,\mathrm{fm/c} = 3.3 \cdot 10^{-24}\,\mathrm{s}$.

[25] Since free neutrons are uncharged and not stable, they can neither be accelerated nor be stored in a fixed target. The workaround is to collide protons and deuterons with each other and subtract the $p+p$ contribution.

the number of incoming nucleons and produced $\bar{q}q$ pairs hadronize roughly into an equal amount of baryons (B) and anti-baryons ($\bar{B}$), the net-baryon density $\varrho_{\text{net}} = \varrho_B - \varrho_{\bar{B}}$ is rather low in such fireballs. The regime of high net-baryon density and moderate temperatures on the other hand can be probed with lower energetic collisions where the number of newly created particles is smaller and the incoming nuclei are stopped to a sizable degree during the collision, leading to high baryon densities.

The first relativistic heavy-ion collisions were conducted in the 1970s at the BEVALAC[26] accelerator sited at the Lawrence Berkeley National Laboratory (LBNL) with beam energies in the 1-2 AGeV range. In the '90s beams in the same energy regime but with higher intensities became available at the SIS18 synchrotron located at GSI[27]. At the moment, the baryon-rich region of the phase diagram can be explored with the HADES experiment at the SIS18 and in the future with the CBM experiment at the planned FAIR[28] facility, the MPD experiment at NICA[29] and a proposed fixed target program at RHIC. Furthermore, with higher beam energies at the Brookhaven AGS[30] and the CERN SPS[31], it became possible to probe the rather baryon-poor area in the phase diagram.

At HADES and CBM the beam from the accelerator is directed to a fixed target. This has the advantage of a higher interaction rate as compared to colliding two beams head-on. The disadvantage is, however, that only a fraction of the beam energy is available in the center-of-mass frame for particle production. Therefore one needs colliders like the Brookhaven RHIC and the CERN LHC to study even higher energetic heavy-ion collision.

In addition a beam energy scan (BES) program is carried out at RHIC which allows the experiments there to take data also at lower collision energies and scan the phase diagram for signatures of a critical endpoint. Figure 1.9 highlights the various regions in the QCD phase diagram which are or will be accessible to explore with experiments sited at different accelerators.

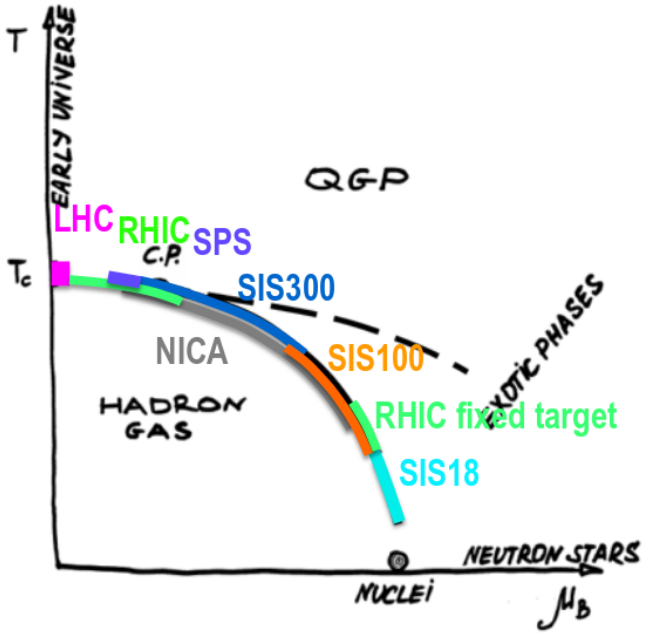

Figure 1.9: Sketch of the QCD phase diagram with the regions highlighted which are (or will be) accessible by experiments at different accelerators.

[26] BEVALAC: combination of the Bevatron (Billions of eV Synchrotron) and the linear accelerator SuperHILAC utilized as an injector for heavy ions.

[27] SIS: SchwerIonen Synchrotron, GSI: Helmholtzzentrum für Schwerionenforschung, Darmstadt.

[28] FAIR: Facility for Antiproton and Ion Research (with beam energies up to 10 AGeV for SIS100 and 35 AGeV for SIS300), to be build in Darmstadt.

[29] MPD: Multi Purpose Detector, NICA: Nuclotron-based Ion Collider fAcility (with center of mass energies per nucleon $\sqrt{s_{NN}}$ between 4-11 GeV) at the Joint Institute for Nuclear Research (JINR), Dubna (Russia).

[30] AGS: Alternating Gradient Synchrotron (with beam energies of 2-15 AGeV) at BNL.

[31] SPS: Super Proton Synchrotron (with beam energies of 40-200 AGeV).

1.4 Probes of the Hot and Dense Matter in the Fireball

In the quest for landmarks in the phase diagram of QCD matter the only milestones reached so far are the knowledge of a smooth cross-over from hadronic matter into the QGP along the temperature axis and a parametrization of the chemical freeze-out curve.

Hadrons are the most abundantly produced particles in heavy-ion collisions, but they are likely to lose their original properties via multiple scattering processes with the surrounding medium on their way out of the fireball. Only after chemical and kinetic freeze-out the information carried by hadrons can no longer alter and so they shed light on the later stages of the collision. The hadron yields measured in experiments at various beam energies are well explained by a chemically equilibrated hadron resonance gas (HRG) [38]. They can be analyzed with the statistical hadronization model (SHM) [39, 40] to extract the temperature and baryon chemical potential of the fireball at the moment of chemical freeze-out. A fit to these points results in a universal parametrization of the freeze-out curve.

Figure 1.10 summarizes the know landmarks in the phase diagram obtained with lattice QCD and the statistical hadronization model.

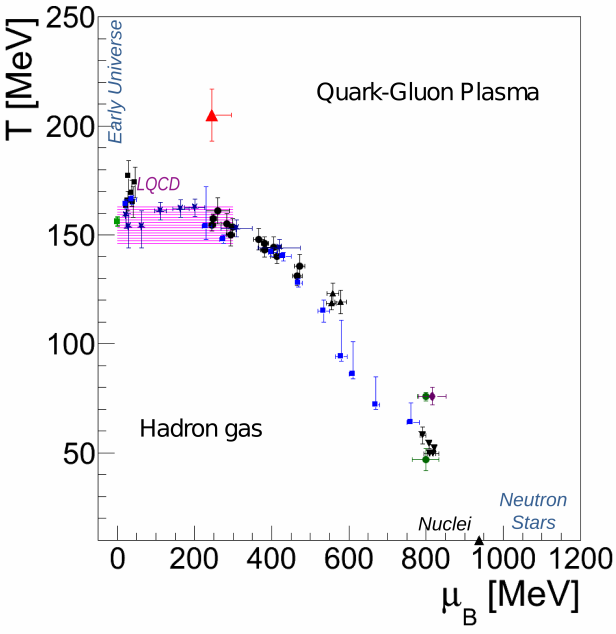

Figure 1.10: Phase diagram of QCD matter including data describing the (T, μ_B) points obtained with the final-state hadron abundances in a statistical model (the black symbols are from [41], the blue squares are from [28], the lila diamond is from [42], the green circles are from [43, 44]). The pink band is a result of lattice QCD calculations [45]. The red triangle results from the slope in the IMR of dimuons measured by NA60 [46].

While fluctuations of conserved quantities, like net-electric charge or baryon number, might help to find the phase boundaries and locate a possible critical endpoint [47], rare probes are the best choice to learn about the changes of the microscopic degrees of freedom in the medium, the restoration of chiral symmetry and the temperature inside the fireball prior to chemical freeze-out. Already more than 30 years ago it was realized that electromagnetic probes represent an ideal tool in this respect [16, 48].

Photons interact only electromagnetically with other particles. As the coupling constant $\alpha_{\mathrm{EM}} \approx \frac{1}{137}$ is much smaller then the strong coupling α_{S}, the production rate of real photons as compared to hadrons is diminished. Lepton pairs (l^+l^-, $l = e, \mu$) radiated from virtual photons[32] (dileptons) are even more suppressed by an additional power of α_{EM} which makes them a rare probe. This drawback of a small interaction probability is, however, also a great benefit. Since their mean free path in the medium is much larger than the typical size of the fireball, these probes can carry the information undistorted from the hot and dense collision zone to the detector.

[32] Unlike real photons (γ), the virtual ones (γ^*) carry mass. They live only for short times (allowed by the Heisenberg uncertainty principle) and quickly decay into other particles, like lepton pairs (l^+l^-), to obey the relativistic energy-momentum relation $E^2 = p^2c^2 + m^2c^4$.

The explosive fireball expansion leads to a collective motion of the medium which builds up over time and leaves its traces in the transverse momentum spectra of the different particles. While hadrons receive the full flow reached at the moment of decoupling, electromagnetic probes are emitted continuously and may provide the possibility to track the evolution of the medium during the collision.

Thermal photon radiation might constitute a good experimental tool to measure the temperature in the early stages of a heavy-ion collision. If one can isolate the photons which are emitted shortly after the medium thermally equilibrates and the collective flow has not yet had time to build up, then the slope extracted from their p_T spectra would be directly related to the temperature of the emitting source. Otherwise the slope parameter will be convoluted with a blue-shift to higher transverse momenta due to the radial expansion.

Unlike real photons, dileptons transmit additional information through their invariant mass which is inherited from their parent particle and reflects the parent's mass distribution at the moment of decay. The light vector mesons (ρ, ω and ϕ) are particularly interesting in this respect, since they carry the same quantum numbers as photons and can therefore directly decay into dileptons. The ρ meson plays a special role due to its short lifetime[33]. It is likely to decay inside the strongly interacting fireball where hadrons are presumably subject to in-medium modifications of their properties as a result of a partial restoration of chiral symmetry in the fireball. Thus, the invariant mass spectrum of dileptons is an invaluable tool in the investigation of these in-medium modifications. A sketch of such a spectrum is shown in Figure 1.11.

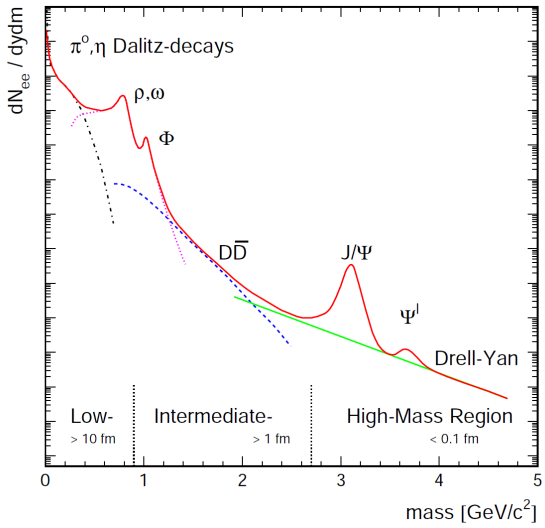

Figure 1.11: Invariant mass spectrum of dileptons [49].

The dilepton mass spectrum can roughly be subdivided into three regions. The low-mass region (LMR) up to the ϕ meson ($m_\phi \simeq 1\,\text{GeV}$) is dominated by (Dalitz) decays of baryonic resonances, the light vector mesons and the pseudo-scalar[34] mesons (π^0, η, η'). Hints of chiral symmetry restoration might show up in this region. Lepton pairs created in correlated semi-leptonic decays of mesons containing charm quarks ($D, \bar{D} \to e^+\nu X, e^-\bar{\nu}X$) and thermal radiation from the QGP contribute as dominant sources to the intermediate-mass range (IMR) of the dilepton spectrum between the ϕ and the J/Ψ meson ($m_{J/\Psi} \simeq 3.2\,\text{GeV}$). Hard processes such as the Drell-Yan[35] annihilation ($q\bar{q} \to l^+l^-$) happen primarily in high energetic first-chance collisions and emit dileptons into the high- and intermediate-mass region (HMR / IMR).

As pointed out recently [46, 50] the thermal dilepton radiation from the IMR of the invariant mass spectrum can serve as a thermometer of the fireball. The slope parameter extracted from an exponential fit to the intermediate mass range constitutes a true temperature without blue-shift effects from the medium's collective flow. Such a measurement conducted at different beam energies might even serve as a tool to search for a phase transition from the QGP to hadronic matter. The signature to look for would show up as a plateau followed by a sudden drop in temperature when going down in collision energy, instead of a smoothly decreasing temperature. Figure 1.12 depicts both scenarios.

[33] $\tau_\rho = 1.3\,\text{fm/c} < \tau_{\text{fireball}} \sim 10\,\text{fm/c}$, while the lifetimes of ω and ϕ are much longer ($\tau_\omega = 23.5\,\text{fm/c}$ and $\tau_\phi = 46.5\,\text{fm/c}$).

[34] Particles with total spin 0 and odd parity: $J^P = 0^-$.

[35] Annihilation of a quark from one nucleon with a sea-antiquark from another nucleon.

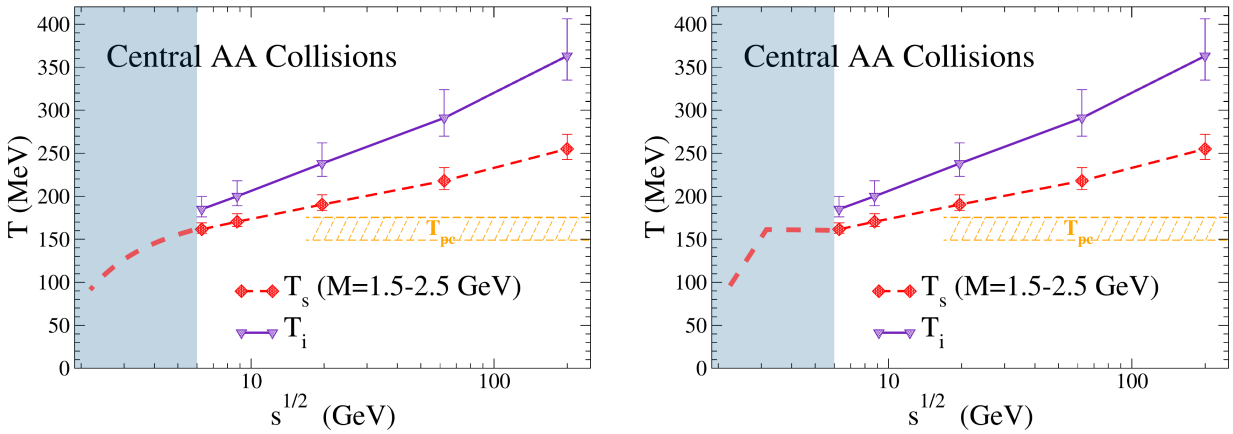

Figure 1.12: Predicted excitation function ($\sqrt{s_{NN}} = 6 - 200$ GeV) of the inverse slope temperature T_S extracted from thermal intermediate-mass dileptons [50]. The extrapolations by the author in the blue shaded areas down to lower collision energies show two different scenarios: a smoothly decreasing temperature on the left and on the right a plateau followed by a steeply falling temperature which is a possible signature of a 1st order phase transition.

1.5 Enhancement of Low-Mass Dileptons in the Invariant Mass Spectrum and the X Factor

Long-lived particles decaying inclusively into virtual photons, such as π^0, η and ω, feed into the invariant mass spectrum primarily after freeze-out. The resulting mixture of unmodified hadronic resonance contributions defines the "hadronic cocktail". The CERES experiment at the CERN SPS observed that the data from proton-nucleus ($p+A$) collisions can be reproduced by the hadronic cocktail, whereas the data from nucleus-nucleus ($A+A$: $S+Au$ at 200 AGeV and $Pb+Au$ at 158 AGeV) collisions show a strong excess in the yield of low mass dileptons below the ρ meson pole mass [51–54]. Going down in collision energy ($Pb+Au$ at 40 AGeV) the measured excess is even bigger [55].

As discussed in section 1.2, different theoretical models were developed to explain this either with a shift of the pole mass of the ρ meson [34, 56, 57] or with a strong broadening of its mass distribution [3, 58] ("melting" vs. "dropping mass"). In a high precision measurement of the dimuon invariant mass spectrum (in $In+In$ at 158 AGeV), the NA60 experiment at SPS was able to subtract the hadronic cocktail from the data and thus, measure the excess spectrum for the first time [36, 59]. It could be demonstrated that the observed excess favors a broadening of the ρ spectral function in the medium [4, 60, 61].

The many-body approach by R. Rapp and J. Wambach identifies baryons as a dominant source of the medium effects. This model is not only in agreement with the measurements at SPS, but also very successful in describing the data of the STAR[36] experiment at top RHIC energies [62–64] as well as the spectra from the recently conducted beam energy scan [65, 66]. Figure 1.13 shows the dilepton spectra measured by CERES, NA60 and STAR together with theoretical model calculations for the in-medium ρ and QGP contributions.

The PHENIX[37] collaboration also measured dielectrons at top RHIC energies and reported a strong enhancement in the low-mass range [69]. The theoretical models which were able to describe the data from the SPS experiments and STAR failed to explain the PHENIX excess.

The quality of the data, however, suffered from a considerable hadron contamination of the electron sample and a small signal to background (S/B) ratio. Therefore, the PHENIX detector was upgraded to improve the hadron rejection and supply additional electron identification power. The outcome of their new measurement campaign led the PHENIX collaboration to reject their older results [70]. The newly published dielectron excess is compatible with the STAR measurements.

At the much lower beam energies of the BEVALAC a similar enhancement of the dilepton yield over the hadronic cocktail was observed by the DLS[38] experiment [71]. A satisfying theoretical explanation for this excess was missing for a long time. Thus, it received the name "DLS puzzle". A reinvestigation of comparable collision systems,

[36] STAR: Solenoidal Tracker At RHIC.
[37] PHENIX: Pioneering High Energy Nuclear Interaction eXperiment.
[38] DLS: Di-Lepton Spectrometer.

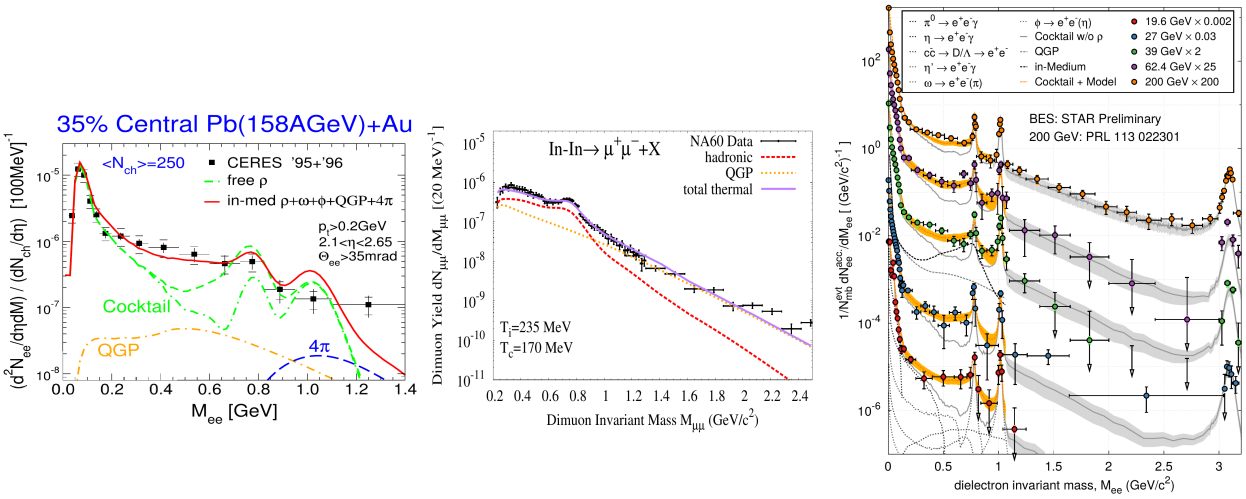

Figure 1.13: Dilepton spectra in heavy-ion collisions from CERES [53] (left), NA60 [46] (middle) and STAR [63] (right) compared to theoretical calculations with QGP and hadronic emission using the same model for the in-medium ρ spectral function [50, 67, 68].

measured with the HADES detector at SIS18 with improved resolution and higher statistics, confirmed the results obtained by the DLS collaboration [72–75].

Since the reference spectrum is not trivial at low energies, the HADES strategy is to measure consistently e^+e^- production in NN and AA collisions at the same beam energy. While the light $C+C$ system can be interpreted as a superposition of individual $p+p$ and $p+n$ collisions, there exists a non-trivial excess of dileptons for the middle-size $Ar+KCl$ system in the mass range of $0.15-0.5\,\mathrm{GeV/c^2}$, suggesting the onset of medium effects. The excess yield was isolated in a comparison with the measured elementary reaction reference spectra and shows a scaling with system size like $A_{\mathrm{part}}^{1.4}$. In 2012 the HADES collaboration was able to make the next step and measure the dilepton production in the heavy $Au+Au$ system. First results hint towards an even larger enhancement in the low mass region of the invariant mass spectrum for this collision system [33]. Figure 1.14 shows the low mass enhancements via a comparison of the spectra measured in the two systems $Ar+KCl$ at 1.76 AGeV and $Au+Au$ at 1.23 AGeV with scaled elementary reaction reference spectra.

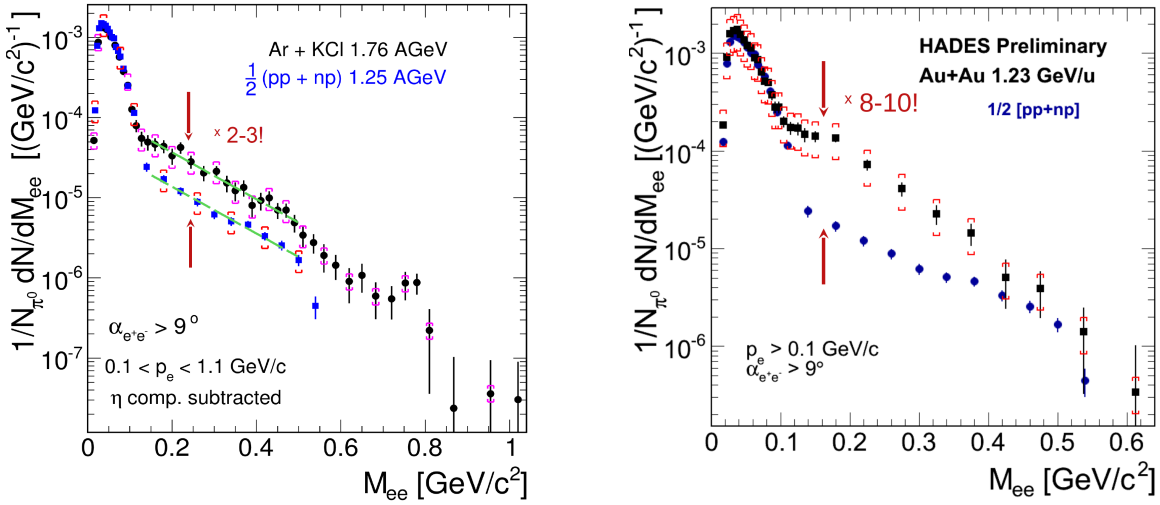

Figure 1.14: Comparison of the reference spectrum from properly scaled $N+N$ collisions with the reconstructed e^+e^- invariant mass distribution in $Ar+KCl$ (the expected contribution of η Dalitz decays has been subtracted) on the left [75] and $Au+Au$ on the right [33].

With the published dilepton spectra and the corresponding hadronic cocktails one can plot the excitation function of the enhancement over the cocktail. The enhancement factor X is defined as the ratio of the integrated yield measured in experiment to the integrated yield calculated from the hadronic cocktail with the correlated charm contribution subtracted from both of them.

$$X = \frac{\int_{0.45\,\mathrm{GeV/c^2}}^{0.7\,\mathrm{GeV/c^2}} dM \left(\frac{dN_{ll}}{dM}\right)_{\text{measured minus } \bar{c}c}}{\int_{0.45\,\mathrm{GeV/c^2}}^{0.7\,\mathrm{GeV/c^2}} dM \left(\frac{dN_{ll}}{dM}\right)_{\text{cocktail minus } \bar{c}c}}. \tag{1.5}$$

Figure 1.15 shows the excitation function of the X factor calculated with the available experimental data (left) and the excess yield in the LMR for STAR BES data [65] together with model extrapolations to lower energies (right). It is interesting to see the strong rise in the enhancement factor and excess yield towards the lower energy region highlighted in blue on the left panel. At these collision energies the (freeze-out) baryon density is expected to reach its maximum [76]. Up to now no dilepton measurement have been performed in this energy range, but it will be accessible with the CBM experiment at FAIR in the future. The enhancement factor can be interpreted as the number of ρ meson (or at lower collision energies Δ resonance) generations which decay inside the thermal fireball and get recreated during the evolution. This is the so-called ρ- or Δ-clock [33, 46, 77]. Theorists have recently identified the yield of thermal dilepton radiation integrated over a similar mass range of $0.3-0.7\,\mathrm{GeV}^2$ as a chronometer of the fireball [50]. Thus, the rise of the X factor hints towards a prolonged lifetime of the fireballs to be created at such collision energies. A non-monotonous variation of the fireball lifetime might indicate that the (T, μ_B) trajectory of the fireball passes close to a critical point of a phase transition.

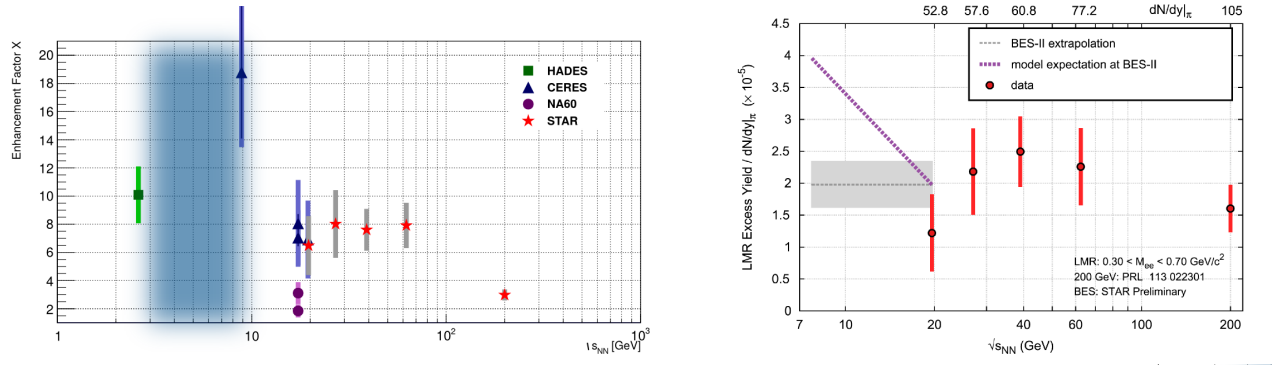

Figure 1.15: Left: Enhancement factor X = measured dilepton yield / cocktail yield ($\bar{c}c$ contributions subtracted from both) integrated over the mass range $0.45-0.7\,\mathrm{GeV/c^2}$ as published by the different experiments for collisions at various values of $\sqrt{s_{NN}}$. The low STAR point at $\sqrt{s_{NN}} = 200\,\mathrm{GeV}$ might be due to a wrong assessment of the charm contribution in the data. Highlighted is the region accessible in the future with FAIR without dilepton measurements up to now. Right: Excess yield scaled by the number of pions around midrapidiy as measured by STAR [65] together with model predictions for lower collision energies.

The thermal dilepton emission in the IMR is associated with radiation from the QGP. To extract a temperature from the excess radiation first the dileptons emanating from semi-leptonic decays of D mesons have to be eliminated. A precise vertex determination allowed the NA60 collaboration to reject muons coming from displaced secondary vertices. So far it is the only experiment which was able to measure the slope in the intermediate mass range. The resulting temperature $T = 205 \pm 15\,\mathrm{MeV}$ [46] is well above the corresponding freeze-out temperature at this collision energy and also higher than the critical temperature $T_c \simeq 170\,\mathrm{MeV}$ at which lQCD calculations suggest the transition into the deconfined phase [46, 78]. This measurement constitutes the proof of principle that dilepton radiation can serve as a thermometer, chronometer and barometer of the hot and dense fireball (see section 1.4).

1.6 HADES and CBM

Depending on beam energy and centrality, typical particle multiplicities reached in heavy-ion collisions range from a few tens up to several thousand reaction products per event (mainly nucleons and pions). The experimental task consists in detecting these particles, identifying their properties (e.g. mass, energy, emission angle, collective flow patterns, etc.) and filtering out the traces of the rare penetrating probes.

For this purpose the High Acceptance Di-Electron Spectrometer (HADES) [79] at GSI and the Compressed Baryonic Matter (CBM) experiment [1, 80] which will be built at the future FAIR facility are arranged in several detector layers, each serving a different task. A schematic view of both detector setups is shown in Figure 1.16. While experiments build at collider facilities have usually a barrel shape and the different detector layers surround the interaction region like “onion skin”, the fixed-target experiments are cone shaped with the tip of the cone being the target.

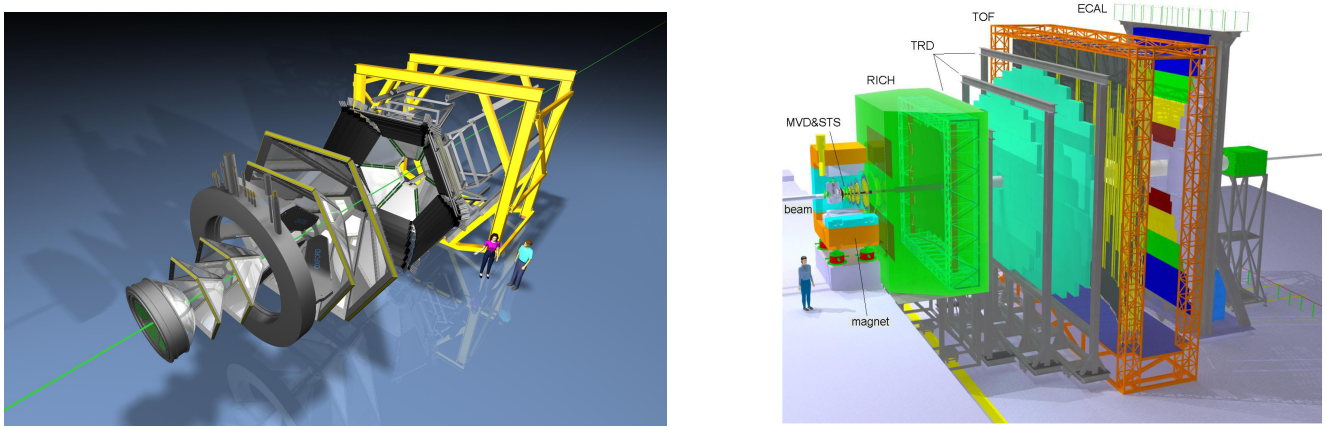

Figure 1.16: Sketch of the HADES detector in an expanded view (left) [81] and the CBM detector in the electron identification setup [82].

The aim of HADES is the systematic investigation of the production of dielectrons and (multi-)strange particles in the SIS18 energy regime and in the future at SIS100. HADES consists of 6 identical sectors covering the entire azimuthal angle and polar angles between 18° and 85°. The tracking of charged particles is achieved with four layers of Multiwire Drift Chambers (MDC), two in front of and two behind a superconducting toroidal magnet. Particle identification is possible with the time-of-flight information provided by a diamond start detector (START) plus an array of plastic scintillators (TOF) and a Resistive Plate Chamber (RPC) wall. Furthermore the energy-loss in MDC and TOF, as well as the electromagnetic shower signatures in a Pre-Shower detector help to distinguish different particle species. In addition a Ring-Imaging Cherenkov detector (RICH) supplies the main electron identification power. In the future the Pre-Shower detector will be replaced by an Electromagnetic Calorimeter (ECAL) to extent the reconstruction capabilities of HADES. It allows the detection of photons and neutral hadrons decaying into photons and also improves the electron-pion discrimination at large momenta ($p > 400\,\mathrm{MeV}$) [83, 84].

FAIR will offer the opportunity to explore the QCD phase diagram at the highest baryon densities accessible in heavy-ion experiments. The research program of the CBM experiment is therefore focused on the study of matter under such extreme conditions and the exploration of the “terra incognita” in the QCD phase diagram, including the search for the 1^{st} order phase transition and the possible critical endpoint with the help of rare probes. To achieve this objective, the detector is designed to cope with high interaction rate measurements of a large variety of probes like open (D mesons) and hidden charm (J/Ψ and other $c\bar{c}$ states), multi-strange hadrons, dileptons from light vector mesons, and bulk observables like collective flow and event-by-event fluctuations [1].

The experimental setup will consist of a Micro-Vertex Detector (MVD), in order to distinguish the primary interaction vertex from displaced decay vertices, and a Silicon Tracking Station (STS) as the main tracking device, both located inside the magnetic field of a superconducting dipole magnet. Electron identification power is obtained with a RICH and a Transition Radiation Detector (TRD), both in front of an RPC time-of-flight wall for hadron identification. CBM will in addition be supplemented by an ECAL detector for the measurement of direct photons and a Particle Spectator Detector (PSD) for the determination of the event centrality [80].

The measurement of dimuons will be possible though the replacement of the RICH and parts of the TRD with Muon Chambers (MUCH) which consist of a hadron absorber interlaced with tracking detector layers. The absence of strong physical background sources, like π^0 Dalitz decays in the dielectron channel, is beneficial for muon pair measurements, but it comes with the drawback of the restriction to invariant masses above the two-muon production threshold ($2\,m_\mu = 210\,\mathrm{MeV/c^2}$) and the impossibility to simultaneous measure hadrons for correlation studies. Hence a measurement of both channels, dielectrons and dimuons, is important and can serve as a crosscheck of the results obtained with the other lepton type [82].

2 Realistic Event Generator — Simulation Tools and Theoretical Approaches to Dilepton Emission

To establish a link between experimental observables and the different phases and manifestations of hadronic matter is one of the major tasks of theoretical heavy-ion physics. Therefore, a detailed understanding of the dynamics in the reactions is mandatory. The calculation of dilepton production in hot and dense matter, e.g., requires the knowledge of the space-time history of the colliding and expanding nuclear system. Simulations constitute in this respect an important part of the theory and the experiments related to nuclear and particle physics. They are not only needed to gain insight into measured observables and to help with the interpretation of experimental results, but also to develop new analysis techniques that should be used on real data.

Simulations give experimentalists a feeling for the kind of events they expect or hope to find and the amount of statistics needed to extract a significant signal. Also the planning of new detectors and the optimization of their performance to find interesting physical signatures relies to some extend on simulations. Another application is the simulation of the detector geometry and response[1] to different impinging particles which allows to correct the measured raw data for geometrical acceptance and efficiency effects in order to extract the true physical signal.

Different kinds of event generators are employed to handle these tasks. On one hand, there are microscopic models which track individual particles and propagate them through a cascade of collisions and decays with the dynamics inspired by QCD. Macroscopic models, on the other hand, do not consider each collision in detail, but focus on a statistical description of the macroscopic observables of the system.

2.1 Pluto

Pluto [87, 88] is a Monte Carlo event generator designed for hadronic interactions. It can model elementary as well as heavy-ion induced reactions at moderately high energies of a few AGeV motivated by the physics program of the HADES experiment. Later on it was also adapted and integrated into the simulation frameworks of other experiments like CBM.

Pluto is a ROOT [89] based “laptop” simulation tool which makes it very modular and flexible. It allows for fast simulations of the reaction kinematics and decays as well as the application of filters for acceptance and efficiency. Thus, it is very well suited for fast event generation needed, e.g., for feasibility studies and model comparisons.

The basic idea behind Pluto is that one should be able to use the package in a very easy way, but still be allowed to customize it without many constraints. While the event production can be initialized with a few lines of code, the event generation can be adapted to the user’s needs by the opportunity to add new decays or particles into the existing package or incorporate new models of physics as plug-ins.

Implemented in Pluto is a “thermal fireball” model which creates thermally excited hadrons coming from the hot fireball. The distributions of their subsequent decay products can then be analyzed. A decay manager simplifies the execution of multi-channel cocktail simulations. An example of a hadronic cocktail produced with Pluto for $Au+Au$ collisions at a beam energy of 25 AGeV (SIS300 energy regime) is shown in Figure 2.1 on the left panel. Included are the various contributions to the dilepton invariant mass spectrum stemming from meson decays after freeze-out (blue lines). The ρ meson could be modeled by a Breit-Wigner distribution around its pole mass with a cutoff at the two-pion threshold $m_{ee} = 2m_{\pi}$ which is caused by the assumption that the phase space of the ρ meson is governed by the two-pion phase space [82].

The right panel of Figure 2.1 show the two dimensional thermal dilepton spectrum for different mass and transverse momentum bins calculated for $Au+Au$ at 20 AGeV [90]. It contains contributions of dileptons emanating from in-medium ρ meson decays and from QGP radiation.

Such two dimensional histograms can directly be used as an input for the mass and transverse momentum sampling in Pluto and incorporated in the dilepton cocktail. These thermal contributions to the dilepton invariant mass spectrum are also shown in Fig 2.1 on the left panel (red lines).

[1] In order to get secondary particles coming from interactions with the detector material a digitization package like GEANT [85, 86] (GEometry ANd Tracking) can be used.

It is the main goal of this thesis to develop a framework in which it is straightforward to calculate the two dimensional spectra for any collision system of interest. Every Pluto user should then be able to include the radiation from in-medium ρ meson decays and, depending on the energy, also the QGP contribution into their simulations.

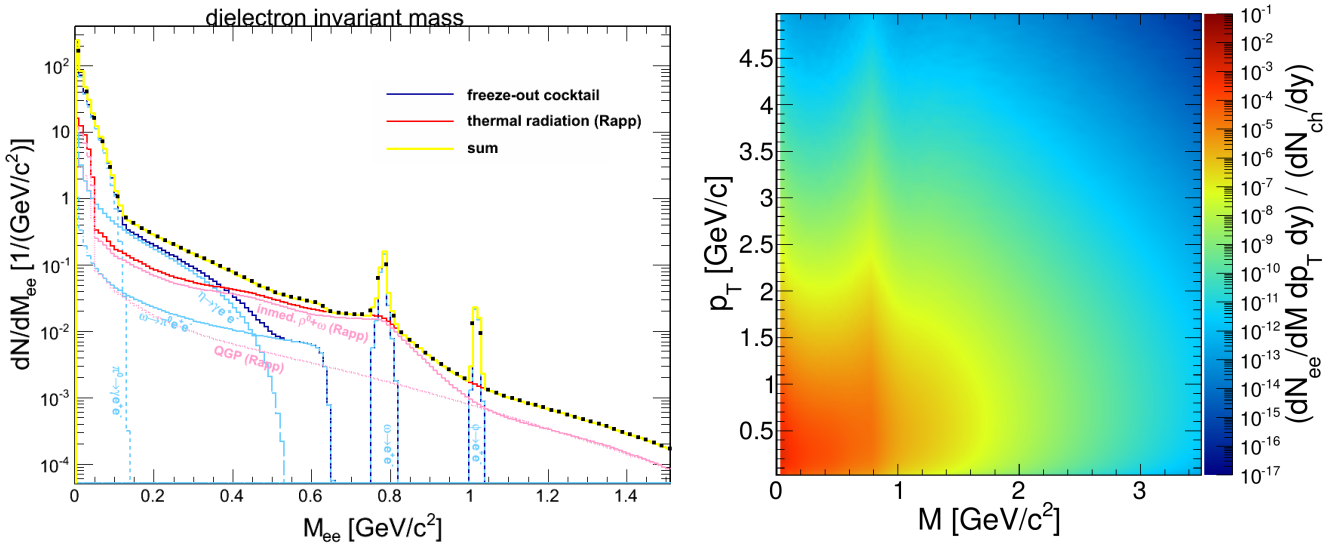

Figure 2.1: Left: Pluto cocktail for $Au + Au$ collisions at 25 AGeV with blue lines depicting the various freeze-out contributions and red lines showing the thermal sources (in-medium ρ + QGP). Right: Calculated two-dimensional spectrum of thermal radiation for $Au + Au$ at 20 AGeV [90].

2.2 The Transport Model UrQMD

Microscopic transport models aim to give a full description of the space-time history of a heavy-ion collision from the initial state to the final state after freeze-out over a broad range of collision energies. They track the trajectories of all hadrons including newly produced particles to provide the information about the evolution of the system. Examples of transport models which attempt to describe the data in the SIS energy regime, but also at higher energies, are the Giessen Boltzmann-Uehling-Uhlenbeck (GiBUU) approach [91] , Hadron-String Dynamics (HSD) [92, 93] and Ultrarelativistic Quantum Molecular Dynamics (UrQMD) [94, 95]. UrQMD which is widely used for simulations in various experiments, e.g., HADES, CBM, STAR, etc., gives an effective solution to the Boltzmann equation to reach that goal. It includes all known baryons and mesons with masses up to 2.2 GeV/c^2. Individual particles are represented by Gaussian wave packets with fixed width and propagated along classical trajectories. They can interact in form of elastic and inelastic scatterings. A collision between two hadrons will occur if

$$d < \sqrt{\frac{\sigma_{tot}}{\pi}} \tag{2.1}$$

where d is the impact parameter between the two hadrons and $\sigma_{tot}(\sqrt{s}, \text{type})$ the total free-particle cross section which depends on the energy and type of the collision respectively. At binary collisions with $\sqrt{s} > 3$ GeV, thus, negligible in the SIS energy regime, string excitations are also possible. The production of vector mesons at low energies takes place mainly via excitation of a heavier resonance and its subsequent decay (e.g. $N + N \rightarrow N + N^* \rightarrow N + N + \rho$), but also via pion annihilation ($\pi + \pi \rightarrow \rho$). The probability for a resonance to decay into a certain channel is determined by a mass dependent branching ratio which is based on the values given by the Particle Data Group (PDG) [10].

The attempt of transport models to account for the complicated reaction dynamics in heavy-ion collisions comes also with a drawback. The models are highly dependent on phenomenology and need an extended set of input parameters (e.g. form factors, decay branching ratios, production cross sections, pole masses and widths of resonances) which in many cases cannot be constrained by data or theoretical approaches.

The two most important output files of UrQMD which are also used in this work are the so-called “f14” and “f15” files. The f14 file is the standard output of UrQMD. At a given time after the start of every heavy-ion event the

position, momentum, energy and particle identity of every particle is written to file. Optionally also after every time interval of a given length the full information of all particles can be written to this file which makes it one of the main ingredients for the event generator developed in this thesis, see section 3.2. The f15 file on the other hand keeps record of every hadron-hadron collision and resonance decay which occurs during the events. This file can be used to track certain particles through the fireball evolution. It plays a major role in the determination of the strength with which the pion chemical potential figures into the dilepton rate calculation, see section 3.6, and it is the main source of information in the conventional way to calculate dilepton production with UrQMD.

In the so-called shining approach or time-integration method the resonances emit dileptons steadily over their whole lifetime from creation at time t_i to reabsorption or decay at time t_f in order to increase the available statistics [96]. This approach has a perturbative character as the dynamics of dilepton emission is not considered as the hadron cascade is progressing.

Figure 2.2 shows the dilepton invariant mass spectra calculated with the time-integration method in UrQMD [97] and GiBUU [98] together with the experimental data of $Ar + KCl$ collisions at 1.76 AGeV measured by HADES. The theory curves clearly fail to describe the data of the medium-heavy $Ar + KCl$ system for which in-medium modifications are expected.

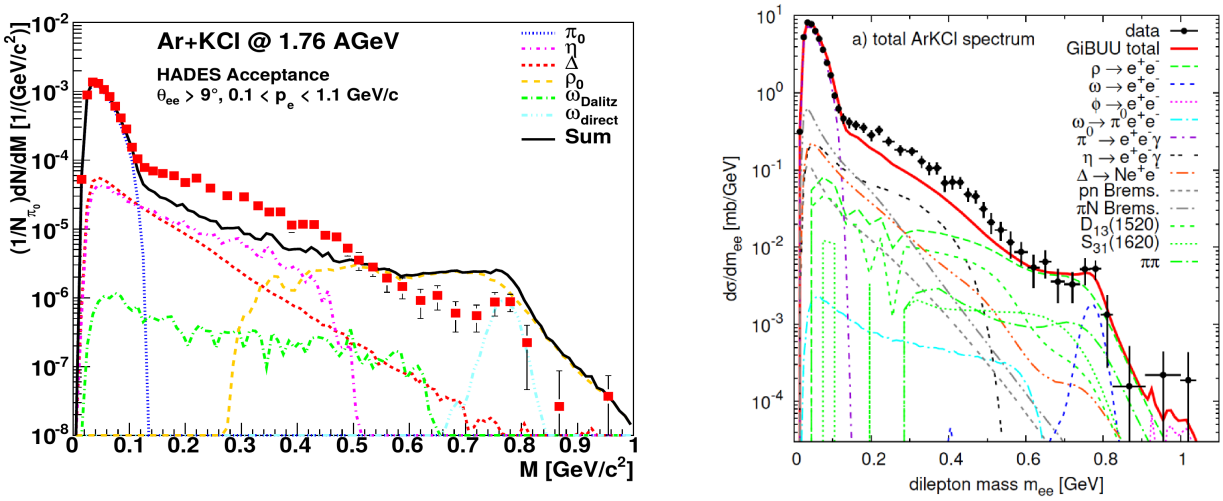

Figure 2.2: Dilepton invariant mass spectra calculated with the UrQMD shining approach [97] or with GiBUU [98] together with the experimental data of $Ar + KCl$ collisions at 1.76 AGeV measured by HADES.

Dilepton spectra at SIS energies are often calculated using non-equilibrium transport models as it is a priori not clear whether local thermalization occurs in these systems and, if so, over which period in time. Such a thermalization would however be the prerequisite to utilized hydrodynamical models for the fireball description.

The implementation of strong in-medium effects on the hadronic spectral functions, in particular the treatment of hadrons with broad spectral distributions, remains rather challenging in transport models [99–101].

2.3 Hydrodynamic Models

The hydrodynamic description of the fireball evolution is based on the assumption that the strong interactions in nuclear matter are able to maintain local thermal equilibrium throughout the expansion of the system until freeze-out happens. Each fluid cell is, in its rest frame, characterized by standard thermodynamic variables such as pressure, temperature and (energy-)density. Hence, hydrodynamics is the most natural framework to implement equilibrium dilepton rates, as they are formulated in the same variables, see section 2.5.

The basic equations of hydrodynamics are the conservation of energy and momentum which can be written in a Lorentz-invariant form as

$$\partial_\mu T^{\mu\nu}(x) = 0 \tag{2.2}$$

with the energy-momentum tensor $T^{\mu\nu}(x)$.

For an ideal fluid, thus neglecting viscosity, the energy-momentum tensor can be expressed as

$$T^{\mu\nu}(x) = [\epsilon(x) + p(x)]u^{\mu}(x)u^{\nu}(x) - p(x)g^{\mu\nu} \tag{2.3}$$

with the local energy density $\epsilon(x)$, pressure $p(x)$ and fluid 4-velocity $u^{\mu}(x) = \gamma\left(1, \vec{\beta}(x)\right)$.

Additionally conserved currents such as the baryon number current, $j_B^{\mu} = \varrho_B u^{\mu}$, are enforced by appropriate continuity equations

$$\partial_{\mu} j_B^{\mu} = 0. \tag{2.4}$$

In the later stages of a heavy-ion collision the pion number might also be effectively conserved due to the lack of pion-number changing processes. This leads to a further continuity equation

$$\partial_{\mu} j_{\pi}^{\mu} = 0 \tag{2.5}$$

which introduces a non-zero effective pion chemical potential μ_{π}.

The basic ingredient governing the hydrodynamic evolution which has to be put in to make the system of equations solvable is an equation of state (EoS), i.e., the dependence of the pressure on the energy- and baryon-density $p = p(\epsilon, \varrho_B)$. Additional freedom comes with the choice of initial conditions and the temperature and way in which the freeze-out occurs. The system of differential equations for the evolution is usually solved numerically on a space-time grid [1, 3].

2.4 Simple Fireball Model

The simple fireball model is an ansatz to reduce the computational power needed in hydrodynamic models to a tractable amount while keeping the essential features of it. The participants of a heavy-ion collision form a single “fireball“ of cylindrical shape which is at rest in the center-of-mass system. It is assumed that the inelastic collisions between the participants sufficed to completely thermalize the interaction region. The fireball then starts to expands isentropically. This ties the time evolution of temperature, baryon chemical potential, transverse velocity, longitudinal rapidity and chemical non-equilibrium properties such as a pion chemical potential to the geometry of the expanding fireball volume, constraining the number of free parameters which can be tuned to fit the results of experimental freeze-out spectra [3].

2.5 Equilibrium Dilepton Production Rate

The basic quantity which impacts the thermal (virtual) photon emission rate is the electromagnetic (EM) current-current correlation function Π_{EM}. It is defined as the thermal expectation value of the hadronic correlation function of two EM currents which comprise the charge carriers of the system. In the quark basis, corresponding to the elementary degrees of freedom of QCD, the EM current can be expressed as

$$j_{EM}^{\mu} = \sum_{i=u,d,s} e_i \bar{q}_i \gamma^{\mu} q_i = \frac{2}{3}\bar{u}\gamma^{\mu}u - \frac{1}{3}\bar{d}\gamma^{\mu}d - \frac{1}{3}\bar{s}\gamma^{\mu}s. \tag{2.6}$$

It can be rearranged into good isospin states which leads to the hadronic basis [102] with the currents of the light vector mesons

$$j_{EM}^{\mu} = \frac{1}{2}\left(\bar{u}\gamma^{\mu}u - \bar{d}\gamma^{\mu}d\right) + \frac{1}{6}\left(\bar{u}\gamma^{\mu}u + \bar{d}\gamma^{\mu}d\right) - \frac{1}{3}\bar{s}\gamma^{\mu}s = \frac{1}{\sqrt{2}}j_{\rho}^{\mu} + \frac{1}{3\sqrt{2}}j_{\omega}^{\mu} - \frac{1}{3}j_{\phi}^{\mu}. \tag{2.7}$$

The imaginary part $\mathrm{Im}\Pi_{\mathrm{EM}}$ of the current-current correlation function is called EM spectral function and directly determines the thermal photon and dilepton rates [103]

$$q_0 \frac{dN_\gamma}{d^4x d^3q} = -\frac{\alpha_{\mathrm{EM}}}{\pi^2} f^B(q_0;T)\,\mathrm{Im}\Pi_{\mathrm{EM}}(M=0, q=q_0;\mu_B,T) \tag{2.8}$$

$$\frac{dN_{ll}}{d^4x d^4q} = -\frac{\alpha_{\mathrm{EM}}^2}{\pi^3 M^2} L(M^2)\, f^B(q_0;T)\,\mathrm{Im}\Pi_{\mathrm{EM}}(M,q;\mu_B,T) \tag{2.9}$$

with the Bose-distribution $f^B(q_0;T) = (\exp(\frac{q_0}{T})-1)^{-1}$ and the (virtual) photon's energy q_0, 3-momentum q and invariant mass $M^2 = q_0^2 - q^2$.

$\frac{dN_{ll}}{d^4x d^4q}$ describes the amount of lepton pairs l^+l^- radiated off a cell of strongly interacting matter per unit time and 4-momentum. The lepton phase space factor $L(M^2)$

$$L(M^2) = \left(1-\frac{4m_l^2}{M^2}\right)^{1/2}\left(1+\frac{2m_l^2}{M^2}\right) \tag{2.10}$$

involves the mass m_l of the outgoing leptons and causes the disappearance of emission below the threshold of twice the lepton's mass. Above that cutoff the factor quickly reaches unity.

As there is no preferred direction in the local rest frame, the virtual photon is radiated isotropically. If the emitting source is however moving with respect to the lab frame, the resulting tracks have to be boosted to the lab frame according to the local 4-velocity of the medium $u^\mu = \gamma\left(1,\vec{\beta}\right)$. This is equivalent to substituting the energy q_0 and 3-momentum q with the Lorentz-invariant quantities $q_\mu \cdot u^\mu$ and $\left(\left(q_\mu \cdot u^\mu\right)^2 - M^2\right)^{1/2}$ on the right hand side of equation (2.8) and (2.9). This correction is especially important for the transverse momentum spectra, as a radial expansion of the fireball shifts the momenta to higher values, causing a blue-shift in the corresponding spectra.

In the vacuum $\mathrm{Im}\Pi_{\mathrm{EM}}$ is accurately known from the inverse process of hadron production in e^+e^- annihilation reactions. The corresponding cross section into hadronic final states is given by

$$\sigma(e^+e^- \to \mathrm{hadrons}) = \underbrace{\sigma(e^+e^- \to \mu^+\mu^-)}_{\frac{4\pi\alpha_{\mathrm{EM}}^2}{3s}} \frac{(-12\pi)}{s}\,\mathrm{Im}\Pi_{\mathrm{EM}}^{\mathrm{vac}}(s), \tag{2.11}$$

thus, $\mathrm{Im}\Pi_{\mathrm{EM}}$ can be measured by taking the ratio

$$R = \frac{\sigma(e^+e^- \to \mathrm{hadrons})}{\sigma(e^+e^- \to \mu^+\mu^-)} \propto \frac{\mathrm{Im}\Pi_{\mathrm{EM}}^{\mathrm{vac}}}{M^2} \tag{2.12}$$

which is shown in Figure 2.3. In the mass region $M \lesssim 1.5\,\mathrm{GeV/c^2}$ the EM spectral function is dominated by the low-mass vector mesons ρ, ω and ϕ as already suggested by equation (2.7).

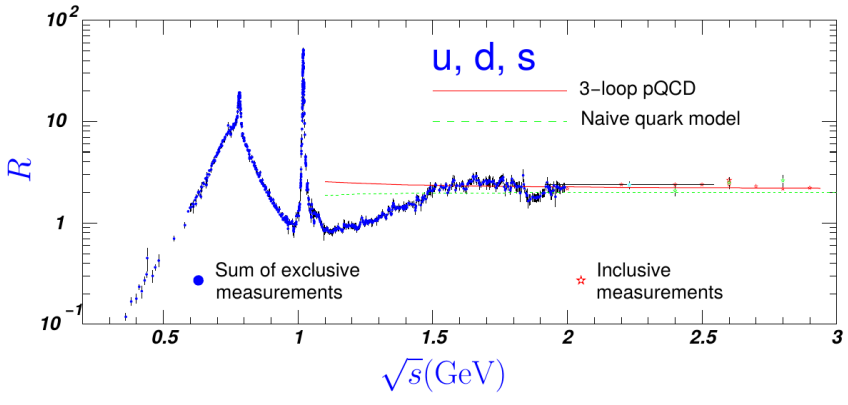

Figure 2.3: EM spectral function as measured by the R-ratio in e^+e^- annihilation into hadrons [10].

The three vector mesons represent the lowest resonances in the two-pion, three-pion and kaon-antikaon channels. The EM spectral function is therefore in accordance with the vector meson dominance model (VMD) which states that a (virtual) photon couples to any EM hadronic current exclusively via an intermediate vector meson [104].

At masses $M > 1.5\,\mathrm{GeV/c^2}$ one enters into the perturbation regime in which hadronization has only a small impact on the smooth continuum. The dilepton emission in this regime corresponds to multi-hadron annihilation (4π, $6\pi \rightarrow l^+l^-$ etc.) which may be excited via the scattering of two ρ mesons, a pion with an a_1 meson or a $\pi - \omega$ scattering.

In the vacuum the EM spectral function then takes the form

$$\mathrm{Im}\Pi_{\mathrm{EM}}^{\mathrm{vac}}(M) = \begin{cases} \sum\limits_{v=\rho,\omega,\phi} \left(\dfrac{m_v^2}{g_v}\right)^2 \mathrm{Im}D_v^{\mathrm{vac}}(M)\,, & M < M_{\mathrm{dual}}^{\mathrm{vac}} \simeq 1.5\,\mathrm{GeV/c^2} \\ -\dfrac{M^2}{12\pi}\left(1 + \dfrac{\alpha_s(M)}{\pi} + \ldots\right) N_c \sum\limits_{q=u,d,s} \left(e_q\right)^2\,, & M > M_{\mathrm{dual}}^{\mathrm{vac}}. \end{cases} \tag{2.13}$$

with the vacuum spectral functions of the vector mesons $\mathrm{Im}D_v^{\mathrm{vac}}$ ($v = \rho, \omega, \phi$).

Taking this as the starting point, the question is: how does the spectral function of the ρ meson which gives the dominant contribution to $\mathrm{Im}\Pi_{\mathrm{EM}}$ change inside hot and dense nuclear matter? In the many-body calculation by R. Rapp and J. Wambach [58] the propagator D_ρ of the ρ picks up additional contributions to the self-energy of the meson

$$D_\rho(M, q; \mu_B, T) = \frac{1}{M^2 - m_\rho^2 - \Sigma_{\rho\pi\pi} - \Sigma_{\rho M} - \Sigma_{\rho B}} \tag{2.14}$$

which account for the coupling to the surrounding nuclear medium. $\Sigma_{\rho\pi\pi}$ contains interactions of the ρ meson's pion cloud with hadrons from the medium, e.g. $\pi N \rightarrow \Delta$. Direct scatterings of the ρ off mesons (e.g. $\rho\pi \rightarrow a_1$) and baryons (e.g. $\rho N \rightarrow N^*$) are included in $\Sigma_{\rho M}$ and $\Sigma_{\rho B}$, respectively [102]. Figure 2.4 depicts the Feynman-diagrams of a propagating ρ meson in the vacuum and in the medium.

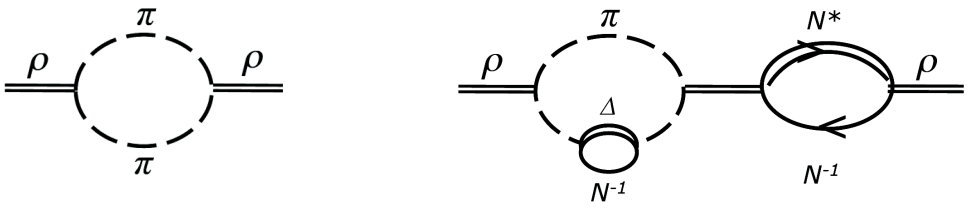

Figure 2.4: Feynman-diagrams of the main contributions to the ρ meson self-energy in the vacuum (left) and in the medium (right). In the vacuum the main contribution comes from a $\pi - \pi$ loop. In the medium additional interactions with the baryons and mesons of the surrounding hot and dense matter which allow the creation of resonance-hole excitations have to be taken into account.

While in the vacuum it gets its spectral width from a $\pi - \pi$ loop, the additional contributions especially from interactions with the baryons in the medium cause a strong broadening of the ρ meson spectral function as shown in Figure 2.5 on the left [102]. On the right panel of Figure 2.5, the ρ meson is embedded in a hot meson gas with all baryon-induced effects switched off, leading to a by far less pronounced melting of the peak.

The emission rates above assume the system to be not only in thermal, but also in chemical equilibrium. After chemical freeze-out the particle composition in terms of stable particles (with regard to the strong interaction) does no longer change, although the hadronic system still interacts via elastic collisions sustaining thermal equilibrium until the kinetic freeze-out is reached. This leads to situations in which there are more pions in the fireball than one would expect from the thermally equilibrated, cooled down system, leading to a build-up of an effective pion chemical potential μ_π. The extra pions trigger an enhanced production of ρ mesons via $\pi - \pi$ annihilation and resonance excitations which in turn increases the amount of radiated (virtual) photons.

To reflect this fact in the production rates an additional pion fugacity factor z^k can be included in equation (2.8) and (2.9) with the fugacity

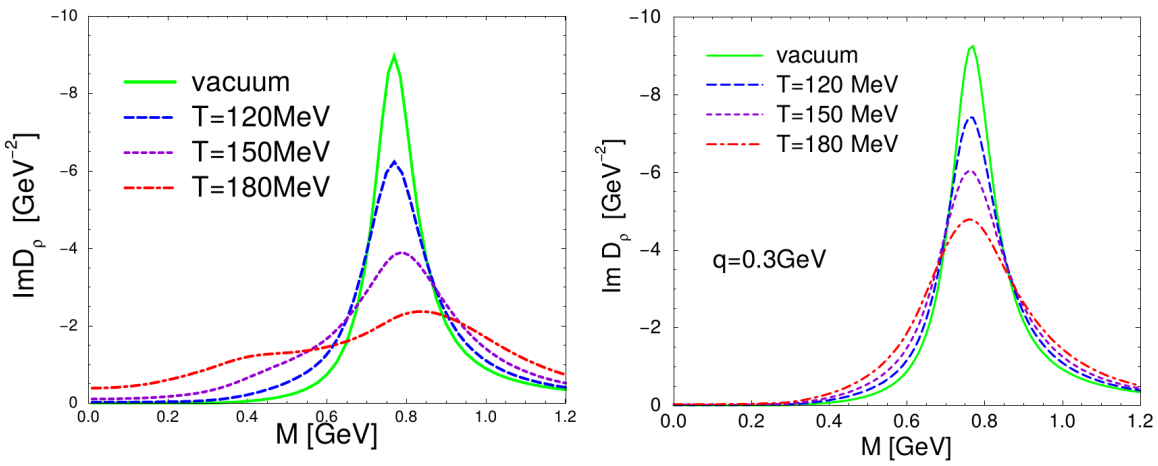

Figure 2.5: Spectral function of the ρ meson in hot and dense hadronic matter for temperatures $T = 120$, 150 and 180 MeV and baryon densities of $0.1\varrho_0$, $0.7\varrho_0$ and $2.6\varrho_0$, respectively, on the left [102]. The right panel shows the same spectral function in a hot meson gas with all baryon-induced medium effects switched off.

$$z = \exp\left(\frac{\mu_\pi}{T}\right). \tag{2.15}$$

This factor enhances the dilepton rate as long as the pion chemical potential takes positive values. The exponent k reflects the mean number of pions needed to produce a ρ meson. At SPS and RHIC energies for which the pion-to-baryon ratio is larger then 5, the most important production mechanism is the $\pi - \pi$ annihilation yielding $k = 2$. At the lower SIS energies a value around 1 is more logical, since resonances decays play a significant role in the ρ production. A more detailed analysis of which value for the exponent should be used at SIS energies is part of this work (see section 3.6).

For practical use in the event generator for in-medium dileptons a parametrization of the Rapp-Wambach spectral function $\mathrm{Im}D_\rho^{\mathrm{inmed}}(M, q; T, \varrho_{\mathrm{eff}}, \mu_\pi)$ will be used which was provided by Ralf Rapp. It needs the temperature T, the pion chemical potential μ_π and the effective baryon density ϱ_{eff} as input. The latter is defined as

$$\varrho_{\mathrm{eff}} = \varrho_N + \varrho_{\bar{N}} + \frac{1}{2}(\varrho_R + \varrho_{\bar{R}}) \tag{2.16}$$

where $\varrho_{N(\bar{N})}$ denotes the density of (anti-) nucleons and $\varrho_{R(\bar{R})}$ of baryonic resonances. The effective baryon density is used as the ρ couples in the same way to baryons and anti-baryons (though the contribution of anti-baryons is irrelevant at SIS energies). The factor $\frac{1}{2}$ reflects the finding that the resonances have a less pronounced effect on the spectral shape of the ρ meson [58]. The parametrization has been tested and agrees with the full Rapp-Wambach spectral function in general within a few 10's of percent (better for space-time integrated spectra) which is sufficient for the purpose at hand [90].

Thus the EM spectral function in equation (2.8) and (2.9) can be expressed as

$$\mathrm{Im}\Pi_{\mathrm{EM}}^{\mathrm{inmed}\rho}(M) = \frac{m_\rho^4}{g_\rho^2}\,\mathrm{Im}D_\rho^{\mathrm{inmed}}(M, q; T, \varrho_{\mathrm{eff}}, \mu_\pi) \tag{2.17}$$

with the bare mass of the ρ meson[2] $m_\rho = 829$ MeV and the coupling $g_\rho = \sqrt{2.7 \cdot 4\pi}$ [35].

For the radiation from the hadronic continuum in the intermediate-mass range a recent parametrization of the continuum in $e^+e^- \rightarrow$ hadrons will be utilized [15]. The EM spectral function takes the form

$$\mathrm{Im}\Pi_{\mathrm{EM}}^{\mathrm{cont}}(M) = -\frac{1}{8\pi}\left(1 + \frac{\alpha_S}{\pi}\right)\frac{M^2}{1 + \exp[(E_{\mathrm{th}} - M)/\delta]}. \tag{2.18}$$

[2] This would be the mass of the ρ if it would not interact with, e.g., pions.

The parameter $E_{\rm th}$ plays the role of a threshold energy, while δ determines how fast the limiting value is reached. The value of α_S is fixed to $\alpha_s(1\,\text{GeV}) = 0.5$, while the numerical values $E_{\rm th} = 1.5\,\text{GeV}$ and $\delta = 0.2\,\text{GeV}$ are taken from fits to the ALEPH data [12].

At higher beam energies the QGP contribution to the thermal emission should be included. In the quark-gluon plasma the leading source of dileptons is the electromagnetic annihilation of two quarks with equal flavor, $q\bar{q} \rightarrow l^+l^-$, corresponding to a structureless EM spectral function, $\text{Im}\Pi_{\rm EM}^{\rm QGP} \propto M^2$ [102]. In the last years progress has been made in extracting accurate QGP emission rates from lattice QCD at a pair momentum $q = 0$ [105]. An extension to finite q, as required for the application to experiment, has been constructed by implementing the $q = q_0$ dependence of the perturbative photon rate [106] and matching it to the results of lQCD [68]. The resulting QGP rates are similar to previous results using the hard-thermal-loop (HLT) approximation [107], but with an improved low-mass behavior and nontrivial 3-momentum dependence.

To obtain the invariant mass spectrum of dileptons from equation (2.9) one has to perform a transformation of variables from energy q_0 to mass M and integrate over the unwanted degrees of freedom, in this case the 3-momentum q, to get the dilepton rate

$$\frac{dR}{dM} = \frac{dN_{ll}}{d^4x dM} = \int d^3q \, \frac{M}{q_0} \, \frac{dN_{ll}}{d^4x d^4q}. \tag{2.19}$$

The invariant mass spectrum $\frac{dN_{ll}}{dM}$ is then given by the integral of the rate $\frac{dR}{dM}$ over the whole space-time evolution of the fireball

$$\frac{dN_{ll}}{dM} = \int d^4x \, \frac{dR}{dM} = \int d^4x \, d^3q \, \frac{M}{q_0} \, \frac{dN_{ll}}{d^4x d^4q}. \tag{2.20}$$

Other spectra, like the 2- or 3-differential $\frac{dN_{ll}}{dM\,dp_T}$ and $\frac{dN_{ll}}{dM\,dp_T\,dy}$ which are important for the implementation into Pluto, result from a different integration over the 4-momentum. The derivation of these can be found in the appendix 6.1.

The framework for the determination of a realistic space-time evolution of the expanding fireball formed in the reaction in terms of temperature and baryon density as well as pion chemical potential will be discussed in the next chapter.

3 Realistic Event Generator — Fireball Space-Time Evolution and Determination of Bulk Properties

The modular structure of Pluto makes it feasible to customize the event generator and incorporate models of in-medium physics like, e.g., the Rapp-Wambach spectral function as plug-ins. Before these thermal emission rates can be applied to the framework some more intermediate steps have to be performed, as the dilepton rates depend on the temperature T, effective baryon density ϱ_{eff}, pion chemical potential μ_π and the collective velocity $\vec{v}_{\text{coll}}$. These quantities have to be provided as input parameters to the model. Moreover, as dileptons are radiated over the whole evolution of the fireball and experiments measure only the time-integrated spectra, the calculation of lepton pairs requires the knowledge of the full space-time history of the colliding and expanding system.

For high energy collisions this evolution may be modeled with hydrodynamics. However, at low energies such a treatment of the heavy-ion collision is not applicable. The non-equilibrium transport models used to describe the fireball dynamics at SIS energies usually do not allow to define meaningful values for equilibrium thermodynamic quantities during the fireball evolution. As a middle ground between the microscopic transport and macroscopic hydro approach a coarse-graining procedure may resolve this tension.

3.1 General Concept of Modeling the Fireball Space-Time Evolution

The elementary idea to realistically model the space-time evolution of the fireball for the new event generator is to simulate an ensemble of events with a transport model like UrQMD. By averaging the baryon and pion distributions in suitable space-time cells over many events one obtains smooth space-time distributions which allow for the extraction of local temperatures and baryon densities if the interactions in the fireball are strong enough to equilibrate the system.

Figure 3.1 shows a sketch of this so-called coarse-graining of hadronic transport for an ensemble of central $Au+Au$ collisions at three different time steps.

Once the bulk properties of the hot and dense matter are determined over the whole fireball history the thermal dilepton emission rates, discussed in section 2.5, can be convoluted with the realistic space-time evolution to compute the dilepton emission. Thus, the coarse-graining procedure which is based on a proposal by P. Huovinen and J. Kapusta [109, 110] combines the virtues of a microscopic space-time evolution with the ability to use pertinent in-medium dilepton rates calculated with hadronic many-body theory.

The price is the assumption of local thermal equilibrium which is however mitigated compared to a full hydrodynamic simulation, since deviations from the vanishing mean-free-path limit are still kept in the evolution.

Recently a similar approach was used by S. Endres *et al.* to calculate the dilepton emission in the SPS and also SIS18 energy regime [111–113].

3.2 Dividing the Fireball Space-Time Evolution

For the development of the framework for the new event generator of in-medium dileptons, four different heavy-ion systems were chosen for which central UrQMD events (with impact parameter $b = 0\,\text{fm}$) were simulated in the center-of-mass frame.

- 60,000 events for $Au + Au$ at 1.23 AGeV. This system was measured by HADES in April 2012 and the data analysis is ongoing.
- 300,000 events for $Ar + KCl$ as measured by HADES in September 2005. The dilepton results are published [75].
- 50,000 events for $Au + Au$ at 20 AGeV. This system lies in the CBM energy regime and the in-medium emission rates are available for this energy (see Figure 2.1).
- 40,000 events for $In + In$ at 158 AGeV which has been measured by NA60 [36, 59] and serves as a control system since the Rapp-Wambach spectral function describes the fully acceptance corrected data very well [4].

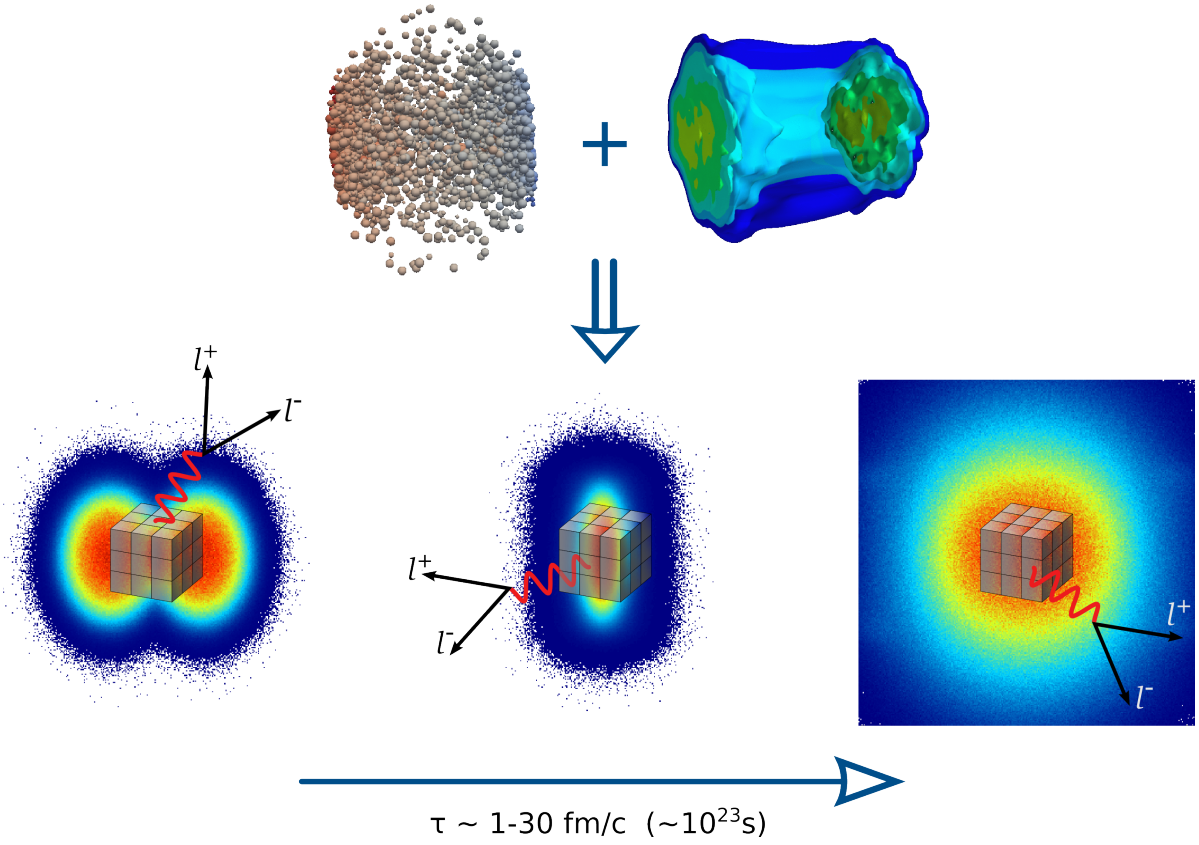

Figure 3.1: Sketch of an ensemble of Au+Au collisions radiating lepton pairs at three different time steps together with a space-time grid indicating the coarse-graining procedure. The color code indicates the particle density. The coarse-graining procedure combines some of the advantages of both transport and hydrodynamic descriptions. Visualizations for transport and hydro are taken from [37, 108].

Figure 3.2 shows a projection of two colliding nuclei ($Au+Au$ at 1.23 AGeV) for different time steps. The color code indicates the densities of particles in a given region of space. During the first few fm/c the nuclei penetrate each other until the densest stage of the collision is reached after about 13 fm/c. After that, the system starts to expand.

Figure 3.3 gives the same projection for $Au+Au$ at 20 AGeV for which the different stages of the collision progress much faster.

The fireball evolution is then divided into a grid of space-time cells. The spacial volume is discretized into 21^3 cubic cells of size $\delta x\,\delta y\,\delta z = 1\,\mathrm{fm}^3$ covering 10.5 fm in each direction from the center. The temporal grid is chosen as 30 time steps with a size of $\delta t = 1$ fm/c for the three systems at SIS18 and FAIR energies, while for the $In+In$ collision system the time steps are adapted to $\delta t = 0.5$ fm/c to account for the faster evolution at high energies. With such a volume and time span of the grid, covering in total $21^3 \times 30 \sim 280.000$ cells, the colliding systems are reasonably well contained inside the 4-volume to describe the whole evolution from first-chance collisions to the freeze-out.

The following sections will focus mostly on the two collision systems measured by HADES, namely $Au+Au$ at a beam energy of 1.23 AGeV, corresponding to a center-of-mass energy per nucleon of $\sqrt{s_{NN}} = 2.4$ GeV, and $Ar+KCl$ at a beam energy of 1.76 AGeV, corresponding to $\sqrt{s_{NN}} = 2.6$ GeV. For the subsequent discussion the cells can be divided up into two classes. One can define an inner cube of cells covering a volume of $7^3 \times 1\,\mathrm{fm}^3$ around the collision center and an outer shell of cells containing in total $(21^3 - 7^3)\,\mathrm{fm}^3$. The "radius" (3.5 fm) is about half the system radius $R_{Au} \simeq 6.5$ fm. For the smaller $Ar+KCl$ system the size of the inner cube is reduces to include only 3^3 cells.

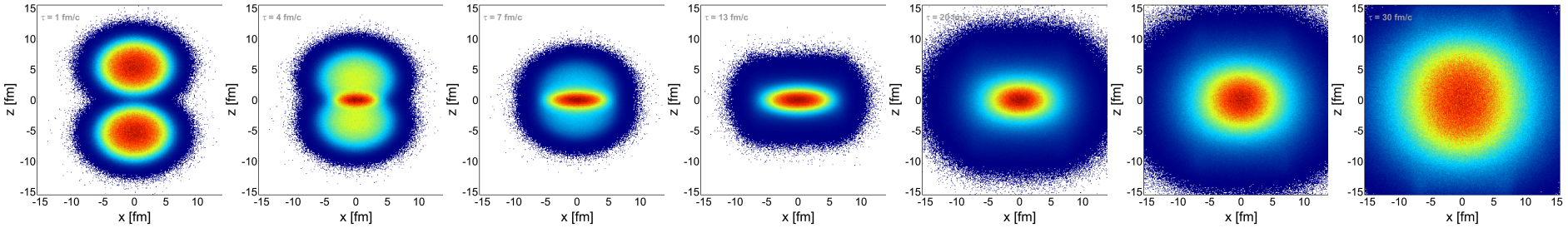

Figure 3.2: Fireball evolution for $Au+Au$ at 1.23 AGeV plotted at different time steps (from left to right: $\tau = 1$ fm/c, 4 fm/c, 7 fm/c, 13 fm/c, 20 fm/c, 24 fm/c, 30 fm/c). The beam direction is along the vertical axis. The color scheme indicates the density of particles in a given region.

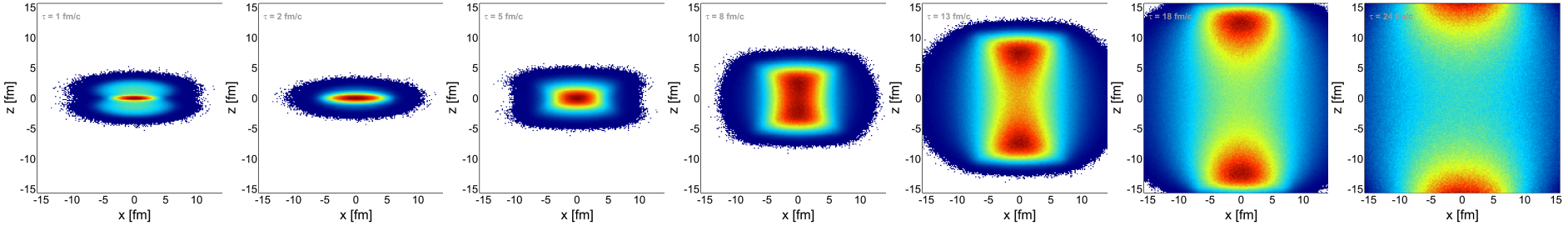

Figure 3.3: Fireball evolution for $Au+Au$ at 20 AGeV plotted at different time steps (from left to right: $\tau = 1$ fm/c, 2 fm/c, 5 fm/c, 8 fm/c, 13 fm/c, 18 fm/c, 24 fm/c). The beam direction is along the vertical axis. The color scheme indicates the density of particles in a given region.

3.3 Check for System Thermalization

The first prerequisite which has to be checked is whether the above mentioned reactions produce equilibrated matter, i.e., do the produced particles undergo sufficient rescattering to justify the notion of an interacting medium characterized by bulk thermodynamic variables. There are two rather independent measures which have been used to test if the matter in a given space-time cell has reached thermal equilibrium.

The first observable is the number of binary interaction, i.e., collisions or decays a given particle in a cell has experienced so far. A nucleon traversing the medium created in the hot and dense fireball scatters off other baryons and mesons via elastic and inelastic collisions. In UrQMD the number of collisions a nucleon experienced so far in an event is kept even if the nucleon gets excited into a resonance which later decays back into a nucleon. A sketch of this successively increasing number of collisions n_{coll} is depicted with the red numbers in brackets on the left panel of Figure 3.4. The middle panel shows the distributions of nucleons per event which have undergone n_{coll} interactions or decays at a certain point in time in a $Au+Au$ event at 1.23 AGeV. For comparison the same plot is shown on the left for In+In collisions at 158 AgeV for all particles.

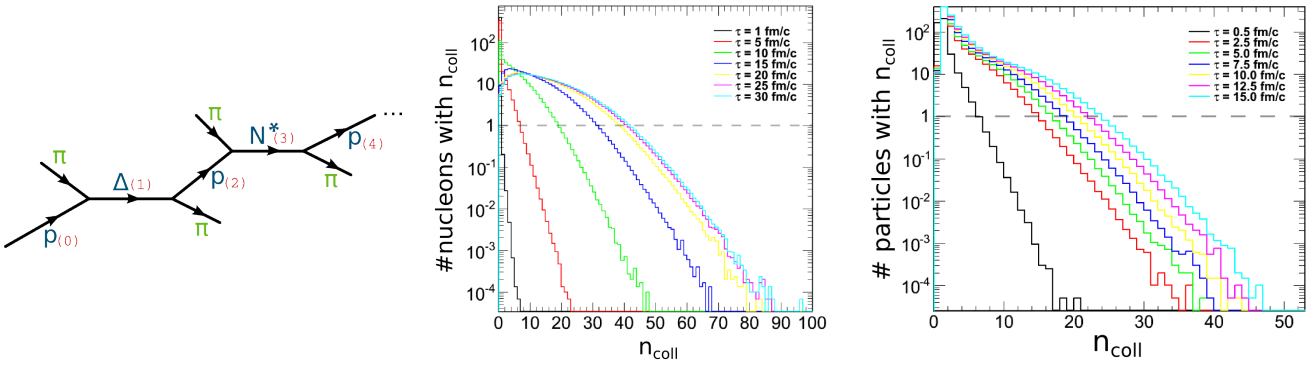

Figure 3.4: Left: Sketch of a nucleon traversing through the medium. It interacts with other nucleons or mesons to form resonances which subsequently decay back into nucleons. The number of collisions experienced by the nucleon successively increases indicated by the red numbers in brackets next to the nucleons or resonances. Middle: Distribution of n_{coll} of nucleons per $Au+Au$ event. The different colored lines indicate the distribution at different time steps. Right: Distribution of n_{coll} of all particles per $In+In$ event at 158 AGeV. The different colored lines indicate the distribution at different time steps.

In the first 15 to 20 fm/c the distribution for the $Au+Au$ collisions rapidly changes indicating that many collisions happen in the system which help to equilibrate the medium. For the high energy $In+In$ system this equilibration happens much faster, as many scatterings happen in the first few fm/c and indeed this system can successfully be modeled with hydrodynamics [4, 114].

This can be further quantified by investigating how the longitudinal momentum p_Z distributions of the incoming nucleons change in the early stages between first impact and full overlap. Figure 3.5 shows these distributions for the central cell at different steps in time. After only 4 fm/c (upper row, middle panel) a Gaussian distribution around $p_Z = 0$ has already formed from the nucleons which have collided three or more times, while the nucleons with two or less collisions still carry the momenta of the incoming nuclei. After 7 fm/c (lower row, middle panel) the Gaussian component makes up already about 80% of the nucleons. In thermal equilibrium a (hadron) gas can non-relativistically be described by a Maxwell-Boltzmann distribution which has a Gaussian momentum spread in each direction p_X, p_Y, p_Z. While the momentum in the transverse directions p_X and p_Y has a Gaussian shape during the whole time evolution due to the symmetry in central collisions, the development of this Gaussian component in the longitudinal momentum direction indicates a remarkably rapid trend towards thermalization.

A second measure for the thermalization of the medium are M_T spectra of particles. In an equilibrated system the $\frac{1}{M_T^{3/2}} \frac{dN}{dM_T}$ distribution should exhibit an exponential behavior. The derivation of this relation can be found in the appendix 6.2. Figure 3.6 shows the corresponding spectra obtained for pions in two different space-time cells together with exponential fits to guide the eye (for more details see section 3.5).

The results of this section hint towards a fast thermalization of the medium in many space-time cells, thus, allowing a meaningful assignment of values for the thermodynamic bulk properties to these cells.

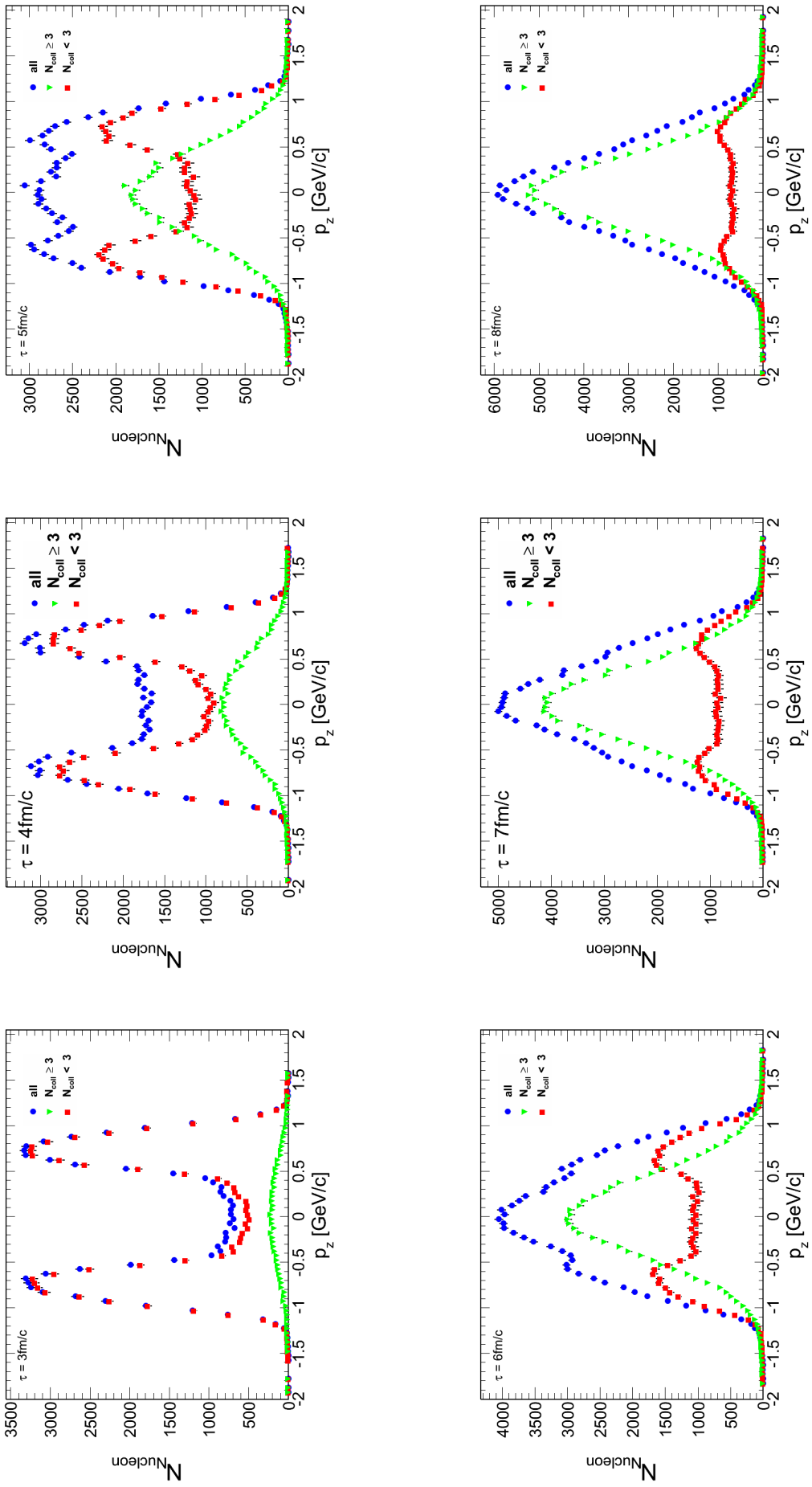

Figure 3.5: Distribution of the longitudinal momentum p_Z of nucleons in the ensemble of central $Au + Au$ collisions for different time steps (upper row from left to right: 3 fm/c, 4 fm/c, 5 fm/c; lower row from left to right: 6 fm/c, 7 fm/c, 8 fm/c) in the central cell. The blue circles refer to all nucleons, while the red squares show only nucleons which have experienced less than 3 collisions. Nucleons with three or more interactions are indicated by the green triangles.

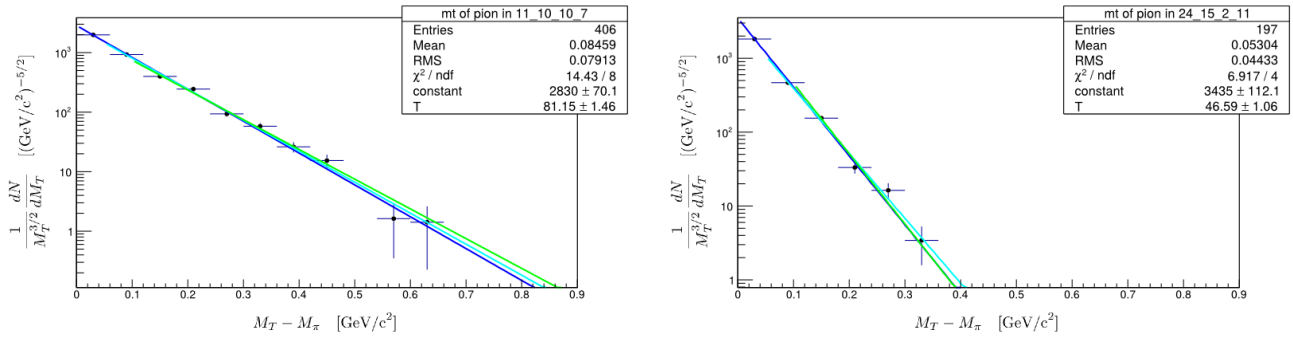

Figure 3.6: M_T spectrum of pions in a given space-time cell fitted with an exponential function. The different colored lines show the fit functions obtained by using different fit ranges.

3.4 Determination of Effective Baryon and Pion Densities

The bulk properties of the medium, like temperature and densities, are only defined properly in the local rest frame (LRF). While the system as a whole is simulated in the center-of-mass frame at rest, the restriction to a specific cell, differing from the cell at the center of the collision zone, leads to a net motion of the particles in that cell due to the collective radial expansion of the fireball. To extract the local densities and temperature one therefore has to determine the net velocity $\vec{\beta}$ of the particles in a cell and boost all hadron momenta back into the local rest frame which is co-moving with the same net velocity as the particles. Thus, the net velocity of the particles vanishes in this frame. A sketch of this procedure is shown in Figure 3.7.

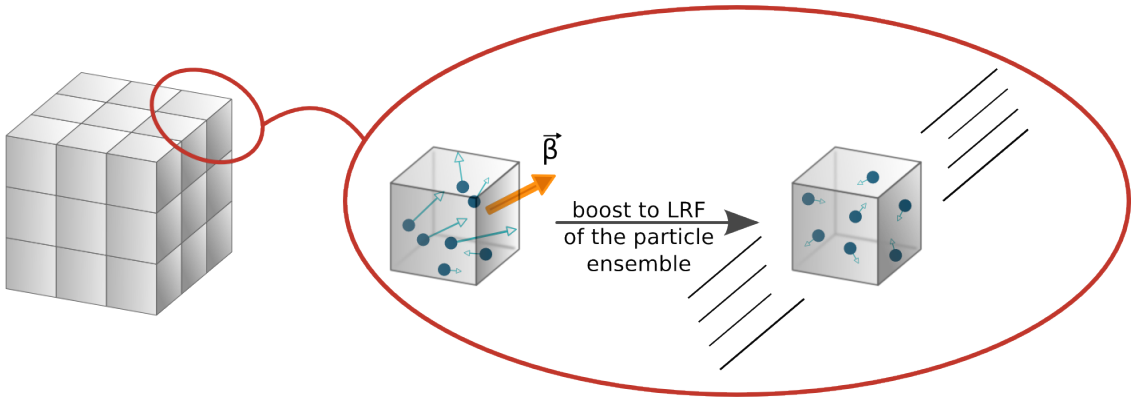

Figure 3.7: In a specific non-central cell, the particles have a net velocity $\vec{\beta}$ due to the radial expanding fireball. As density and temperature are only defined in the local rest frame, one has to boost the particle momenta into this frame which moves along with the same $\vec{\beta}$ so that the net velocity of the particles vanishes.

The standard (f14) output file of UrQMD provides for every time step the position and 4-momentum of each particle. Treating the particles as point-like objects at these positions would lead to a overestimation of the density as hadrons are in reality extended entities with a typical size of 1 fm. It is therefore natural to consider the particles as smeared 3-dimensional Gaussian packets centered around the given position with a width of $\sigma = 1$ fm.

Figure 3.8 sketches the Gaussian smearing procedure. Note that on the left hand side only one point particle accounts for the properties of the highlighted cell, while on the right hand side every particle contributes not only to the cell in which its center is located, but also to the adjacent cells. This makes the determination of the cell's properties numerically more stable [115–118].

To account for the Lorentz-contraction of the incoming beams the Gaussians are contracted in beam direction by a factor $\gamma_Z = \left(1-\beta_Z^2\right)^{-1/2}$ with the velocity of the particle in z-direction β_Z. The fraction P_i of particle i with position (x_i, y_i, z_i) in a given cell is then determined by the normalized 3D-Gaussian integrated over that cell

$$P_i = \int_{\text{cell}} \left(\frac{1}{\sqrt{2\pi}\sigma}\right)^3 \gamma_z \exp\left(-\frac{1}{2}\,\frac{(x-x_i)^2+(y-y_i)^2+\gamma_Z^2(z-z_i)^2}{\sigma^2}\right). \tag{3.1}$$

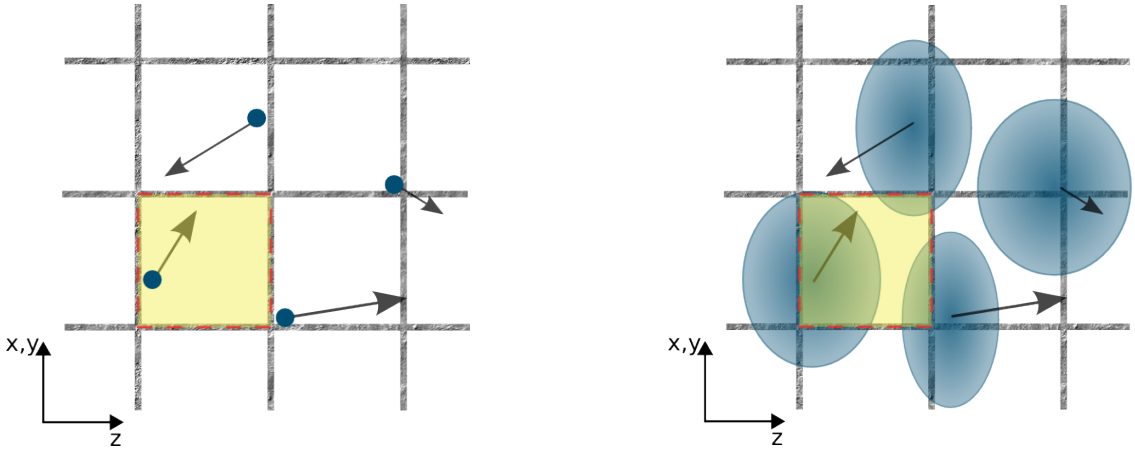

Figure 3.8: Sketch of the method to obtain smooth space-time distributions of the particle densities. Instead of counting point particles (left panel) to determine the density in a cell, the particles are initialized as smeared out Gaussian packets which are contracted in beam direction (right panel). The density in a cell is then obtained by integrating over the content in the cell.

The baryon 4-current $j^{\mu}_{B,CF}$ in the computational frame, i.e., the center-of-mass frame in which the UrQMD events are simulated is given by

$$j^{\mu}_{\mathrm{B,CF}} = \frac{1}{\delta x \delta y \delta z} \left\langle \sum_{\text{particles i}} \frac{p^{\mu}_i}{p^0_i} P_i \, f_{\mathrm{PID}} \right\rangle_{\text{N UrQMD events}} = \begin{pmatrix} \varrho_{\mathrm{CF}} \\ \varrho_{\mathrm{CF}} \, \vec{\beta}_{\mathrm{Cell}} \end{pmatrix} \tag{3.2}$$

where $\delta x \delta y \delta z$ is the volume of the cell, p^{μ}_i is the 4-momentum of particle i, p^0_i its energy and the bracket $\langle \cdot \rangle_N$ stands for the average over N UrQMD events. The weighting factor f_{PID} depends on the particle species and determines the type of baryon current which is calculated (net, total, effective):

$$f^{\mathrm{net}}_{\mathrm{PID}} = \begin{cases} +1, & \text{for baryons,} \\ -1, & \text{for antibaryons,} \\ 0, & \text{for mesons} \end{cases} \tag{3.3}$$

$$f^{\mathrm{total}}_{\mathrm{PID}} = \begin{cases} 1, & \text{for (anti-)baryons,} \\ 0, & \text{for mesons} \end{cases} \tag{3.4}$$

$$f^{\mathrm{eff}}_{\mathrm{PID}} = \begin{cases} 1, & \text{for (anti-)nucleons,} \\ \frac{1}{2}, & \text{for (anti-)baryon resonances,} \\ 0, & \text{for mesons.} \end{cases} \tag{3.5}$$

Note that once the baryon 4-current is obtained also the net velocity vector $\vec{\beta}_{\mathrm{cell}}$ of the baryons in the cell is known. As illustrated above, the local rest frame is the frame in which the baryon current vanishes. By means of a Lorentz transformation $\Lambda^{\mu\nu}(\vec{\beta})$ the 4-current in the local rest frame is calculated as

$$j^{\mu}_{\mathrm{B,LRF}} = \begin{pmatrix} \varrho_{\mathrm{B,LRF}} \\ \vec{0} \end{pmatrix} = j_{\mathrm{B,CF},\,\nu} \, \Lambda^{\mu\nu}(\vec{\beta}_{\mathrm{cell}}). \tag{3.6}$$

The baryon density is than determined as the time-component of the 4-current in the LRF. Performing the boost leads to

$$\varrho_{\mathrm{B,LRF}} = \frac{j^0_{\mathrm{B,CF}}}{\gamma_{\mathrm{cell}}}. \tag{3.7}$$

Figure 3.9 shows the net-baryon density evolution obtained for the central cell (left) and an inner cube of 5^3 cells (right) in different collision systems. For a short time at the beginning of a high energy collision the densities in the center can reach values of 10 times normal nuclear matter density, but the density quickly drops below ϱ_0 afterwards. At lower energies the maximum compression is reached after about $12-14\,\mathrm{fm/c}$ which is still well above ϱ_0 and the systems stay a long time $\sim 10-15\,\mathrm{fm/c}$ at these elevated densities.

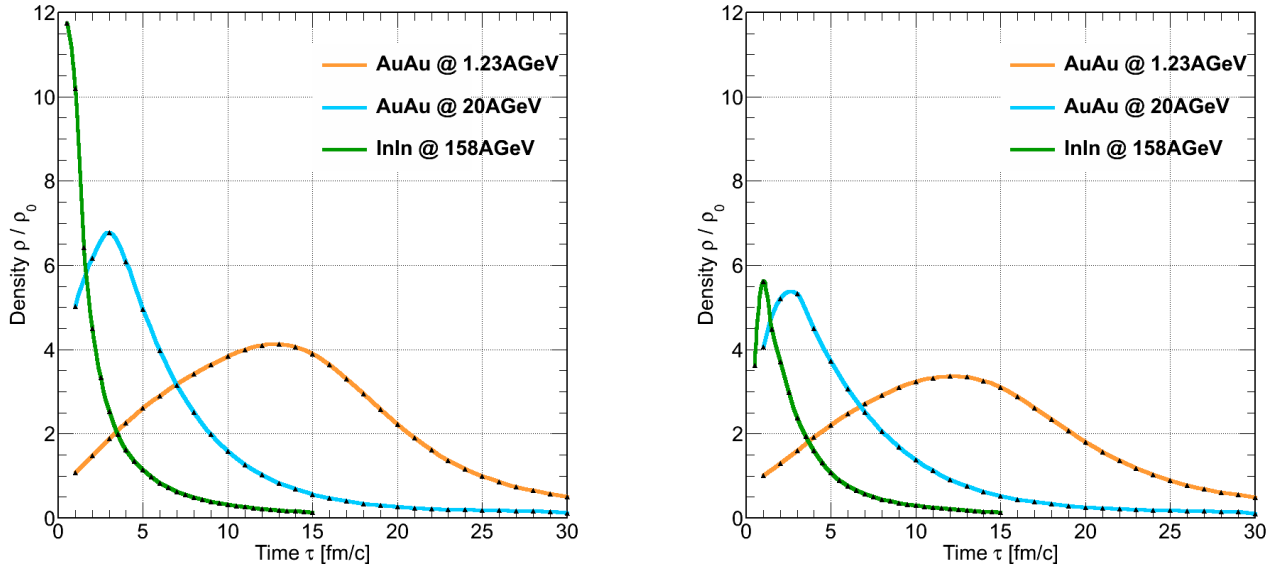

Figure 3.9: Evolution of the net-baryon density in the central cell (left) and an inner cube of 5^3 cells (right) in different collision systems: $In+In$ at 158 AGeV in green, $Au+Au$ at 20 AGeV in cyan and $Au+Au$ at 1.23 AGeV in orange.

Figure 3.10 illustrates the effective baryon density ϱ_{eff} profile at a fixed time $\tau = 13\,\mathrm{fm/c}$ for slices through the fireball at different values of the z-direction. A picture with all z-slices can be found in the appendix 6.3.

In the same way as the baryon density also the density of other particles, like Δ resonances or pions, can be determined which will become important for the calculation of the pion chemical potential in section 3.6. The pion density profile for different slices in z-direction is shown in Figure 3.11. In appendix 6.4 more z-slices can be found. Figure 3.12 and 3.13 demonstrate the smooth profile of β_X and β_Z in $Au+Au$ at 1.23 AGeV collisions for the time step $\tau = 13\,\mathrm{fm/c}$. Other slices in the z-direction for this time step are in appendix 6.5.

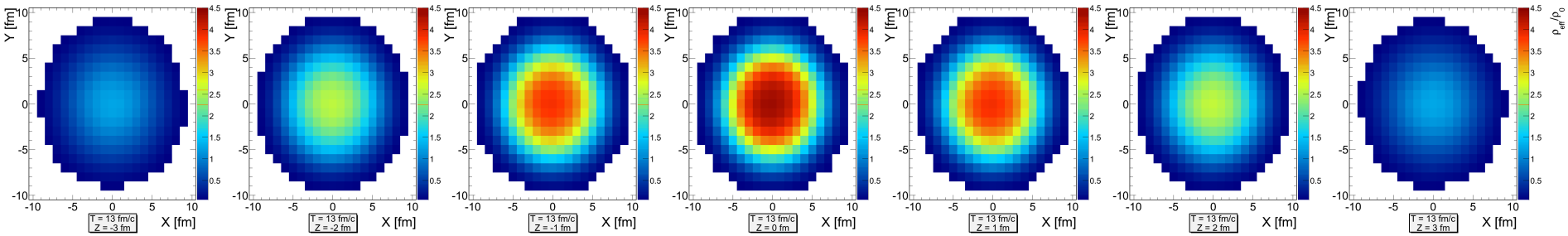

Figure 3.10: Profile plots (slices in z-direction) of the effective baryon density ϱ_{eff} in $Au+Au$ collisions at 1.23 AGeV at a fixed time step $\tau = 13$ fm/c. The range in x- and y-direction is from -10.5 fm to 10.5 fm. The z-slices shown from left to right are: $z = -3$ fm, $z = -2$ fm, $z = -1$ fm, $z = 0$ fm, $z = 0$ fm, $z = 1$ fm, $z = 2$ fm, $z = 3$ fm. The color scheme indicates densities of $0.5\varrho_0$ in blue and $4.5\varrho_0$ in red.

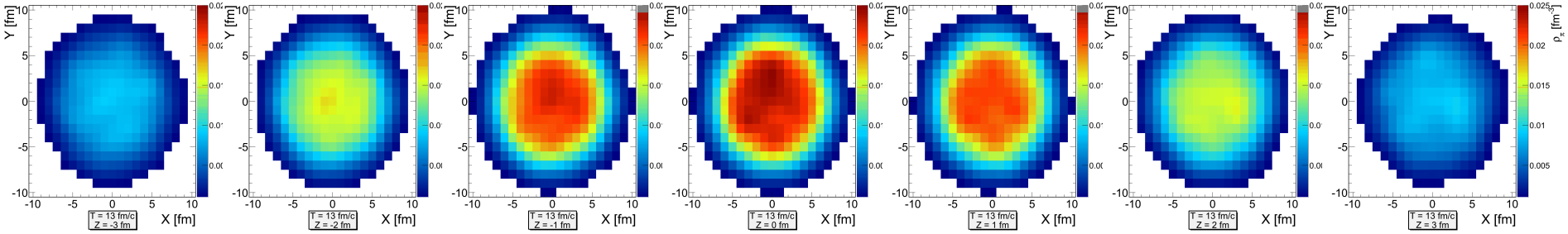

Figure 3.11: Profile plots (slices in z-direction) of pion density ϱ_π in $Au+Au$ collisions at 1.23 AGeV at a fixed time step $\tau = 13$ fm/c. The range in x- and y-direction is from -10.5 fm to 10.5 fm. The z-slices shown from left to right are: $z = -3$ fm, $z = -2$ fm, $z = -1$ fm, $z = 0$ fm, $z = 0$ fm, $z = 1$ fm, $z = 2$ fm, $z = 3$ fm. The color scheme indicates densities of 10^{-3} fm^{-3} in blue and $2.5 \cdot 10^{-2}$ fm^{-3} in red.

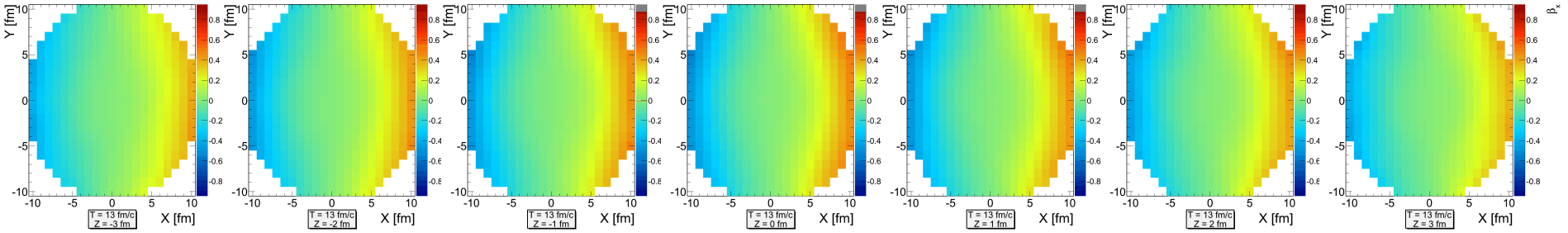

Figure 3.12: Profile plots (slices in z-direction) of the collective velocity β_X in $Au + Au$ collisions at 1.23 AGeV at a fixed time step $\tau = 13$ fm/c. The range in x- and y-direction is from -10.5 fm to 10.5 fm. The z-slices shown from left to right are: $z = -3$ fm, $z = -2$ fm, $z = -1$ fm, $z = 0$ fm, $z = 0$ fm, $z = 1$ fm, $z = 2$ fm, $z = 3$ fm. The color scheme indicates velocities β_X of $-0.85 \cdot c$ in blue and $0.85 \cdot c$ in red.

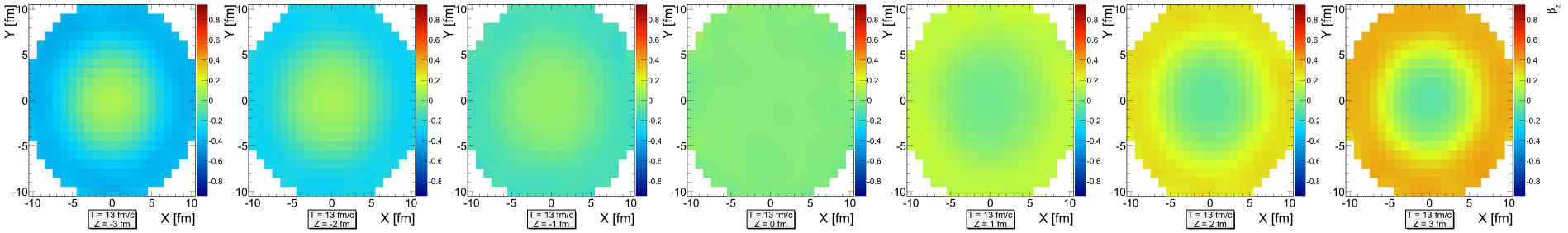

Figure 3.13: Profile plots (slices in z-direction) of the collective velocity β_Z in $Au + Au$ collisions at 1.23 AGeV at a fixed time step $\tau = 13$ fm/c. The range in x- and y-direction is from -10.5 fm to 10.5 fm. The z-slices shown from left to right are: $z = -3$ fm, $z = -2$ fm, $z = -1$ fm, $z = 0$ fm, $z = 0$ fm, $z = 1$ fm, $z = 2$ fm, $z = 3$ fm. The color scheme indicates velocities β_Z of $-0.85 \cdot c$ in blue and $0.85 \cdot c$ in red.

3.5 Determination of Temperature

The second input variable needed for the thermal Bose factor f^B and also the Rapp-Wambach spectral function is the local temperature. To extract this quantity the transverse mass M_T spectra can be used which should show an exponential shape in thermal equilibrium. One can either use the spectra normalized with M_T^{-2} and restrict the particles used to fill the spectra to a narrow interval around midrapidity $|y| \leq 0.5$ or normalize the spectra with $M_T^{-3/2}$ and include particles with all rapidities. For a detailed derivation see appendix 6.2. It has been checked that within the uncertainties induced by the reduced statistics the M_T^{-2} spectra give the same results for the temperature as the spectra containing all rapidities.

The slope extracted from an exponential fit to the distribution is normally called inverse slope parameter T_{eff} and not temperature. The collective motion of the fireball in the transverse direction blue-shifts the transverse momentum p_T and thus also M_T which spoils a direct interpretation of the extracted slope as a temperature.

Since the collective velocity in each space-time cell is known from the determination of the densities (see section 3.4) one can boost the momentum of every particle in a given cell back into the local rest frame. This eliminates the blue-shift and allows to connect the extracted slope with a temperature.

If there is enough statistics available, i.e., at least a minimum amount of particles of a particular species in a certain cell, one can fit an exponential function to the rest frame $M_T^{-3/2}$ spectrum. Examples of the fits are shown in Figure 3.6 in section 3.3. Different fit ranges ($[0-2]\,\text{GeV/c}^2$ in blue, $[0.05-2]\,\text{GeV/c}^2$ in cyan and $[0.1-2]\,\text{GeV/c}^2$ in green) are used to ensure the quality of the extracted temperature. In most cases the variation amounts to 5-10%. To quantify which fit gives the best description of the data there are two parameters, namely the fit error of the temperature parameter and the χ^2 of the fit. These can be used to derive weights which favor fits with low parameter error and a reduced χ^2 close to 1. With those a weighted average of the inverse slope parameters, obtained by varying the fit range, can be calculated. The resulting value is then used as the temperature of the cell.

The procedure is carried out for different particles (pions, thermal nucleons with $n_{\text{coll}} \geq 3$ and Δ resonances) to check how much the temperature depends on the particle type used for the fits.

Figure 3.14 depicts the temperature profile for different slices through the fireball along the z-direction obtained with pions in $Au+Au$ at time step $\tau = 13\,\text{fm/c}$, while Figure 3.15 illustrates the same for the $Ar+KCl$ system at time step $\tau = 9\,\text{fm/c}$. One can see that for the heavier $Au+Au$ collision system more cells are equilibrated and will contribute to the dilepton production, even though the $Au+Au$ system is at $\tau = 13\,\text{fm/c}$ in the very dense stage, while the matter in $Ar+KCl$ collisions at $\tau = 9\,\text{fm/c}$ is already expanding.

For pions in $Au+Au$ collisions at 1.23 AGeV the individual cells reach a temperature up to $90-95\,\text{MeV}$. The average over 7^3 inner cells, however, gives a value which is about 10 MeV lower. For thermal nucleons the temperature in the cells reaches up to 110 MeV and the fluctuations in temperature between neighboring cells are smaller as compared to pions which can be explained by particle multiplicities.

The temperatures extracted with pions in $Ar+KCl$ at 1.76 AGeV are about 10 MeV higher than the maximum pion temperatures in $Au+Au$ and drop much faster due to the smaller system size. In appendix 6.6 and 6.7 more z-slices with temperature profiles are shown, including the plots for the temperatures extracted with thermalized nucleons.

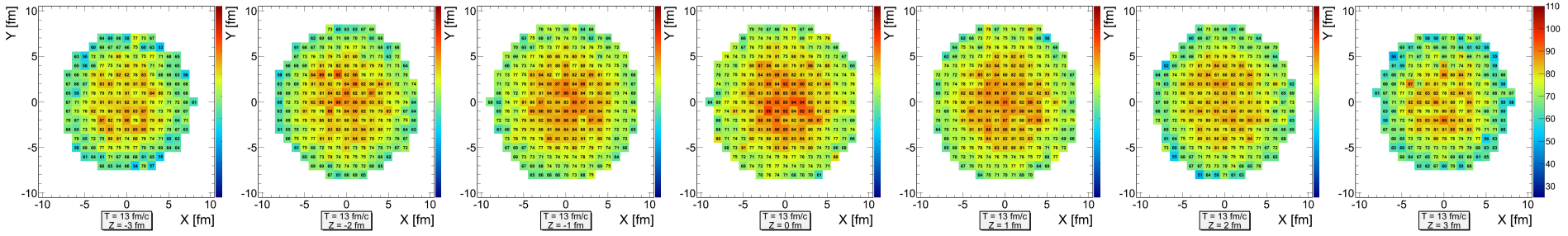

Figure 3.14: Profile plots (slices in z-direction) of temperature T extracted with pions in $Au+Au$ collisions at 1.23 AGeV at a fixed time step $\tau = 13$ fm/c. The range in x- and y-direction is from -10.5 fm to 10.5 fm. The z-slices shown from left to right are: $z = -3$ fm, $z = -2$ fm, $z = -1$ fm, $z = 0$ fm, $z = 0$ fm, $z = 1$ fm, $z = 2$ fm, $z = 3$ fm. The color scheme indicates temperatures of 25 MeV in dark blue and 110 MeV in dark red.

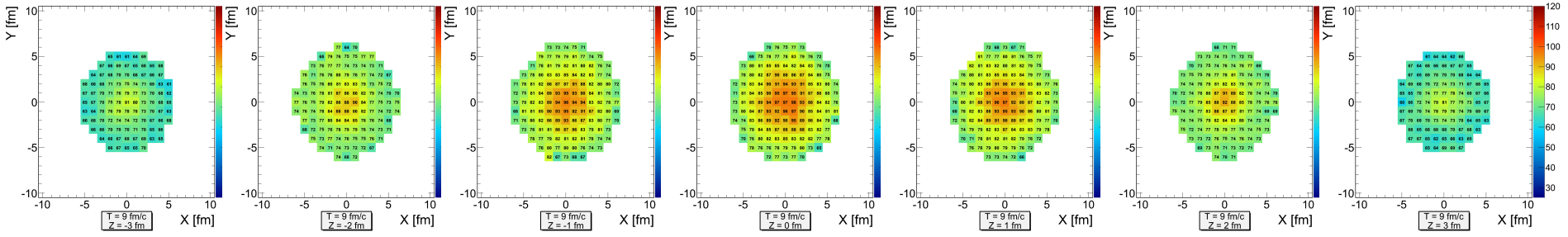

Figure 3.15: Profile plots (slices in z-direction) of temperature T extracted with pions in $Ar+KCl$ collisions at 1.76 AGeV at a fixed time step $\tau = 9$ fm/c. The range in x- and y-direction is from -10.5 fm to 10.5 fm. The z-slices shown from left to right are: $z = -3$ fm, $z = -2$ fm, $z = -1$ fm, $z = 0$ fm, $z = 0$ fm, $z = 1$ fm, $z = 2$ fm, $z = 3$ fm. The color scheme indicates temperatures of 25 MeV in dark blue and 120 MeV in dark red.

Figure 3.16 shows the extracted temperatures of different particles in the central cell and the inner cube of 7^3 cells in $Au+Au$ in the upper row as well as for the central cell and the inner cube of 3^3 cells in $Ar+KCl$ in the lower row. In the following the temperature extracted with pions is taken for the calculation of the dilepton production, as pions play the most important role in the production of the ρ meson and the excitation of resonances which can decay into dileptons.

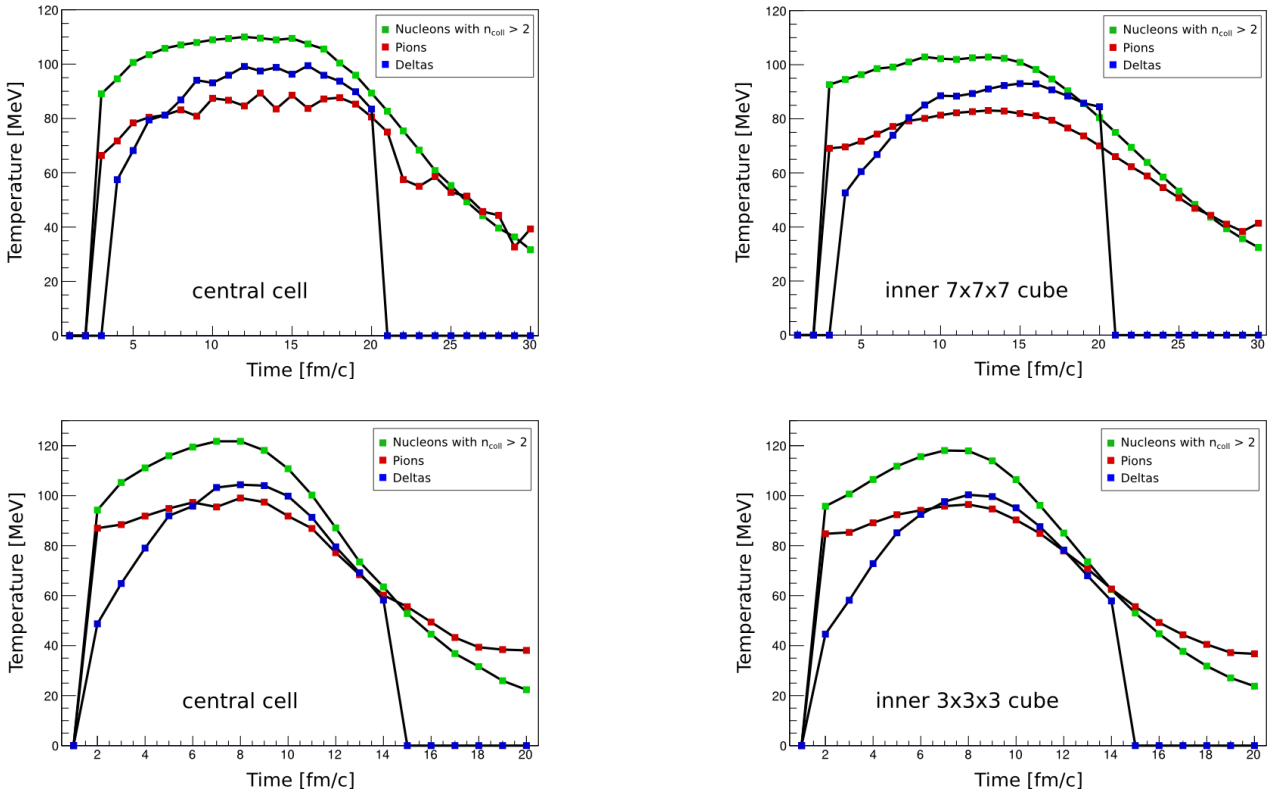

Figure 3.16: Evolution of the temperature extracted from the slope of M_T spectra for different particles (nucleons with $n_{\text{coll}} \geq 3$ in green, pions in red and Δ in blue). The upper row shows the results for $Au+Au$ at 1.23 AGeV, while in the lower row the temperature in the $Ar+KCl$ system at 1.76 AGeV is plotted. The left panels correspond to the central cell, the right panels to an average over the inner cube of 7^3 or 3^3 cells respectively.

3.6 Determination of Pion Chemical Potential and Fugacity Exponent

The remaining input for the calculation of dilepton spectra is the effective pion chemical potential μ_π. Once the pion density ϱ_π (see section 3.4) and temperature T (see section 3.5) in each cell is known, the pion chemical potential is straightforwardly obtained with the use of the Boltzmann approximation, thus, neglecting quantum effects. A detailed derivation is provided in appendix 6.8.

Figure 3.17 shows the evolution of the pion chemical potential together with temperature and effective baryon density in the inner cube of $Au+Au$ and $Ar+KCl$.

As discussed in section 2.5 in the later stages of the collision a sizable pion chemical potential builds up, indicating that there are more pions in the system than one would expect at that temperature. The enhanced pion abundance leads to an increased possibility to create resonances and ρ mesons as compared to a system in chemical equilibrium which in turn raises the yield of dileptons emanating from the fireball. To account for this effect the equilibrium dilepton rates have to be augmented by a fugacity factor $z_\pi^k = \exp(\mu_\pi/T)^k$. The exponent k is determined by the number of pions needed in the main production mechanism of ρ mesons at a given energy.

At high energies most ρ mesons are formed in $\pi-\pi$ annihilation which is a 2-π process, leading to a fugacity factor z_π^2 to be include in the dilepton production rate. At lower energies, however, resonance decays play an important role in the production of ρ mesons. Depending on the number n of pions which were involved to create

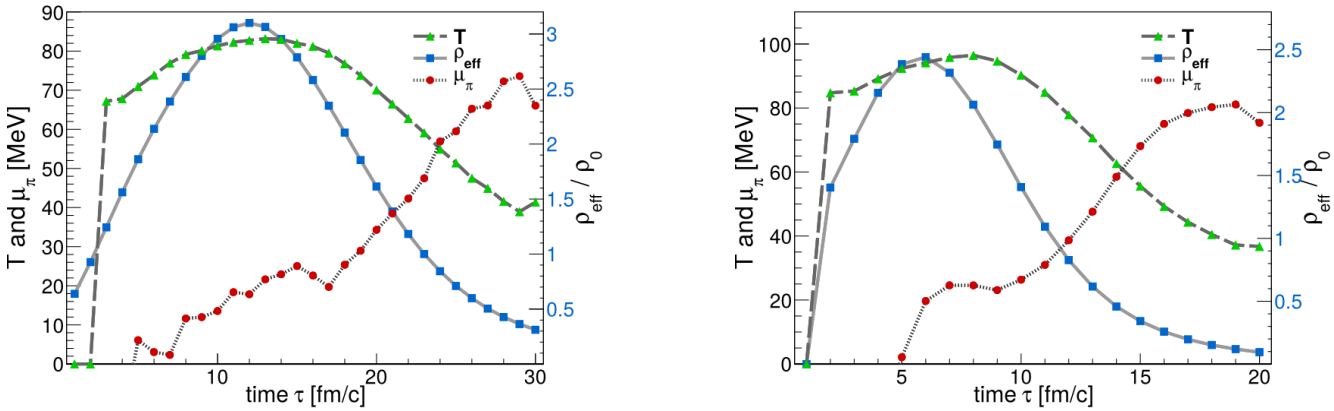

Figure 3.17: Evolution of the temperature T in green, effective baryon density ϱ_{eff} in blue (right vertical scale) and pion chemical potential μ_π in red for the inner cubes of $Au + Au$ at 1.23 AGeV (left) and $Ar + KCl$ at 1.76 AGeV (right).

the resonance in the first place, the production of ρ in decays is considered a n-π process. Figure 3.18 illustrates the production of ρ mesons via $\pi - \pi$ annihilation (left panel) and resonance decays. The $N^*(1520)$ resonance in the middle panel is produced in an inelastic collision of a proton and a π^- and subsequently decays into a neutron and a ρ meson. This constitutes a 1-π process. The resonance excitation on the right proceeds completely without pions, resulting in a 0-π process.

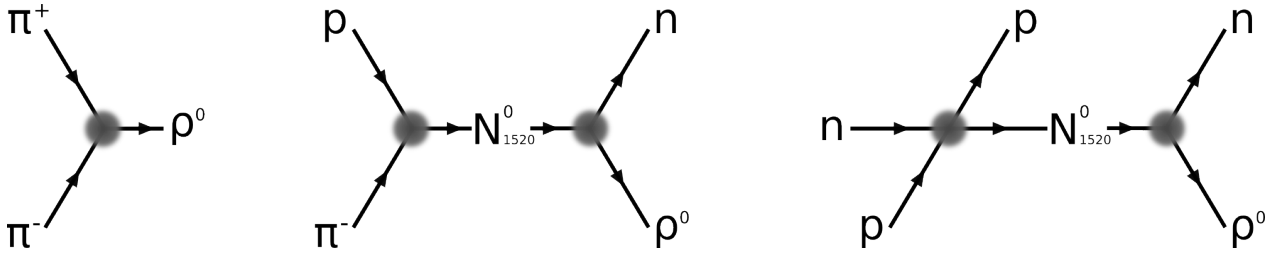

Figure 3.18: Sketch of different production mechanisms for the ρ meson: the annihilation of pions as a 2-π process on the left, a 1-π resonance excitation in the middle and a 0-π process on the right.

UrQMD offers through the f15 collision history file the opportunity to check how the ρ mesons are predominantly produces at HADES energies. Each ρ produced during an event is tested for its origin. If it is not produces in the annihilation of two pions, but comes from a resonance decay, the parent particles are traced back through the whole fireball evolution to determine how many pions were involved to cook up the resonance which finally produced the ρ. In some cases this involved the back-tracking of the particle over 10-15 previous collisions. Two examples are shown in Figure 3.19.

To acquire enough statistics this procedure was done for 20.000 $Au + Au$ collisions at HADES energies. It turns out that 83% of the ρ mesons are produces in resonance decays at these lower beam energies, while only 17% are created in $\pi - \pi$ annihilation. The fraction of ρ mesons coming from decays can be apportioned into

- 0-π: 26% of the resonances are excited in nucleon-nucleon interactions without pions,
- 1-π: 40% of the resonances are produces in interactions involving one pion,
- 2-π: 14% of the resonances need two pions before decaying into the ρ,
- 3-π: 2% of the resonances are excited through scatterings with three pions,
- 4-π: 1% of the resonances are produced in collisions involving four pions.

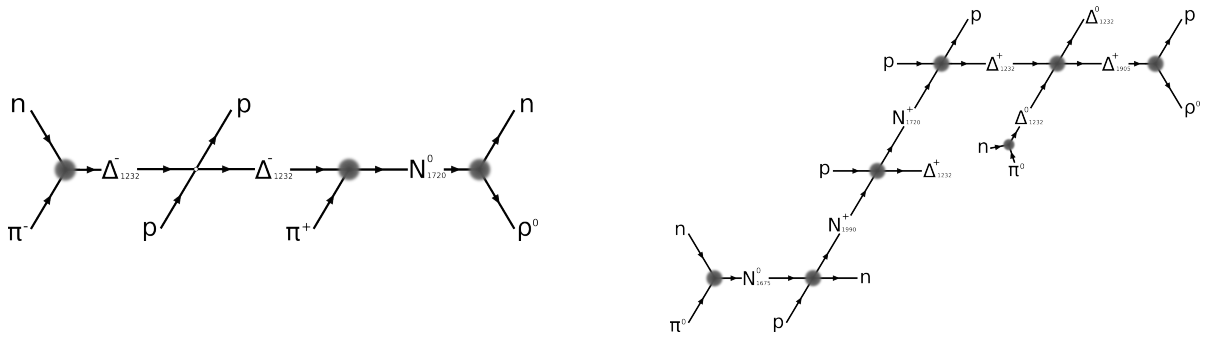

Figure 3.19: Sketch of two chains of resonance excitations which finally result in the production of a ρ meson, both constituting 2-π processes. The blurry gray circles indicate inelastic collisions, while the small white dot stands for a elastic collision.

The mean number of pions needed to produce a ρ mesons can be obtained by taking a weighted average

$$0 \cdot 26\% + 1 \cdot 40\% + 2 \cdot (17 + 14)\% + 3 \cdot 2\% + 4 \cdot 1\% = 1.12\,. \tag{3.8}$$

Thus, the exponent k of the fugacity factor which should be used at lower energies is close to 1, instead of 2 at high energies.

3.7 Calculation of Dilepton Spectra

The integral over the fireball space-time evolution (see equation (2.20)) to obtain the dilepton yield $\frac{dN_{ll}}{dM}$ from the dilepton emission rate $\frac{dR}{dM} = \frac{dN_{ll}}{dM\,d^4x}$ reduces in the coarse-graining approached to a sum over the contributions $\frac{dR_i}{dM}$ of all cells i times the 4-volume of the cell $\delta x\,\delta y\,\delta z \cdot \delta t$

$$\frac{dN_{ll}}{dM} = \int d^4x\,\frac{dR}{dM} = \sum_i^{\text{all cells}} \frac{dR^i}{dM} \quad \delta x\,\delta y\,\delta z\,\delta t\,. \tag{3.9}$$

The same is true for $\frac{dN_{ll}}{dM\,dp_T\,dy}$. The rate for each cell involves the Rapp-Wambach spectral function with the temperature T_{cell} and baryon density $\varrho_{\text{eff, cell}}$ in this cell as input parameters. It would be computationally very expensive to calculate the rate for each cell with the exact values for temperature and density.

Instead the Rapp-Wambach spectral function $\text{Im}D_\rho^{\text{inmed}}(M, q; T, \varrho_{\text{eff}})$ is calculated on a grid of temperatures and effective baryon densities only once. Its value in a given cell is then obtained by bilinear interpolations between the nearest neighboring points on the grid. The grid points are spaced 5 MeV in the temperature direction and $0.1\varrho_0$ in the density direction.

The strategy for calculating the $\frac{dN_{ll}}{dM\,dp_T\,dy}$ spectrum is then to pick a bin with values M, p_T and y for mass, transverse momentum and rapidity. These can be converted into the corresponding values of 3-momentum q and energy q_0 (see appendix 6.1). As a next step the temperature T_{cell}, effective baryon density $\varrho_{\text{eff, cell}}$, pion chemical potential $\mu_{\pi,\text{cell}}$ and collective velocity $\vec{\beta}_{\text{cell}}$ of the cell (as determined earlier) are retrieved from their storage location.

With the help of the 4-velocity $u^\mu = \gamma_{\text{cell}}\left(1, \vec{\beta}_{\text{cell}}\right) = \gamma_{\text{cell}}\left(1, \beta_{T,\text{cell}}, \beta_{Z,\text{cell}}\right)$ the Lorentz scalar $q \cdot u$ can be calculated

$$q^\mu u_\mu = \gamma_{\text{cell}}\left(q_0 - \beta_{T,\text{cell}} p_T - \beta_{Z,\text{cell}}\, m_T \sinh(y)\right). \tag{3.10}$$

The dilepton rate for a given cell and the specific (M, p_T, y) bin follows from

$$\begin{aligned}\frac{dR}{dM\,dp_T\,dy} &= M\,p_T\,2\pi \frac{dN_{ll}}{d^4x\,d^4q} \\ &= M\,p_T\,2\pi\,\frac{\alpha_{\text{EM}}^2}{\pi^3}\,\frac{m_\rho^4}{g_\rho^2}\,\frac{L(M^2)}{M^2}\,z_\pi^k(\mu_{\pi,\text{cell}}; T_{\text{cell}})\,f^B(q^\mu u_\mu; T_{\text{cell}}) \cdot \\ &\qquad \cdot \left(-\text{Im}D_\rho^{\text{inmed}}(M, \sqrt{(q\cdot u)^2 - M^2}; T_{\text{cell}}, \varrho_{\text{eff, cell}})\right),\end{aligned} \tag{3.11}$$

where the value of the spectral function for the cell's temperature and density is obtained by the interpolation between appropriate nearest neighbors on the $T - \varrho$ grid.

The result of all (M, p_T, y) bins can be saved in a 3-dimensional histogram for each cell. The dilepton spectrum is than given by adding up all cells (histograms) and multiplying every bin content by the cell's 4-volume.

The invariant mass spectrum can either be obtained separately, similar to the procedure described above, or via projection of the differential $\frac{dN_{ll}}{dM\,dp_T\,dy}$ spectrum onto the mass axis

$$\frac{dN_{ll}}{dM} = \int dp_T\,dy\,\frac{dN_{ll}}{dM\,dp_T\,dy} = \sum_{\text{all } p_t,y \text{ bins}} \frac{dN_{ll}}{dM\,dp_T\,dy}\Delta p_T \Delta y. \tag{3.12}$$

with the bin widths Δp_T and Δy respectively. The contribution of the hadronic continuum radiation to the dilepton spectra can be calculated likewise.

3.8 In-medium Dilepton Sampling with Pluto

The obtained dilepton spectra $\frac{dN_{ll}}{dM\,dp_T\,dy}$ can directly be utilized as input for the mass and momentum sampling of dileptons in Pluto. Figure 3.20 shows different dielectron distributions obtained in Pluto with the in-medium ρ contribution for $Au+Au$ at 20 AGeV [90] as input. The same is now possible for the other collision systems examined in this thesis and in general for any further system in the SIS18 to SPS energy range.

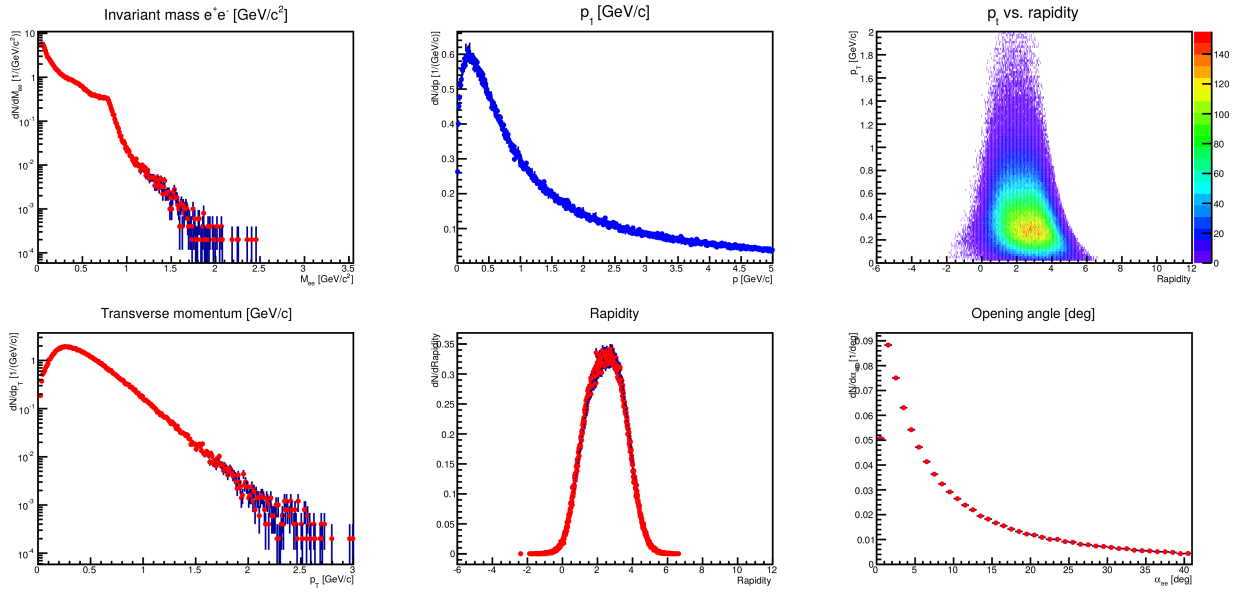

Figure 3.20: In-medium ρ dielectrons sampled with Pluto. In the upper row the invariant mass spectrum, the momentum spectrum of single electrons and a p_T vs. rapidity distribution is plotted. The lower row depicts transverse momentum, rapidity and opening angle distributions.

4 Results — Insights into the Hot and Dense Fireball

The coarse-graining procedure allows to divide the fireball evolution into 4-dimensional space-time cells. After checking for thermalization of the cells, the temperatures and densities in each of those cells can be extracted (see chapter 3). With these values the position of each cell in the temperature-density $T - \varrho_{\text{eff}}$ plane, similar to the QCD phase diagram, can be traced through the time evolution, revealing their trajectories. The upper row of Figure 4.1 depicts these trajectories for the inner cube of 3^3 cells characterizing the medium evolution in $Au + Au$ and $Ar + KCl$ at HADES energies. Note, however, that the relation between baryon density which is used in this plot and baryon chemical potential which is normally employed to draw the phase diagram of QCD matter is highly non-linear. The color code indicates the time step corresponding to the cells. Blue shades imply a cell in the early stages of a collision, while reddish points belong to cells in the late stages.The trajectories for all cells can be found in appendix 6.9 and 6.10.

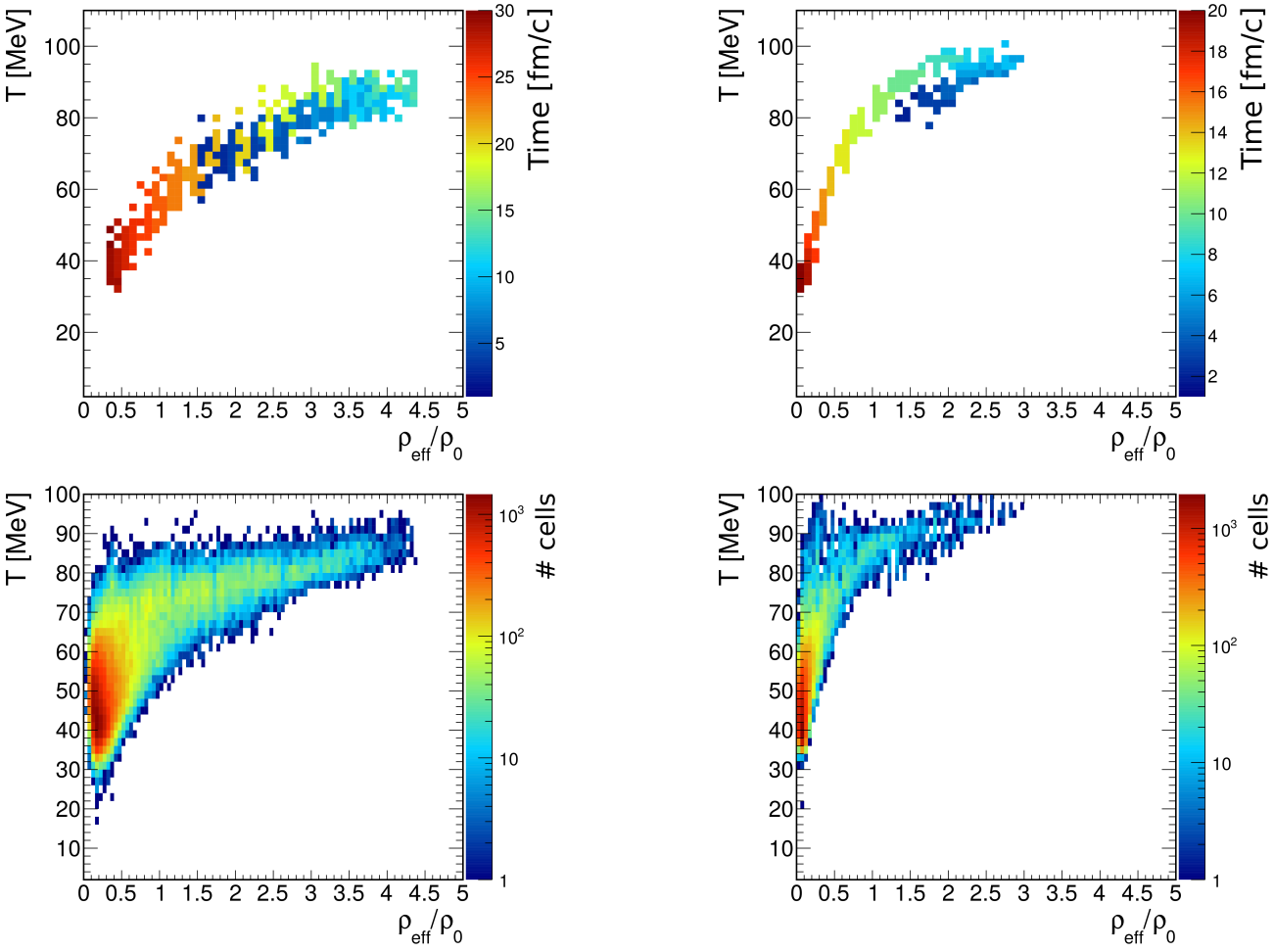

Figure 4.1: Upper row: Trajectories of the cells in the $T - \varrho_{\text{eff}}$ plane for $Au + Au$ at 1.23 AGeV on the left and $Ar + KCl$ at 1.76 AGeV on the right. In both cases the plotted cells are restricted to the inner 3^3 cube for better visibility of the evolution along the trajectory. Lower row: The color scheme in the $T - \varrho_{\text{eff}}$ plane indicates the total amount of cells contributing to a specific bin. $Au + Au$ is shown on the left, $Ar + KCl$ on the right.

The lower row of Figure 4.1 illustrates the total amount of cells contributing to a specific $T - \varrho_{\text{eff}}$ bin. More cells contribute to the thermal emission in the heavier $Au + Au$ system on the left where also higher densities are

reached. In $Ar + KCl$, on the right panels, less cells are thermally excited, but due to the higher collision energy larger temperatures are reached.

As indicated in equations (2.9) and (2.20), the amount of radiated thermal dileptons per time step is determined by an interplay of the fireball volume and the strong exponential temperature dependence in the Bose distribution of the emissivity. In the beginning, shortly after the initial impact of the colliding nuclei, only a few cells in the center of the collision zone reach thermal equilibrium and radiate dileptons. Then more and more cells acquire a high temperature and contribute to the dilepton emission. When the fireball starts to expand, the matter in an even larger amount of cells thermalizes, but the fireball cools down at the same time. For a certain amount of time the increase in volume can compensate for the dropping of temperature. This keeps the dilepton emission rate at a moderate level until the penalty induced by the exponential temperature dependence of the Bose factor finally shuts down the dilepton emission.

This interplay between temperature and volume is shown in Figure 4.2. On the left panel the time evolution of the thermal volume (blue squares) is shown. A cell contributes to this volume if at least one baryon with $n_{\text{coll}} \geq 3$ per 10 events is inside this cell and a temperature as been assigned to the cell. The corresponding average temperature inside this volume is plotted with green triangles. On the right hand side the thermal Bose factor (red triangles) is calculated with this temperature for a dilepton energy of $q_0 = 600$ MeV. At last, the Bose factor is multiplied by the thermal volume (yellow squares). This quantity gives a rough estimate of the dilepton rate which is on top modulated by the in-medium spectral function.

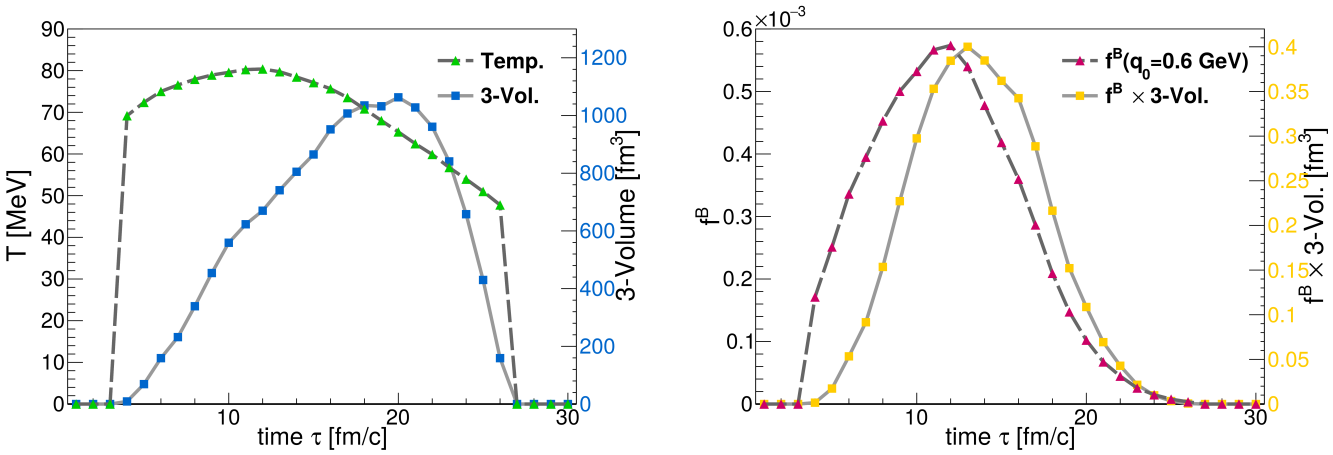

Figure 4.2: Left: Time evolution of the thermalized volume of the fireball (blue squares, right vertical scale) and the average temperature inside this volume (green triangles) for $Au + Au$ at 1.23 AGeV. Right: Time evolution of the thermal Bose factor (red triangles) and the product $f^B \times$ thermal 3-volume for $Au + Au$ at 1.23 AGeV. (yellow squares, right vertical scale).

Merging the realistic dilepton rates, provided by the Rapp-Wambach spectral function, with the accurate description of the space-time evolution, through the coarse-graining of hadronic transport, allows for the calculation of the amount of dileptons radiated in a given mass region per unit of time. The evolution of this integrated yield in the mass range $M = 0.3 - 0.7\,\text{GeV/c}^2$ is illustrated on the left panel of Figure 4.3.

The evolution of the integrated yield from all cells (blue squares) has a remarkably similar shape and peak position as expected from the interplay between temperature and fireball volume. The inner cube of cells (red circles) gives the main contribution to the amount of radiated dilepton in the first few time steps until, at about 8 fm/c after the nuclei started to touch, the outer shell catches up and starts to emit about 2/3 of the radiated yield. Note that the volume inside the inner cube constitutes only roughly 10% of the total fireball volume.

The main portion of dileptons (85%) emanates from a 13 fm/c long time interval in the middle of the fireball evolution. The first 7 fm/c and the time steps later than 21 fm/c after the first collisions have only a small impact on the total amount of radiated lepton pairs. This time interval which produces most of the radiation is much shorter than the time in which the system exists at a raised net-baryon density ($\sim 20 - 25$ fm/c).

The cumulative radiated dilepton yield can be correlated with the build-up of the collective transverse flow in the medium. Figure 4.3 demonstrates that both, the cumulative yield and the average flow velocity, exhibit basically the same time evolution. Collectivity is a manifestation of the pressure in the system as a direct consequence of the interactions happening inside the medium. The same interactions excite resonances and lead therefore to dilepton

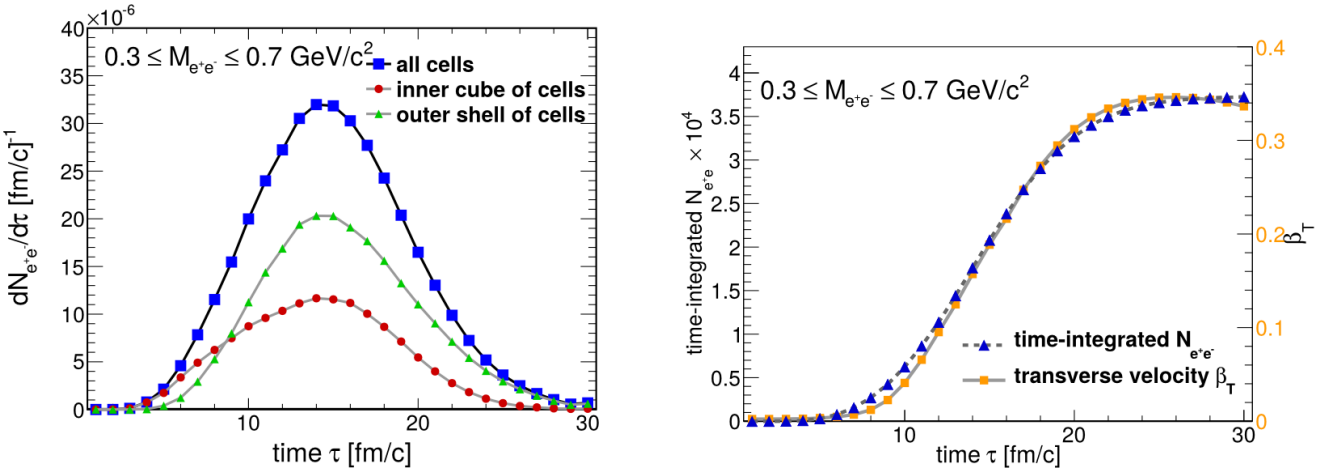

Figure 4.3: Left: Evolution of the radiated dilepton yield per unit time integrated in the mass range $M = 0.3 - 0.7\,\mathrm{GeV/c^2}$. The contribution of all cells is shown by the blue squares, while the red circles display the share from the inner cube of 7^3 cells and the green triangles depict the part arising from the outer shell of cells (all cells minus inner cube). Right: Evolution of the cumulative dilepton yield radiated in the mass range $M = 0.3 - 0.7\,\mathrm{GeV/c^2}$ (blue triangles) and the collective transverse velocity β_T averaged over all cells (orange squares, right vertical scale).

emission. It is interesting to see that these two quantities which are determined rather independent from reach other agree so well. This corroborates the picture that the 13 fm/c long interval is really the fireball lifetime. As the slow down of the build-up of collective velocity indicates that the collisions inside the medium have decreased and finally stopped to happen, it clearly means the end to what one would call an interacting fireball.

Of no less interest are the invariant mass excess spectra calculated for central $Au + Au$ and $Ar + KCl$ collisions. These are shown in the left panel of Figure 4.4, decomposed into the contribution of in-medium ρ meson decays and hadronic continuum radiation.

The strong medium effects on the ρ meson induced by the hot and dense matter created in both collision systems result in a remarkably structureless excess spectrum with only a slight bump remaining in the region of the vacuum ρ pole mass. The medium effects appear even stronger than in the $In + In$ collision system at 158 AGeV measured by the NA60 collaboration [36]. This is to some extend due to the larger system size in case of $Au + Au$, but mainly driven by the high baryon densities created at lower collision energies since the invariant mass spectrum in the smaller $Ar + KCl$ system exhibits also an almost exponential shape. A large portion of the cells which are hot and therefore have a high dilepton emission rate feature also a high effective baryon density above $2\varrho_0$. The gray lines in the invariant mass spectra indicate the contribution of cells with a low density $\varrho_{\mathrm{eff}} < 0.5\rho_0$ and with a temperature below the value assign to the chemical freeze-out point ($T_{\mathrm{ch}} = 47 \pm 5$ MeV for $Au + Au$ at 1.23 AGeV [44] and $T_{\mathrm{ch}} = 76 \pm 5$ MeV for $Ar + KCl$ at 1.76 AGeV [43]). In case of $Ar + KCl$ the dileptons from these cells show a peak at the ρ meson pole mass, while it is melted away when all cells are included. Note that these low density and temperature cells contribute only roughly 10% to the total in-medium ρ meson emission, but they represent the vast majority of cells as illustrated in the lower row of Figure 4.1. For $Au + Au$ the ρ meson peak is also melted in the contributions from the low density and low temperature cells. This might be an effect of the Bose factor which penalizes higher invariant masses stronger at such low temperatures. If the cells are, however, restricted to be below a temperature of $T = 60$ MeV also in $Au + Au$ a ρ meson peak becomes visible.

If the EM spectral function does not depend on temperature, the only temperature dependence of the dilepton emission rate is induced by the Bose factor (see equation 2.9). This is approximately the case in the IMR ($M = 1.5 - 2.5\,\mathrm{GeV/c^2}$), rendering this mass range an ideal thermometer of the fireball, unaffected by collective flow induced blue-shifts [50]. In this region, the invariant mass spectrum is approximately proportional to (for a derivation see appendix 6.11):

$$\frac{dN_{ll}}{dM} \propto (MT)^{3/2} \exp\left(-\frac{M}{T}\right). \tag{4.1}$$

A fit of this function to the excess spectrum in the $Au + Au$ system yields $T_{\mathrm{slope}} = 88 \pm 5$ MeV which is much larger than T_{ch} and matches the highest temperatures reached in the cells at the center of the collision zone. This implies

that the dilepton emission in this range is dominated by the hottest phase of the fireball evolution which coincides at low energies not with the earliest stage.

The right panel of Figure 4.4 depicts the 2-dimensional $\frac{dN_{ee}}{dM\,dp_T}$ spectrum for $Au+Au$ at 1.23 AGeV which can directly be included into Pluto to sample the masses and momenta of electron pairs for the in-medium ρ meson contribution.

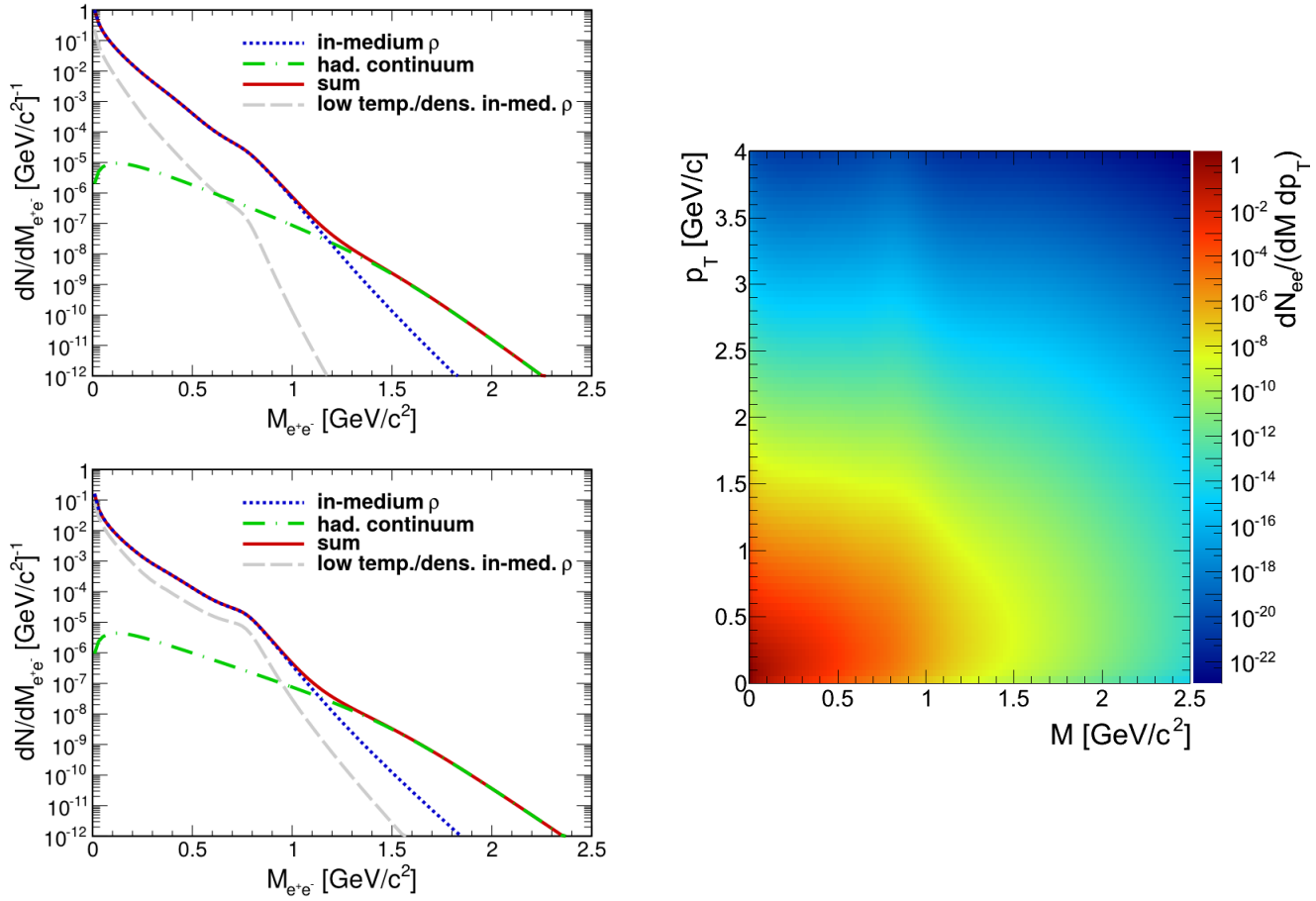

Figure 4.4: Invariant mass spectrum of thermal dileptons emanating from in-medium ρ (blue dotted line) and hadronic continuum radiation (green dashed-dotted line) as well as their sum (red solid line) for $Au+Au$ at 1.23 AGeV in the upper left and $Ar+KCl$ at 1.76 AGeV in the lower left plot. The gray dashed line illustrates the contribution to the in-medium ρ radiation restricted to cells with low density $\varrho_{\text{eff}} < 0.5\rho_0$ and temperatures below the freeze-out value $T < T_{\text{ch}} = 47$ MeV (76 MeV for $Ar+KCl$). The input histogram for Pluto depicting $\frac{dN_{ee}}{dM\,dp_T}$ from thermal radiation in the $Au+Au$ collision system is plotted on the right panel.

5 Summary & Outlook

For the description of the thermal contributions to the dilepton spectrum, accurate dilepton emission rates and a realistic description of the fireball space-time evolution are needed, as dileptons are radiated over the whole course of a heavy-ion collision. While the hydrodynamic models used at high energies allow for a direct application of the thermal in-medium rates, the implementation of medium modifications into the transport models utilized in the low energy regime is difficult.

The coarse-graining approach [109] used in this work combines the advantages of microscopic transport models with the ability to use in-medium dilepton rates calculated via thermal many-body approaches. By averaging over many simulated transport events and dividing the fireball evolution into small 4-dimensional space-time cells, one can identify those cells which are equilibrated and assign local temperatures and densities to them. This in turn permits the use of thermal rates for the in-medium ρ meson and (at higher energies) the QGP radiation.

The densities of nucleons, pions and Δ resonances can be determined by boosting the matter inside a given cell into the local rest frame. The temperatures are obtained by exponential fits to properly normalized transverse mass spectra. A third important quantity figuring into the dilepton emission, the effective pion chemical potential, is extracted in Boltzmann approximation. It accounts for the fact that in the later stages of a collision the system may be overpopulated by pions compared to the expectation of thermal and chemical equilibrium.

With these input parameters the contribution of every thermalized space-time cell to the total dilepton emission can be calculated. The final spectrum is obtained by summing over all cells. It can be implemented as a plug-in into the event generator Pluto and used for the sampling of dileptons. Afterwards the simulated dileptons can be filtered through the detector acceptance and kinematic cut can by applied as in real data.

The developed framework allows the users to pick a collision system of their choice (ion species, collision energy, centrality class) and run the coarse-graining procedure to obtain the input spectra for Pluto. It will be interesting to simulate the thermal radiation for the $Ag+Ag$ collision system at 1.6 AGeV planned to be measured by HADES and for $Au+Au$ collisions in the SIS100 energy range for CBM. In general one can also try to extend the framework to even higher energies with regard to the RHIC beam energy scan. Up to now only central collisions were simulated and the results were later on scaled to the centrality classes used by the experiments. In case of $Ar+KCl$, it has been checked that the simulated data is compatible with the published measurements of the HADES collaboration [75]. As the simulation is done for central events and for the full 4π phase space, the outcome has to be scaled properly to the 40% most central collisions measured by HADES, assuming that the excess yield scales with $A_{\mathrm{part}}^{1.4}$. Additionally the acceptance of the detector has to be taken into account. The implementation of the corresponding $\frac{dN_{ee}}{dM\,dp_T}$ spectrum into Pluto makes the filtering through the HADES acceptance possible and will allow for a more detailed comparison between simulation and experiment.

The setup, however, is easily adapted to also cope with a direct calculation of the dilepton spectra for different centralities if an appropriate impact parameter (range) is chosen for the transport simulation. Such a direct determination might reduce the error bands, allowing for a better comparison to experimental data. Another possible extensions to the framework will be the implementation of chiral mixing [119] which can "fill" the small dip in the invariant mass spectrum in the transition region between in-medium ρ meson and continuum radiation. The modular structure of the developed framework also allows to change either the model used for the space-time evolution or the emission rates used in the dilepton calculations. A further check which should be done in the future is the test for model independence by switching UrQMD against another transport model, like GiBUU or HSD. It might also be interesting to see, what impact on the current results will be induces by models with dileptons radiated at the critical point of a first order phase transition.

Altogether the framework developed in this work brought new insights with regard to the lifetime of the fireball at lower collision energies, which is to a large part determined by an interplay between temperature and volume of the fireball. In the early collision stages, the thermalized volume is small leading to a negligible emission of dileptons even though the temperatures in these cells are quite high. Only after about 8 fm/c, when the effective baryon density reaches already 70% of its maximum value, the dilepton radiation picks up rather quickly. At this point in time, one finds that part of the matter is equilibrated, as indicated by the large Gaussian component in the longitudinal momentum distribution of nucleons which have undergone at least 3 interactions. The radiation phase lasts for about 13 fm/c which is quite a bit smaller than one might have expected based on the evolution of

the effective baryon density. The decrease in temperature during that time can be compensated by the growth of the fireball volume. Afterwards the dilepton rate drops rapidly, suggesting that the penalty induced by the Bose factor becomes to big.

This picture, drawn by the dilepton emission rate, is supported by the development of collective flow which shows a very similar evolution compared to the cumulative yield of lepton pairs. The radiation window nicely coincides with the time duration over which the transverse collectivity builds up.

In addition the slope extracted from the IMR yields a blue-shift free temperature of $T_s = 88 \pm 5\,\mathrm{MeV}$ which corresponds to the highest temperatures reached in the space-time cells and demonstrates the capability of this mass region to serve as a fireball thermometer.

6 Appendix

6.1 Differential Dilepton Spectra

To calculate various differential spectra from the dilepton production rate

$$\frac{dR}{d^4q} = \frac{dR}{dq_0\, dq_X\, dq_Y\, dq_Z} = \frac{dN_{ll}}{d^4x d^4q} \tag{6.1}$$

certain variable transformations are needed which involve Jacobians. These are derived below.

The energy q_0 of a particle with mass M, transverse momentum q_T and momentum in z-direction q_Z is given by $q_0 = \left(q_T^2 + q_Z^2 + M^2\right)^{1/2}$. Thus,

$$\frac{dq_0}{dM} = \frac{1}{2}\,\frac{1}{q_0}\,2M \qquad \Rightarrow \qquad \boxed{q_0 dq_0 = M dM}. \tag{6.2}$$

The rapidity y of that particle is defined as

$$y = \frac{1}{2}\ln\frac{q_0 + q_Z}{q_0 - q_Z}. \tag{6.3}$$

The rapidity depends on q_Z and q_0 which in turn also depends on q_Z so that

$$\frac{dy}{dq_Z} = \frac{\partial y}{\partial q_Z} + \frac{\partial y}{\partial q_0}\,\frac{\partial q_0}{\partial q_Z}. \tag{6.4}$$

The first part gives

$$\frac{\partial y}{\partial p_Z} = \frac{1}{2}\,\frac{q_0 - q_Z}{q_0 + q_Z}\,\frac{d}{dq_Z}\left(\frac{q_0 + q_Z}{q_0 - q_Z}\right) = \frac{1}{2}\,\frac{q_0 - q_Z}{q_0 + q_Z}\,\frac{2q_0}{(q_0 - q_Z)^2} = \frac{q_0}{q_0^2 - q_Z^2} \tag{6.5}$$

where the second equality is due to

$$\frac{d}{dq_Z}\left(\frac{q_0 + q_Z}{q_0 - q_Z}\right) = \frac{(q_0 - q_Z) - (-1)(q_0 + q_Z)}{(q_0 - q_Z)^2} = \frac{2q_0}{(q_0 - q_Z)^2}. \tag{6.6}$$

In an analog way it follows that

$$\frac{\partial y}{\partial q_0} = \frac{1}{2}\,\frac{q_0 - q_Z}{q_0 + q_Z}\,\frac{d}{dq_0}\left(\frac{q_0 + q_Z}{q_0 - q_Z}\right) = \frac{1}{2}\,\frac{q_0 - q_Z}{q_0 + q_Z}\,\frac{-2q_Z}{(q_0 - q_Z)^2} = \frac{-q_Z}{q_0^2 - q_Z^2}. \tag{6.7}$$

Together with

$$\frac{\partial q_0}{\partial q_Z} = \frac{1}{2}\left(q_T^2 + q_Z^2 + M^2\right)^{-1/2}\,2q_Z = \frac{q_Z}{q_0} \tag{6.8}$$

one arrives at

$$\frac{dy}{dq_Z} = \frac{q_0}{q_0^2 - q_Z^2} + \frac{-q_Z}{q_0^2 - q_Z^2}\,\frac{q_Z}{q_0} = \frac{q_0 - \frac{q_Z^2}{q_0}}{q_0^2 - q_Z^2} = \frac{q_0^2 - q_Z^2}{q_0^2 - q_Z^2}\,\frac{1}{q_0} = \frac{1}{q_0} \Rightarrow \boxed{dq_Z = q_0 dy}. \tag{6.9}$$

The third Jacobian is the well known transformations from Cartesian to polar coordinates for isotropic quantities

$$\boxed{dq_X\, dq_Y = q_T\, dq_T\, d\varphi = 2\pi\, q_T\, dq_T}. \tag{6.10}$$

With these Jacobians the derivation of different spectra is straightforward:

$$\frac{dR}{dq_0} = \frac{q_0}{M}\frac{dR}{dM} \quad \Rightarrow \quad \frac{dR}{dM} = \int d^3q \frac{M}{q_0} \quad \frac{dN_{ll}}{d^4x d^4q}$$

$$\frac{dR}{dq_X\, dq_Y} = \frac{dR}{2\pi\, q_T\, dq_T} \quad \Rightarrow \quad \frac{dR}{dq_T} = \int dq_0\, dq_Z\, 2\pi q_T \quad \frac{dN_{ll}}{d^4x d^4q}$$

$$\frac{dR}{dq_0\, dq_X\, dq_Y} = \frac{dR}{dM\, dq_T}\frac{q_0}{2\pi q_T M} \quad \Rightarrow \quad \frac{dR}{dM\, dq_T} = \int dq_Z \frac{2\pi q_T M}{q_0} \quad \frac{dN_{ll}}{d^4x d^4q}$$

$$\frac{dR}{dq_0\, dq_X\, dq_Y\, dq_Z} = \frac{dR}{dM\, dq_T\, dy}\frac{1}{2\pi q_T M} \quad \Rightarrow \quad \frac{dR}{dM\, dq_T\, dy} = 2\pi q_T M \quad \frac{dN_{ll}}{d^4x d^4q}$$

The mass M and the 3-momentum q enter into the in-medium spectral function. For a given particle with mass M, rapidity y and transverse momentum q_T, what is the corresponding value of the 3-momentum q?

As $q^2 = q_T^2 + q_Z^2$, it is needed to calculate the momentum in z-direction in terms of M, q_T and y. Writing q_Z and q as $q_Z = q\cos(\theta)$ and $q = \beta q_0$ the relation for the rapidity becomes

$$y = \frac{1}{2}\ln\frac{q_0 + q_Z}{q_0 - q_Z} = \frac{1}{2}\ln\frac{1+\beta\cos(\theta)}{1-\beta\cos(\theta)}. \tag{6.11}$$

Solving this equation for $\beta\cos(\theta)$ gives

$$\beta\cos(\theta) = \frac{e^{2y}-1}{e^{2y}+1} = \frac{e^{y}-e^{-y}}{e^{y}+e^{-y}} = \frac{\sinh(y)}{\cosh(y)} = \tanh(y). \tag{6.12}$$

This then leads to

$$q_Z = q\cos(\theta)\cdot\frac{\beta}{\beta} = \frac{q}{\beta}\tanh(y) = q_0\tanh(y). \tag{6.13}$$

For the transverse mass $M_T = \left(q_T^2 + M^2\right)^{1/2}$, it follows that

$$M_T^2 = q_T^2 + M^2 = q_0^2 - q_Z^2 = q_0^2\left(1-\tanh^2(y)\right) = \frac{q_0^2}{\cosh^2(y)}. \tag{6.14}$$

This finally gives

$$\boxed{q_0 = M_T\cosh(y)} \tag{6.15}$$

and

$$\boxed{q_Z = q_0\tanh(y) = M_T\sinh(y) = \left(q_T^2 + M^2\right)^{1/2}\sinh(y)}. \tag{6.16}$$

6.2 Exponential Fit to Transverse Mass Spectra

The starting point is the Boltzmann approximation

$$\frac{d^3N}{d\vec{p}} = \frac{d^3N}{dp_z\, p_t\, dp_t\, d\theta} \propto \exp(-E/T) \tag{6.17}$$

with the energy $E = \sqrt{\vec{p}^2 + m^2}$ and the temperature T. Integration over the azimuthal angle θ and changing from momentum in beam direction p_z to rapidity y via $dp_z = E\, dy$ yields

$$\frac{d^2N}{dy\, dp_t} \propto 2\pi\, p_t\, E\, \exp(-E/T). \tag{6.18}$$

A transformation from transverse momentum p_t to transverse mass $m_t = \sqrt{p_t^2 + m^2}$ via $p_t\, dp_t = m_t\, dm_t$ and using the relation $E = m_t \cosh(y)$ results in

$$\frac{d^2N}{dy\, dm_t} \propto 2\pi\, m_t\, E\, \exp(-E/T) = 2\pi\, m_t^2\, \cosh(y)\, \exp(-m_t \cosh(y)/T). \tag{6.19}$$

At midrapidity, $y = 0$, the $\cosh(y)$ term equals 1 and the formula reduces to

$$\boxed{\frac{1}{m_t^2}\frac{dN}{dm_t}\bigg|_{y=0} \propto \exp(-m_t/T)}. \tag{6.20}$$

If one is interested in the full rapidity range the integration over all rapidities of equation (6.19) has to be carried out.

$$\begin{aligned}
\frac{dN}{dm_t} &\propto \int dy\, 2\pi\, m_t^2\, \cosh(y)\, \exp(-m_t \cosh(y)/T) \\
&= 2\pi\, m_t^2 \left(\int_0^\infty dy\, \cosh(y)\, \exp(-m_t \cosh(y)/T) + \int_{-\infty}^0 dy \ldots \right) \\
&= 2\pi\, m_t^2 \cdot 2 \int_0^\infty dy\, \cosh(y)\, \exp(-m_t \cosh(y)/T) \\
&= 2\pi\, m_t^2 \cdot 2\, K_1\left(\frac{m_t}{T}\right)
\end{aligned} \tag{6.21}$$

The third line of equation (6.21) utilizes the symmetry properties of $\cosh(y)$ and the forth line uses the definition of the modified Bessel function of the second kind K_n. These functions exhibit the following asymptotic behavior for large values of the argument.

$$K_n(z) \quad \overset{\sim}{\underset{z \to \infty}{\longrightarrow}} \quad \sqrt{\frac{\pi}{2z}} \exp(-z) \tag{6.22}$$

Thus for $m_t \gg T$ the application of this approximation leads to

$$\frac{dN}{dm_t} \propto 2\pi\, m_t^2 \cdot 2 \left(\frac{T}{m_t}\right)^{1/2} \exp(-m_t/T). \tag{6.23}$$

Absorbing all prefactors into the normalization, one arrives at

$$\boxed{\frac{1}{m_t^{3/2}}\frac{dN}{dm_t} \propto \exp(-m_t/T)}. \tag{6.24}$$

6.3 Baryon Density Profile in $Au + Au$ at 1.23 AGeV

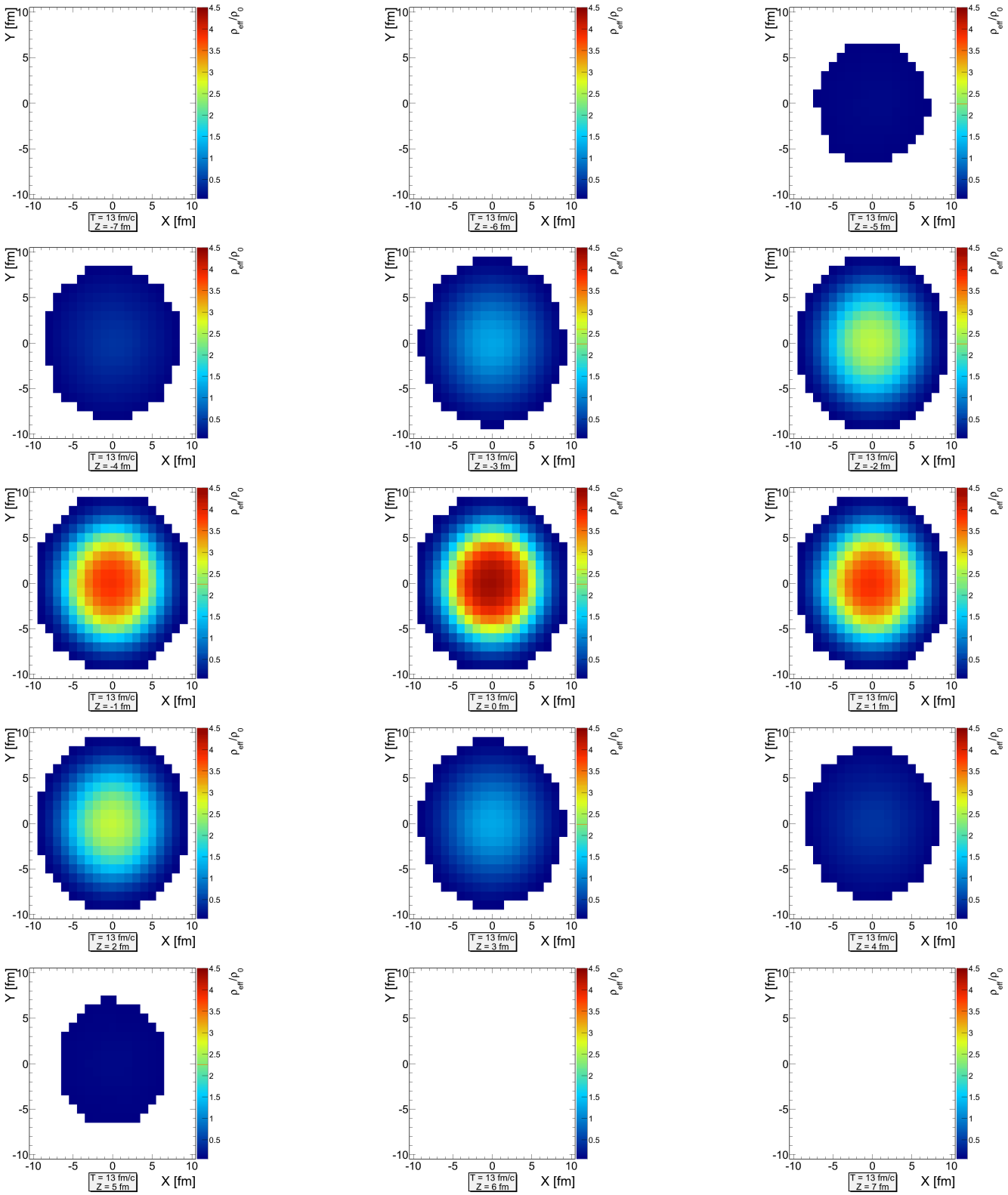

Figure 6.1: Effective baryon density ϱ_{eff} profile (slices in z-direction) in $Au + Au$ at 1.23 AGeV at time $\tau = 13$ fm/c. The range in x- and y-direction is from -10.5 fm to 10.5 fm. The color scheme indicates the density with $0.5\varrho_0$ in blue and $4.5\varrho_0$ in red. The z-slices shown from top left to bottom right are: $z = -7$ fm to $z = 7$ fm.

6.4 Pion Density Profile in $Au + Au$ at 1.23 AGeV

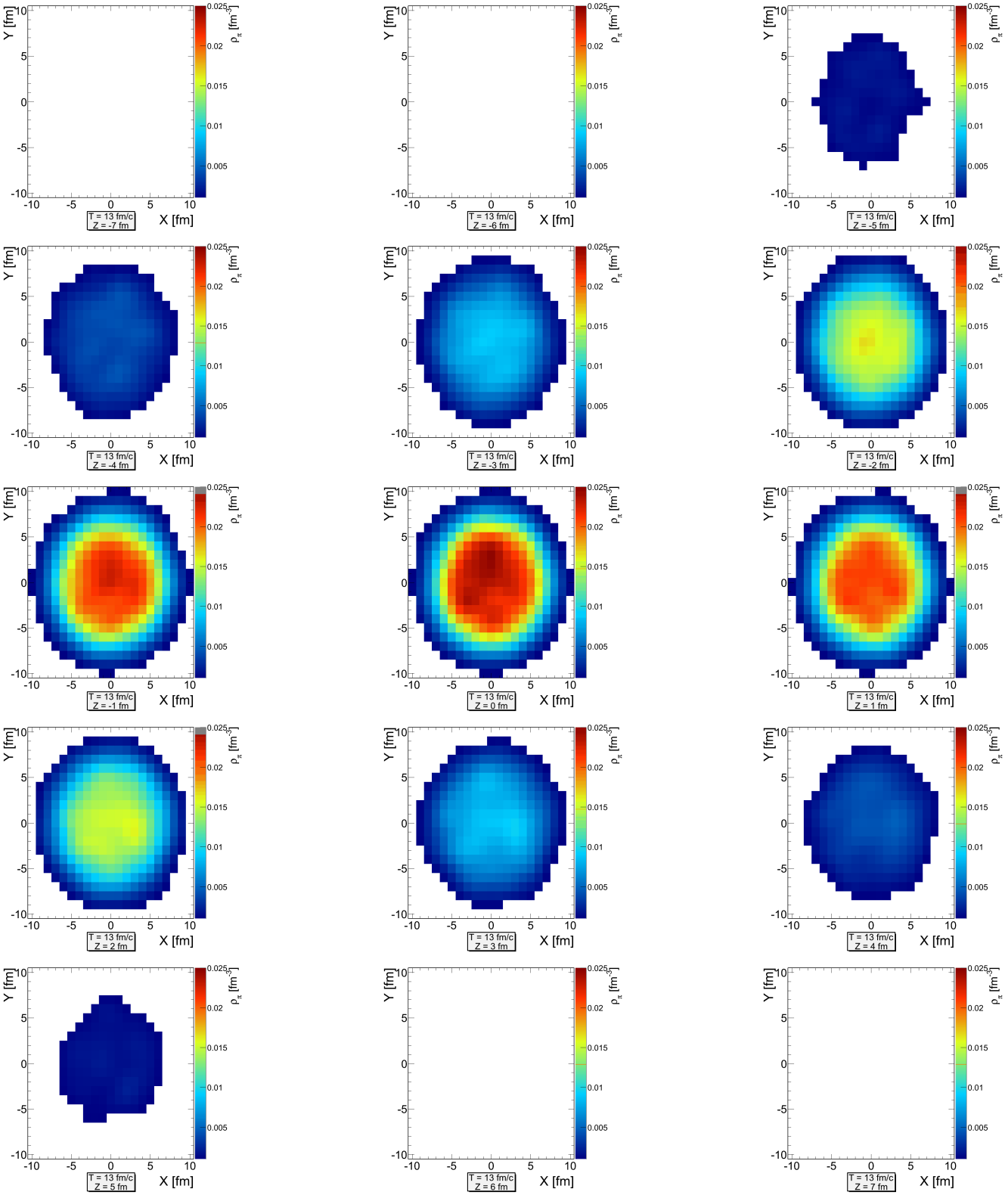

Figure 6.2: Pion density ϱ_π profile (slices in z-direction) in $Au + Au$ at 1.23 AGeV at time $\tau = 13$ fm/c. The range in x- and y-direction is from -10.5 fm to 10.5 fm. The color scheme indicates the density with 10^{-3} fm^{-3} in blue and $2.5 \cdot 10^{-2}$ fm^{-3} in red. The z-slices shown from top left to bottom right are: $z = -7$ fm to $z = 7$ fm.

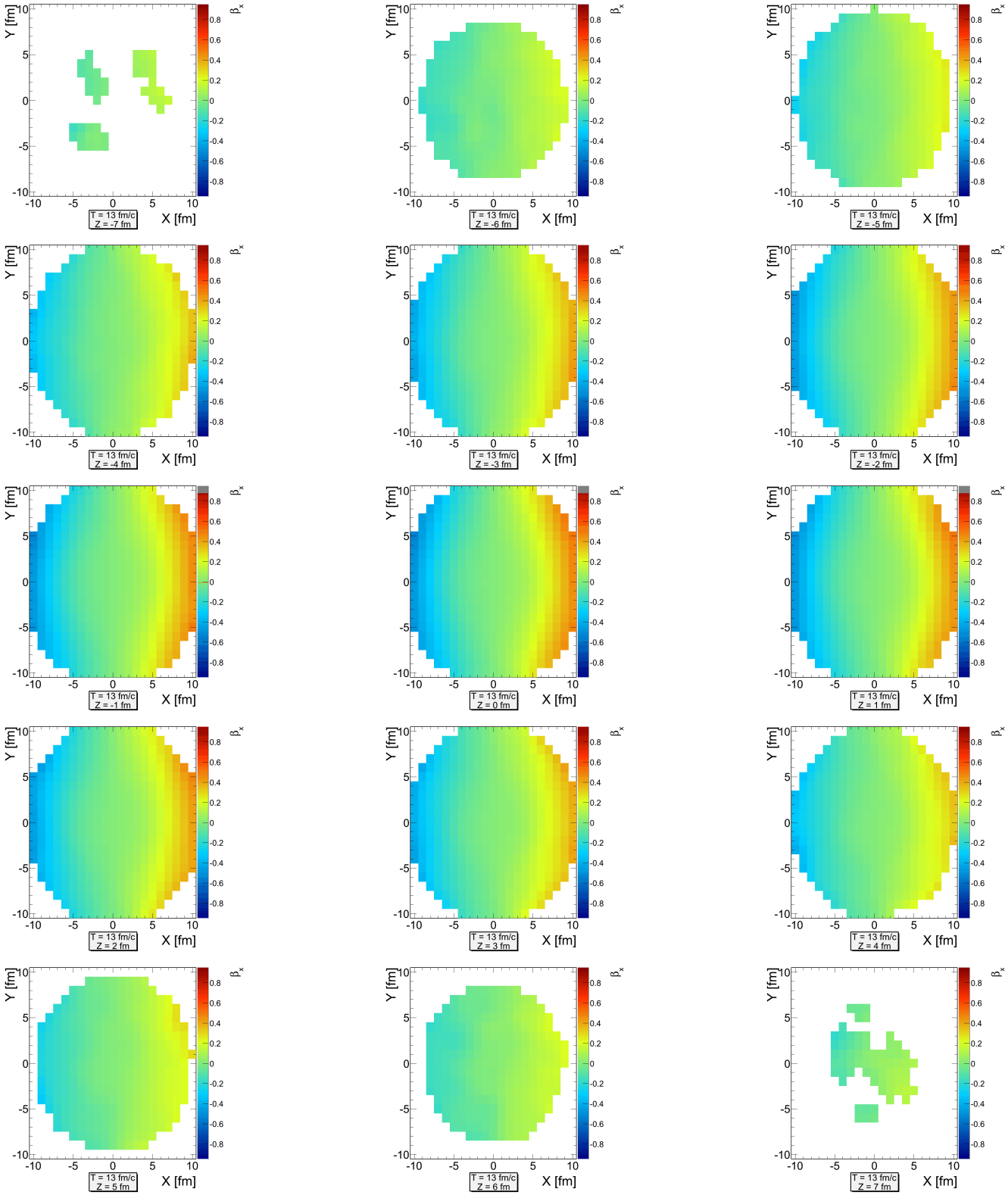

Figure 6.3: Collective velocity β_X profiles (slices in z-direction) in $Au+Au$ at 1.23 AGeV at time $\tau = 13$ fm/c. The range in x- and y-direction is from -10.5 fm to 10.5 fm. The color scheme indicates a velocity of $-0.85 \cdot c$ in blue and $0.85 \cdot c$ in red. The z-slices shown from top left to bottom right are: $z = -7$ fm to $z = 7$ fm.

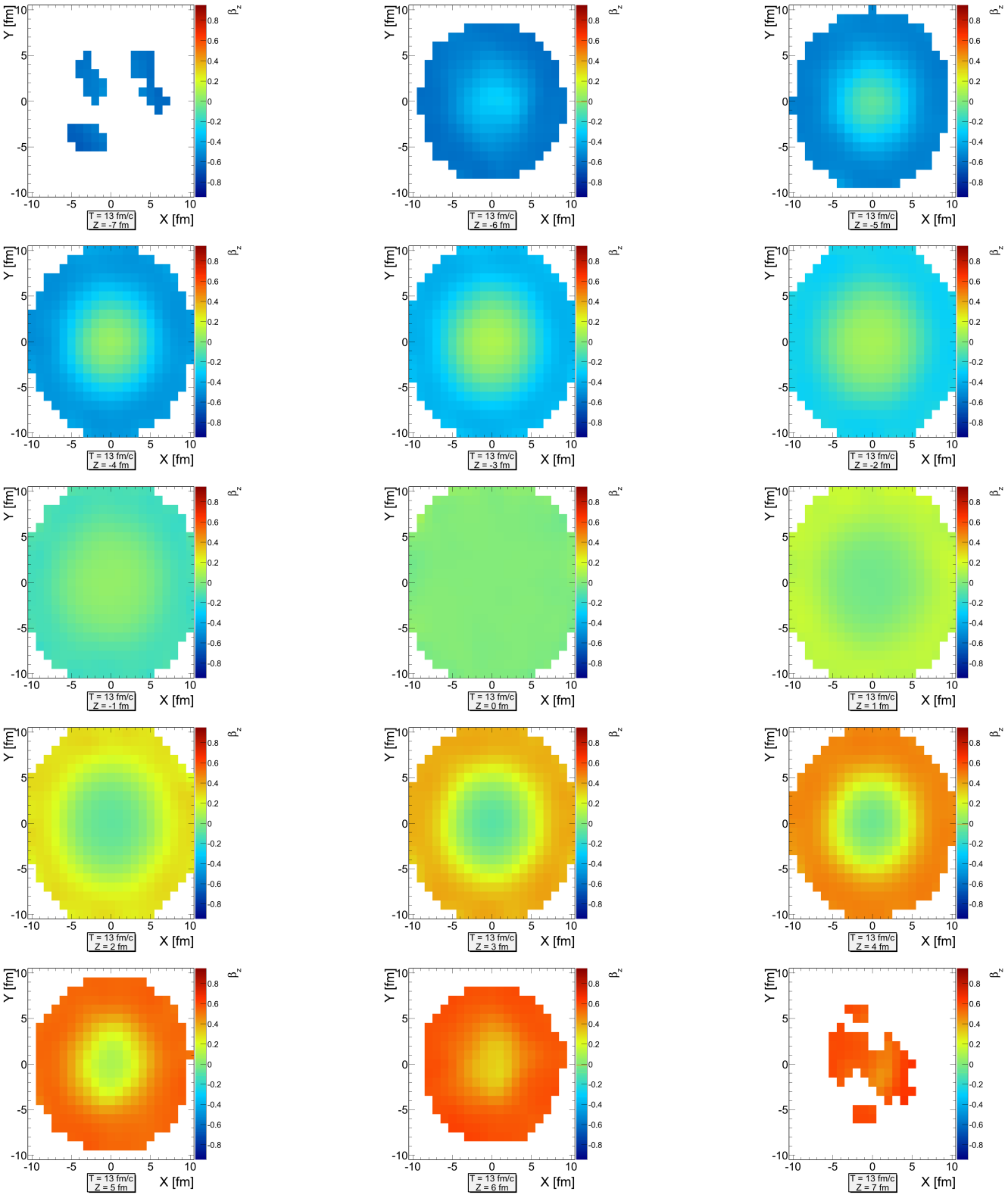

Figure 6.4: Collective velocity β_Z profiles (slices in z-direction) in $Au+Au$ at 1.23 AGeV at time $\tau = 13$ fm/c. The range in x- and y-direction is from -10.5 fm to 10.5 fm. The color scheme indicates a velocity of $-0.85 \cdot c$ in blue and $0.85 \cdot c$ in red. The z-slices shown from top left to bottom right are: $z = -7$ fm to $z = 7$ fm.

6.6 Temperature Profiles in $Au + Au$ at 1.23 AGeV

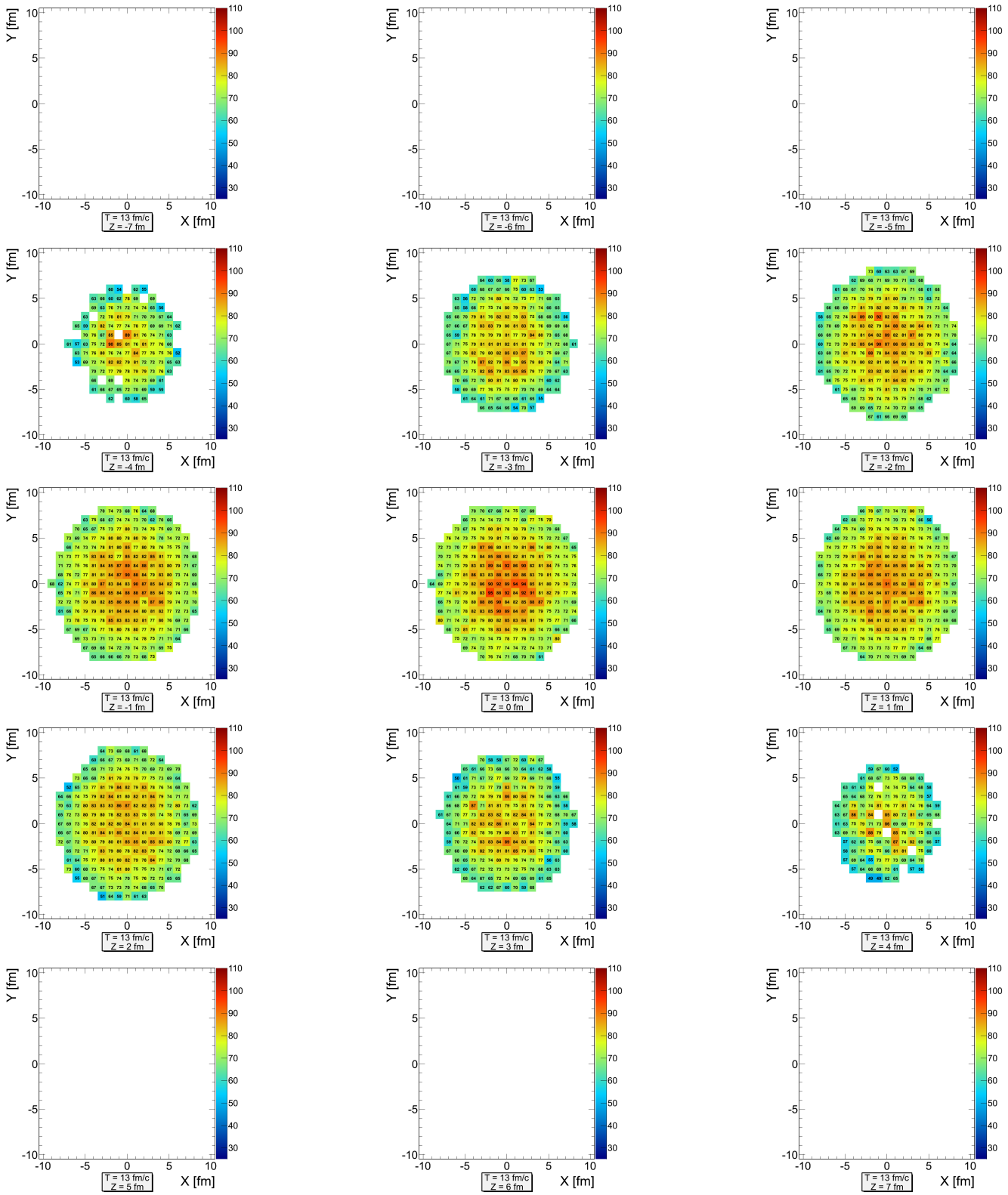

Figure 6.5: Profile plots (slices in z-direction) of temperature T extracted with pions in $Au + Au$ collisions at 1.23 AGeV at a fixed time step $\tau = 13$ fm/c. The range in x- and y-direction is from -10.5 fm to 10.5 fm. The color scheme indicates temperatures of 25 MeV in dark blue and 110 MeV in dark red. The z-slices shown from top left to bottom right are: $z = -7$ fm to $z = 7$ fm.

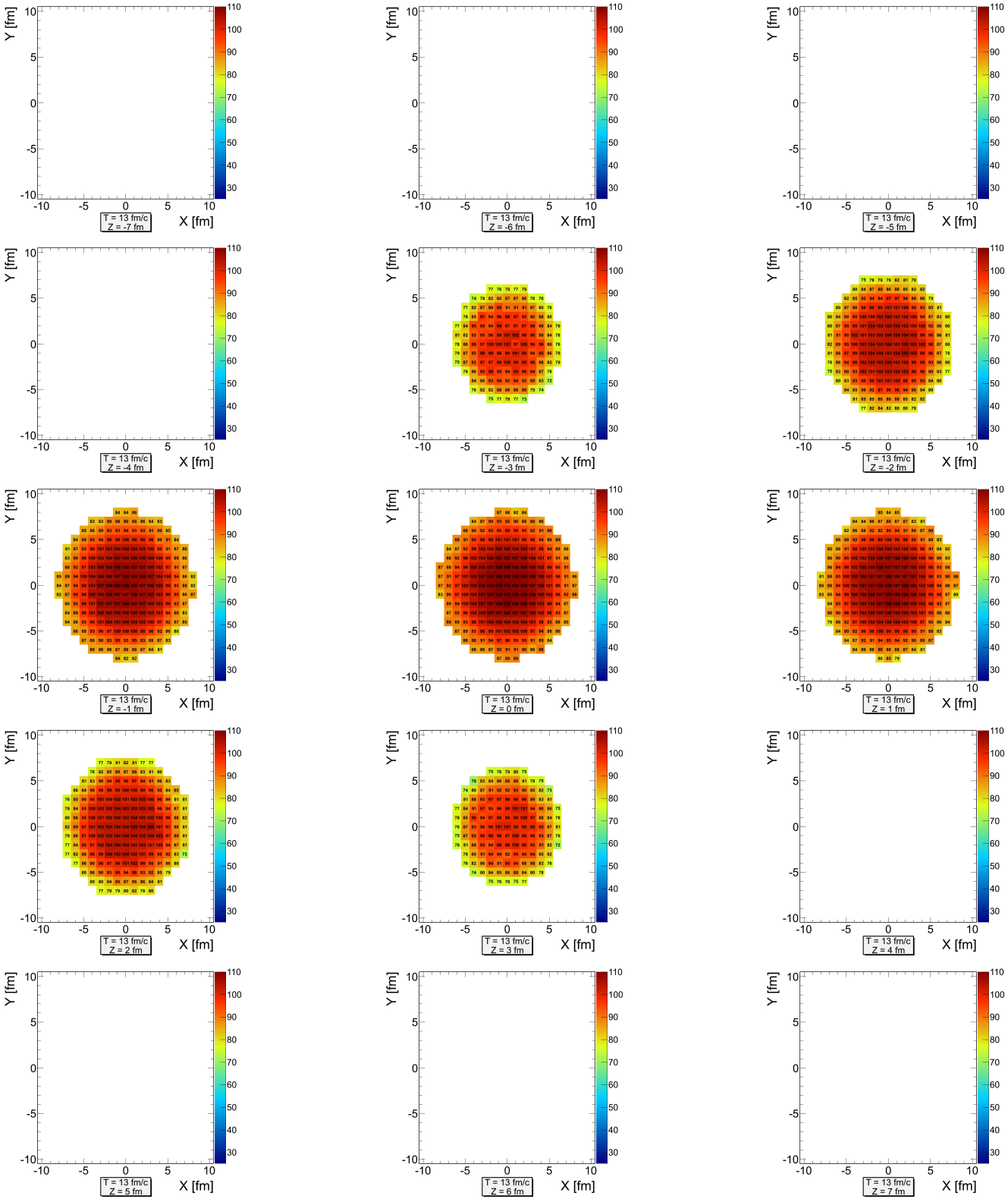

Figure 6.6: Profile plots (slices in z-direction) of temperature T extracted with thermal nucleons in $Au+Au$ collisions at 1.23 AGeV at a fixed time step $\tau = 13$ fm/c. The range in x- and y-direction is from -10.5 fm to 10.5 fm. The color scheme indicates temperatures of 25 MeV in dark blue and 110 MeV in dark red. The z-slices shown from top left to bottom right are: $z = -7$ fm to $z = 7$ fm.

6.7 Temperature Profiles in $Ar + KCl$ at 1.76 AGeV

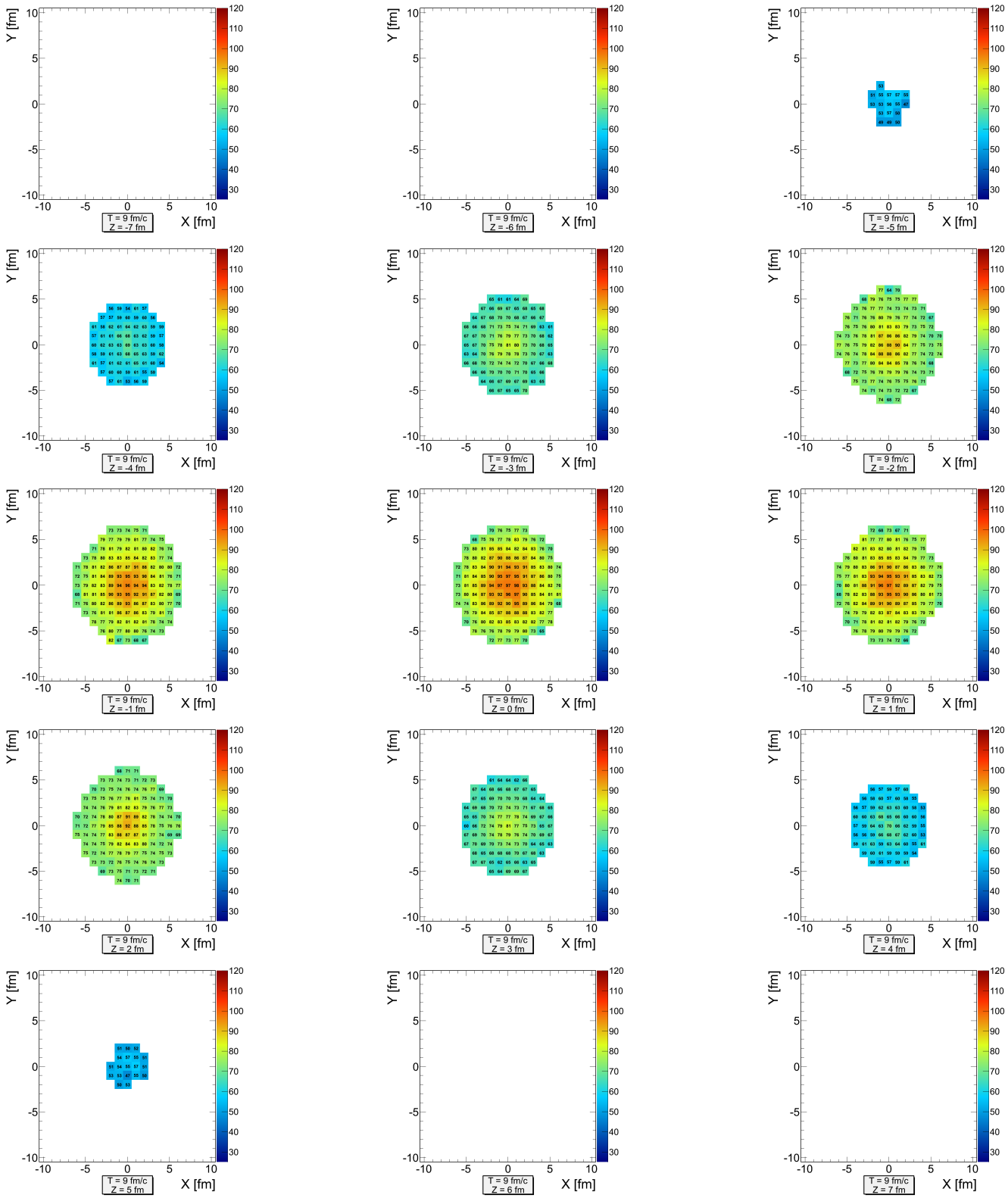

Figure 6.7: Profile plots (slices in z-direction) of temperature T extracted with pions in $Ar+KCl$ collisions at 1.76 AGeV at a fixed time step $\tau = 9$ fm/c. The range in x- and y-direction is from -10.5 fm to 10.5 fm. The color scheme indicates temperatures of 25 MeV in dark blue and 120 MeV in dark red. The z-slices shown from top left to bottom right are: $z = -7$ fm to $z = 7$ fm.

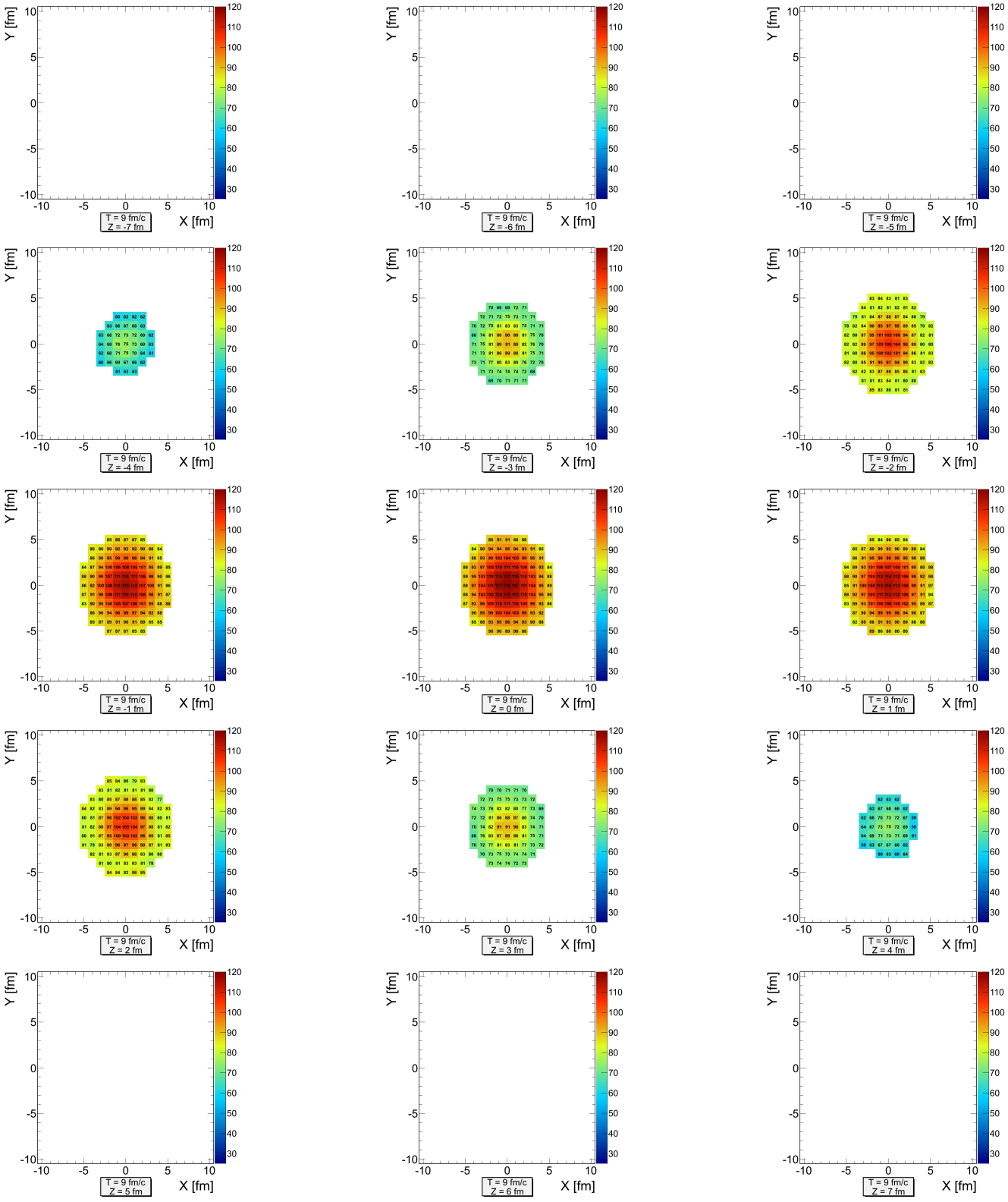

Figure 6.8: Profile plots (slices in z-direction) of temperature T extracted with thermal nucleons in $Ar + KCl$ collisions at 1.76 AGeV at a fixed time step $\tau = 9$ fm/c. The range in x- and y-direction is from -10.5 fm to 10.5 fm. The color scheme indicates temperatures of 25 MeV in dark blue and 120 MeV in dark red. The z-slices shown from top left to bottom right are: $z = -7$ fm to $z = 7$ fm.

6.8 Particle Densities in Thermal Equilibrium

In Boltzmann approximation, i.e., neglecting the quantum properties of fermions and bosons, the particle number density of a certain species in thermal equilibrium is given in natural units ($\hbar = c = k_B = 1$) by

$$n = \frac{g}{(2\pi)^3} \int_{\mathbb{R}^3} d^3\vec{p}\ \exp(-\beta\ (E-\mu)), \tag{6.25}$$

where g describes the degeneracy of spin and isospin ($g = 3$ for pions, $g = 4$ for nucleons and $g = 16$ for deltas), $\beta = 1/T$ is the inverse temperature, $E = \sqrt{\vec{p}^2 + m^2}$ is the energy and μ accounts for the chemical potential. The fugacity $z = \exp(\beta\mu)$ is independent of the momentum and can be moved in front of the integral. In thermal equilibrium the momentum distribution is spherically symmetric, so that the integration over the angles can be done easily.

$$n = \frac{4\pi\ g}{(2\pi)^3}\ z \int_0^\infty dp\ p^2\ \exp(-\beta\ \sqrt{p^2+m^2}) \tag{6.26}$$

To deal with this integral, a useful step is the variable change from p to y via $p = m\ \sinh(y)$. It follows that $dp = m\ \cosh(y)\, dy$ and $\sqrt{p^2+m^2} = m\ \sqrt{\sinh^2(y)+1} = m\ \cosh(y)$.

$$n = \frac{4\pi\ g\ m^3}{(2\pi)^3}\ z \int_0^\infty dy\ \cosh(y)\ \sinh^2(y)\ \exp(-\beta\ m\ \cosh(y)) \tag{6.27}$$

With the identity $\cosh(y)\ \sinh^2(y) = \frac{\cosh(3y)-\cosh(y)}{4}$ and the definition of the modified Bessel function $K_n(x) = \int_0^\infty dt\ \cosh(nt)\ \exp(-x\ \cosh(t))$ the particle number density can be written as

$$n = \frac{4\pi\ g\ m^3}{(2\pi)^3}\ z \left(\frac{K_3(\beta m) - K_1(\beta m)}{4}\right). \tag{6.28}$$

The two modified Bessel functions can be combined via the identity $K_{n+1}(x) - K_{n-1}(x) = \frac{2n}{x} K_n(x)$. It can be derived by performing the integral in the definition of $K_n(x)$ via integration by parts as

$$\begin{aligned} K_n(x) &= \underbrace{\left[\frac{1}{n}\ \sinh(nt)\ \exp(-x\cosh(t))\right]_0^\infty}_{=0} - \int_0^\infty dt\ \frac{1}{n}\ \sinh(nt)\,(-x)\ \sinh(t)\exp(-x\ \cosh(t)) \\ &= \frac{x}{n}\int_0^\infty dt \left\{\frac{\cosh((n+1)t) - \cosh((n-1)t)}{2}\right\} \exp(-x\ \cosh(t)) \\ &= \frac{x}{2n}\left\{K_{n+1}(x) - K_{n-1}(x)\right\}, \end{aligned} \tag{6.29}$$

where the second line follows as

$$\sinh(mx)\ \sinh(nx) = \frac{1}{2}\left[\cosh((m+n)x) - \cosh((m-n)x)\right]. \tag{6.30}$$

For the particle number density the use of this property of the modified Bessel functions results in

$$n = \frac{4\pi\ g\ m^3}{(2\pi)^3}\ z\ \frac{1}{\beta\ m} K_2(\beta m) \tag{6.31}$$

To change the units from $\left[\mathrm{MeV}^3\right]$ to $\left[\mathrm{fm}^{-3}\right]$ an appropriate power of the conversion factor $\hbar c = 197\,\mathrm{MeV\,fm}$ can be included.
If the particle number density n and the temperature T are known, the equation above can be used to determine the chemical potential

$$\boxed{\mu = T\ \ln\left(\frac{2\pi^2\ n\ (\hbar c)^3}{g\ T\ m^2\ K_2\left(\frac{m}{T}\right)}\right)}. \tag{6.32}$$

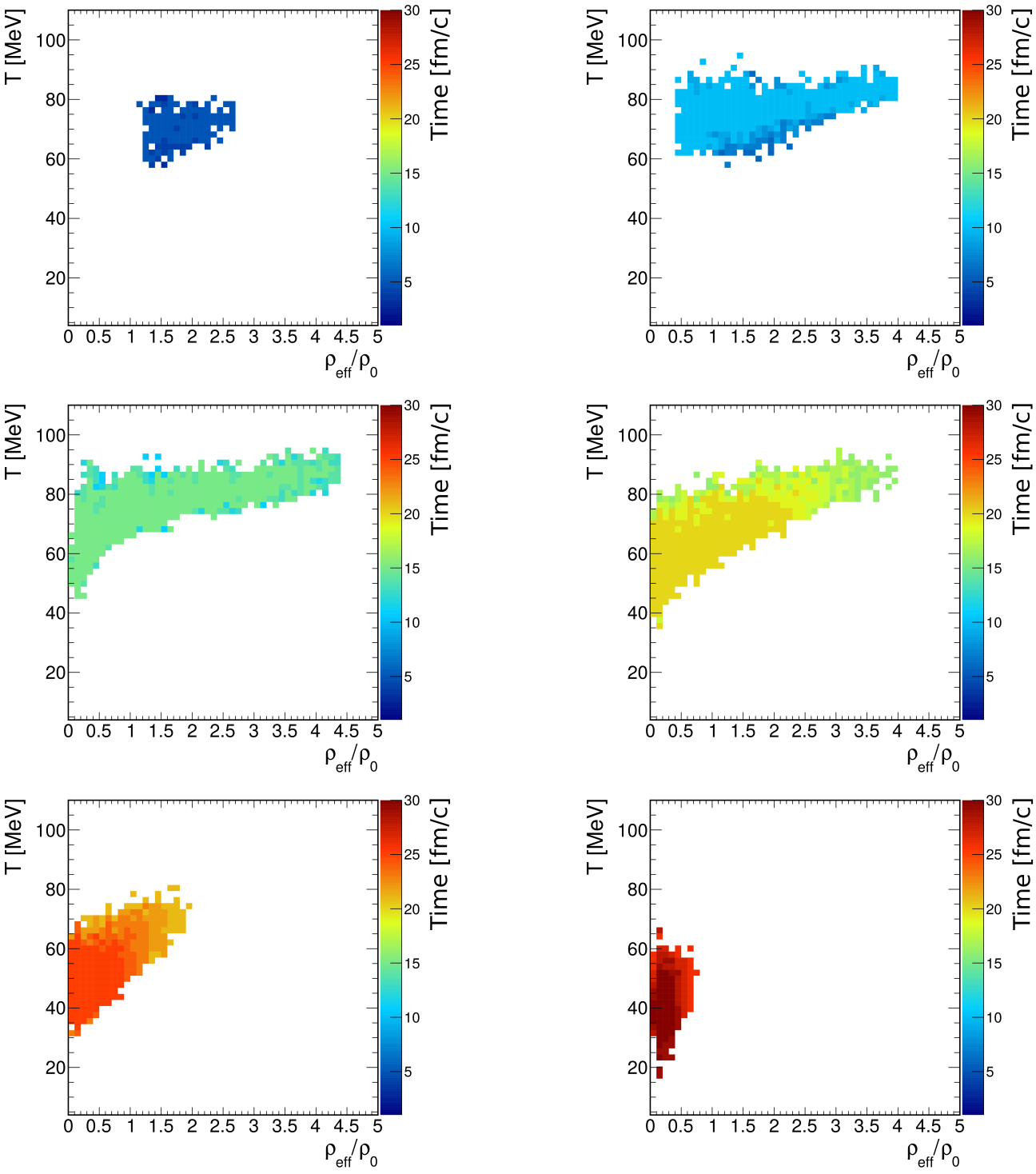

Figure 6.9: Trajectories of all cells in the $T - \varrho_{\text{eff}}$ plane for $Au + Au$ at 1.23 AGeV split into 5 fm/c long intervals for better visibility. The color scheme indicated the time step: $\tau = 1$ fm/c in blue, $\tau = 30$ fm in red.

6.10 Trajectories of the Space-Time Cells for $Ar + KCl$ at 1.76 AGeV in the $T - \varrho_{\text{eff}}$ plane

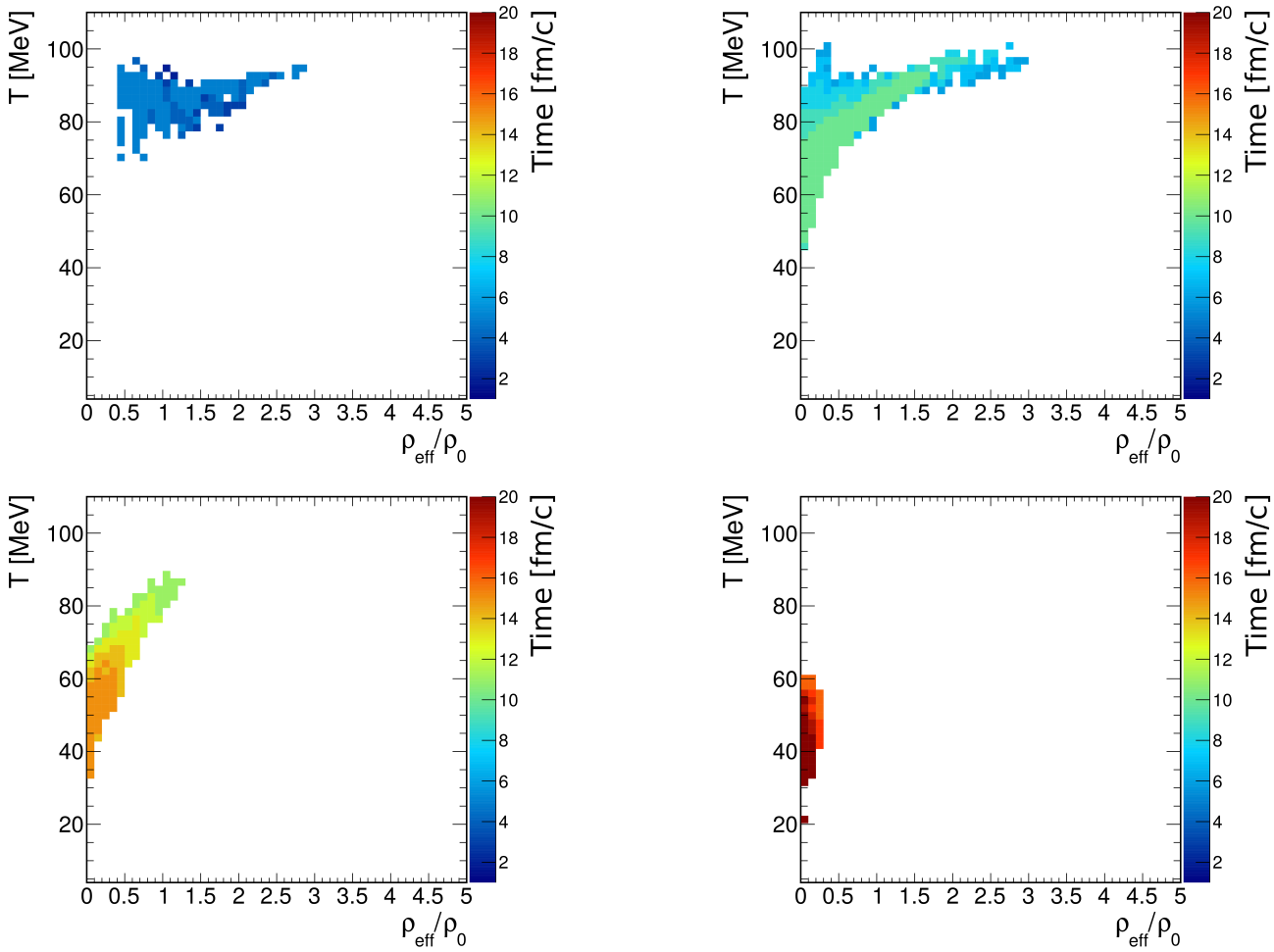

Figure 6.10: Trajectories of all cells in the $T - \varrho_{\text{eff}}$ plane for $Ar + KCl$ at 1.76 AGeV split into 5 fm/c long intervals for better visibility. The color scheme indicated the time step: $\tau = 1$ fm/c in blue, $\tau = 20$ fm in red.

6.11 Fit Function for the IMR Slope to Extract the Temperature

The starting point is the invariant mass spectrum

$$\frac{dN_{ll}}{dM} = \frac{M}{q_0}\int d^4x\, d^3q\, \frac{dN_{ll}}{d^4x\, d^4q} \tag{6.33}$$

$$\simeq \text{const.}\, V_{FB}\, \tau\, \frac{\text{Im}\Pi_{\text{EM}}(M;T)}{M}\int \frac{d^3q}{q_0}\exp(-q_0/T) \tag{6.34}$$

$$\simeq \text{const.}\, V_{FB}\, \tau\, \frac{\text{Im}\Pi_{\text{EM}}(M;T)}{M^2}\exp(-M/T)\,(MT)^{3/2}. \tag{6.35}$$

In the step from equation (6.33) to (6.34) the fireball 4-volume was integrated to $V_{FB}\,\tau$ and equation (2.9) was used as well as the fact that the in-medium EM spectral function depends only weakly on 3-momentum which is exact in the vacuum and approximately satisfied in the medium [102]. The step from equation (6.34) to (6.35) will be shown below. Assuming it is correct and using the fact that in the IMR the quantity $\frac{\text{Im}\Pi_{\text{EM}}(M;T)}{M^2}$ is almost a constant (see equation (2.12) and Figure 2.3), one arrives at

$$\boxed{\frac{dN_{ll}}{dM} \propto (MT)^{3/2}\exp\left(-\frac{M}{T}\right)}. \tag{6.36}$$

To proof the step from equation (6.34) to (6.35), one starts with

$$\int \frac{d^3q}{q_0}\exp(-q_0/T) = 4\pi\int_0^\infty dq\,\frac{q^2}{q_0}\exp(-q_0/T) \tag{6.37}$$

and substitutes $q = M\,\sinh(y)$, $q_0 = M\,\cosh(y)$ and $\frac{dq}{dy} = \cosh(y)$.
This means the above expression is equal to

$$4\pi\int dy\, M\,\cosh(y)\frac{M^2\sinh^2(y)}{M\cosh(y)}\exp\left(-\frac{M}{T}\cosh(y)\right) = 4\pi M^2\int dy\,\sinh^2(y)\exp\left(-Z\,\cosh(y)\right) \tag{6.38}$$

with $Z = \frac{M}{T}$.
The modified Bessel function of the 2. kind is defined as

$$K_M(Z) = \int_0^\infty dy\cosh(My)\exp(-Z\cosh(y)). \tag{6.39}$$

Integration by parts gives

$$K_M(Z) = \underbrace{\frac{1}{M}\sinh(My)\exp(-Z\cosh(y))\Big|_{y=0}^{\infty}}_{=0} - \int dy\,\frac{1}{M}\sinh(My)\cdot(-Z)\sinh(y)\exp(-Z\cosh(y)) \tag{6.40}$$

$$= \int dy\,\frac{Z}{M}\sinh(My)\sinh(y)\exp(-Z\cosh(y)), \tag{6.41}$$

thus, the last integral in equation (6.38) can be identified with $\frac{1}{Z}K_1(Z)$.

$$\int \frac{d^3q}{q_0}\exp(-q_0/T) = 4\pi\,M^2\frac{1}{Z}\,K_1(Z) = 4\pi\,M^2\frac{T}{M}\,K_1(M/T) \tag{6.42}$$

For $T \ll M$ the function K_1 can be approximated by $K_1(M/T) \to \sqrt{\frac{\pi T}{2M}}\exp(-M/T)$. This gives the desired relation between equation (6.34) and (6.35)

$$\int \frac{d^3q}{q_0}\exp(-q_0/T) = 4\pi M^2\frac{T}{M}\sqrt{\frac{\pi T}{2M}}\exp(-M/T) = \text{const.}\frac{1}{M}\,(MT)^{3/2}\exp(-M/T). \tag{6.43}$$

Bibliography

[1] B. Friman *et al.*, "The CBM physics book: Compressed baryonic matter in laboratory experiments," *Lect. Notes Phys.* **814** (2011) 1–980.

[2] P. Braun-Munzinger and J. Wambach, "The Phase Diagram of Strongly-Interacting Matter," *Rev. Mod. Phys.* **81** (2009) 1031–1050, arXiv:0801.4256 [hep-ph].

[3] R. Rapp and J. Wambach, "Chiral symmetry restoration and dileptons in relativistic heavy ion collisions," *Adv. Nucl. Phys.* **25** (2000) 1, arXiv:hep-ph/9909229 [hep-ph].

[4] R. Rapp, J. Wambach, and H. van Hees, "The Chiral Restoration Transition of QCD and Low Mass Dileptons," *Landau-Bornstein* **23** (2010) 134, arXiv:0901.3289 [hep-ph].

[5] S. Leupold, V. Metag, and U. Mosel, "Hadrons in strongly interacting matter," *Int. J. Mod. Phys.* **E 19** (2010) 147–224, arXiv:0907.2388v2 [nucl-th].

[6] V. Koch, "Introduction to chiral symmetry," arXiv:nucl-th/9512029 [nucl-th].

[7] **ATLAS** Collaboration, G. Aad *et al.*, "Observation of a new particle in the search for the Standard Model Higgs boson with the ATLAS detector at the LHC," *Phys. Lett.* **B 716** (2012) 1–29, arXiv:1207.7214 [hep-ex].

[8] **CMS** Collaboration, S. Chatrchyan *et al.*, "Observation of a new boson at a mass of 125 GeV with the CMS experiment at the LHC," *Phys. Lett.* **B 716** (2012) 30–61, arXiv:1207.7235 [hep-ex].

[9] A. Purcell, "Go on a particle quest at the first CERN hackfest," 2012 (accessed October 6, 2015). http://www.isgtw.org/sites/default/files/Standard_model_infographic.png.

[10] **Particle Data Group** Collaboration, K. Olive *et al.*, "Review of Particle Physics," *Chin. Phys.* **C 38** (2014) 090001.

[11] M. Gell-Mann, R. J. Oakes, and B. Renner, "Behavior of current divergences under SU(3) x SU(3)," *Phys. Rev.* **175** (1968) 2195–2199.

[12] **ALEPH** Collaboration, R. Barate *et al.*, "Measurement of the spectral functions of axial - vector hadronic tau decays and determination of alpha(S)(M**2(tau))," *Eur. Phys. J.* **C 4** (1998) 409–431.

[13] **OPAL** Collaboration, K. Ackerstaff *et al.*, "Measurement of the strong coupling constant alpha(s) and the vector and axial vector spectral functions in hadronic tau decays," *Eur. Phys. J.* **C 7** (1999) 571–593, arXiv:hep-ex/9808019 [hep-ex].

[14] S. Weinberg, "Precise relations between the spectra of vector and axial vector mesons," *Phys. Rev. Lett.* **18** (1967) 507–509.

[15] P. M. Hohler and R. Rapp, "Is ρ-Meson Melting Compatible with Chiral Restoration?," *Phys. Lett.* **B 731** (2014) 103–109, arXiv:1311.2921 [hep-ph].

[16] E. V. Shuryak, "Quark-Gluon Plasma and Hadronic Production of Leptons, Photons and Psions," *Phys. Lett.* **B 78** (1978) 150. [Yad. Fiz.28,796(1978)].

[17] **BRAHMS** Collaboration, I. Arsene *et al.*, "Quark gluon plasma and color glass condensate at RHIC? The Perspective from the BRAHMS experiment," *Nucl. Phys.* **A 757** (2005) 1–27, arXiv:nucl-ex/0410020 [nucl-ex].

[18] **PHOBOS** Collaboration, B. Back *et al.*, "The PHOBOS perspective on discoveries at RHIC," *Nucl. Phys.* **A 757** (2005) 28–101, arXiv:nucl-ex/0410022 [nucl-ex].

[19] **STAR** Collaboration, J. Adams *et al.*, "Experimental and theoretical challenges in the search for the quark gluon plasma: The STAR Collaboration's critical assessment of the evidence from RHIC collisions," *Nucl. Phys.* **A 757** (2005) 102–183, arXiv:nucl-ex/0501009 [nucl-ex].

[20] **PHENIX** Collaboration, K. Adcox *et al.*, "Formation of dense partonic matter in relativistic nucleus-nucleus collisions at RHIC: Experimental evaluation by the PHENIX collaboration," *Nucl. Phys.* **A 757** (2005) 184–283, arXiv:nucl-ex/0410003 [nucl-ex].

[21] **ALICE** Collaboration, K. Aamodt *et al.*, "Elliptic flow of charged particles in Pb-Pb collisions at 2.76 TeV," *Phys. Rev. Lett.* **105** (2010) 252302, arXiv:1011.3914 [nucl-ex].

[22] **ALICE** Collaboration, J. Schukraft, "ALICE results from the first Pb-Pb run at the CERN LHC," *J. Phys.* **G 38** (2011) 124003, arXiv:1106.5620 [hep-ex].

[23] N. Cabibbo and G. Parisi, "Exponential Hadronic Spectrum and Quark Liberation," *Phys. Lett.* **B 59** (1975) 67–69.

[24] J. C. Collins and M. Perry, "Superdense Matter: Neutrons Or Asymptotically Free Quarks?," *Phys. Rev. Lett.* **34** (1975) 1353.

[25] K. Fukushima and T. Hatsuda, "The phase diagram of dense QCD," *Rept. Prog. Phys.* **74** (2011) 014001, arXiv:1005.4814 [hep-ph].

[26] L. McLerran, "Quarkyonic Matter and the Phase Diagram of QCD," arXiv:0808.1057 [hep-ph].

[27] L. McLerran, K. Redlich, and C. Sasaki, "Quarkyonic Matter and Chiral Symmetry Breaking," *Nucl. Phys.* **A 824** (2009) 86–100, arXiv:0812.3585 [hep-ph].

[28] A. Andronic *et al.*, "Hadron Production in Ultra-relativistic Nuclear Collisions: Quarkyonic Matter and a Triple Point in the Phase Diagram of QCD," *Nucl. Phys.* **A 837** (2010) 65–86, arXiv:0911.4806 [hep-ph].

[29] M. G. Alford *et al.*, "Color superconductivity in dense quark matter," *Rev. Mod. Phys.* **80** (2008) 1455–1515, arXiv:0709.4635 [hep-ph].

[30] Y. Nambu and G. Jona-Lasinio, "Dynamical Model of Elementary Particles Based on an Analogy with Superconductivity. 1.," *Phys. Rev.* **122** (1961) 345–358.

[31] Y. Nambu and G. Jona-Lasinio, "Dynamical Model of Elementary Particles Based on an Analogy with Superconductivity. 2.," *Phys. Rev.* **124** (1961) 246–254.

[32] B. Schäfer and J. Wambach, *private communication*.

[33] **HADES** Collaboration, T. Galatyuk, "HADES overview," *Nucl. Phys.* **A 931** (2014) 41–51.

[34] G. Brown and M. Rho, "Scaling effective Lagrangians in a dense medium," *Phys. Rev. Lett.* **66** (1991) 2720–2723.

[35] R. Rapp, G. Chanfray, and J. Wambach, "Rho meson propagation and dilepton enhancement in hot hadronic matter," *Nucl. Phys.* **A 617** (1997) 472–495, arXiv:hep-ph/9702210 [hep-ph].

[36] **NA60** Collaboration, R. Arnaldi *et al.*, "First measurement of the rho spectral function in high-energy nuclear collisions," *Phys. Rev. Lett.* **96** (2006) 162302, arXiv:nucl-ex/0605007 [nucl-ex].

[37] MADAI.us, "Model and Data Analysis Initiative," 2015 (accessed September 18, 2015). https://madai-public.cs.unc.edu/visualization/heavy-ion-collisions/.

[38] J. Cleymans and H. Satz, "Thermal hadron production in high-energy heavy ion collisions," *Z. Phys.* **C 57** (1993) 135–148, arXiv:hep-ph/9207204 [hep-ph].

[39] J. Cleymans, H. Oeschler, K. Redlich, and S. Wheaton, "Comparison of chemical freeze-out criteria in heavy-ion collisions," *Phys. Rev.* **C 73** (2006) 034905, arXiv:hep-ph/0511094 [hep-ph].

[40] A. Andronic, P. Braun-Munzinger, and J. Stachel, "Thermal hadron production in relativistic nuclear collisions: The Hadron mass spectrum, the horn, and the QCD phase transition," *Phys. Lett.* **B 673** (2009) 142–145, arXiv:0812.1186 [nucl-th]. [Erratum: Phys. Lett. B 678 (2009) 516].

[41] J. Cleymans and K. Redlich, "Chemical and thermal freezeout parameters from 1-A/GeV to 200-A/GeV," *Phys. Rev.* **C 60** (1999) 054908, arXiv:nucl-th/9903063 [nucl-th].

[42] **FOPI** Collaboration, X. Lopez *et al.*, "Sub-threshold production of Sigma(1385) baryons in Al + Al collisions at 1.9-A-GeV," *Phys. Rev.* **C 76** no. 052203, (2007) , arXiv:0710.5007 [nucl-ex].

[43] **HADES** Collaboration, G. Agakishiev *et al.*, "Hyperon production in Ar+KCl collisions at 1.76A GeV," *Eur. Phys. J.* **A 47** (2011) 21, arXiv:1010.1675 [nucl-ex].

[44] **HADES** Collaboration, M. Lorenz, "Reviewing hadron production at SIS energies featuring the new HADES *Au + Au* data," *Nucl. Phys.* **A 931** (2014) 785–789.

[45] Z. Fodor and S. D. Katz, "Critical point of QCD at finite T and mu, lattice results for physical quark masses," *JHEP* **04** (2004) 050, arXiv:hep-lat/0402006 [hep-lat].

[46] **NA60** Collaboration, H. J. Specht, "Thermal Dileptons from Hot and Dense Strongly Interacting Matter," *AIP Conf. Proc.* **1322** (2010) 1–10, arXiv:1011.0615 [nucl-ex].

[47] **STAR** Collaboration, X. Luo, "Energy Dependence of Moments of Net-Proton and Net-Charge Multiplicity Distributions at STAR," *PoS* **CPOD2014** (2014) 019, arXiv:1503.02558 [nucl-ex].

[48] E. L. Feinberg, "Direct Production of Photons and Dileptons in Thermodynamical Models of Multiple Hadron Production," *Nuovo Cim.* **A 34** (1976) 391.

[49] A. Drees, "Dileptons and Photons at RHIC Energies," *Nucl. Phys.* **A 830** (2009) 435C–442C, arXiv:0909.4976 [nucl-ex].

[50] R. Rapp and H. van Hees, "Thermal Dileptons as Fireball Thermometer and Chronometer," arXiv:1411.4612 [hep-ph].

[51] **CERES** Collaboration, G. Agakichiev *et al.*, "Enhanced production of low mass electron pairs in 200 GeV/u S - Au collisions at the CERN SPS," *Phys. Rev. Lett.* **75** (1995) 1272–1275.

[52] **CERES** Collaboration, G. Agakishiev *et al.*, "Low mass e+ e- pair production in 158/A-GeV Pb - Au collisions at the CERN SPS, its dependence on multiplicity and transverse momentum," *Phys. Lett.* **B 422** (1998) 405–412, arXiv:nucl-ex/9712008 [nucl-ex].

[53] **CERES** Collaboration, G. Agakichiev *et al.*, "e+ e- pair production in Pb - Au collisions at 158-GeV per nucleon," *Eur. Phys. J.* **C 41** (2005) 475–513, arXiv:nucl-ex/0506002 [nucl-ex].

[54] **CERES** Collaboration, D. Adamova *et al.*, "Modification of the rho-meson detected by low-mass electron-positron pairs in central Pb-Au collisions at 158 AGeV/c," *Phys. Lett.* **B 666** (2008) 425–429, arXiv:nucl-ex/0611022 [nucl-ex].

[55] **CERES** Collaboration, D. Adamova *et al.*, "Enhanced production of low mass electron pairs in 40 AGeV Pb - Au collisions at the CERN SPS," *Phys. Rev. Lett.* **91** (2003) 042301, arXiv:nucl-ex/0209024 [nucl-ex].

[56] G.-Q. Li, C. Ko, and G. Brown, "Enhancement of low mass dileptons in heavy ion collisions," *Phys. Rev. Lett.* **75** (1995) 4007–4010, arXiv:nucl-th/9504025 [nucl-th].

[57] G.-Q. Li, C. Ko, and G. Brown, "Effects of in-medium vector meson masses on low mass dileptons from SPS heavy ion collisions," *Nucl. Phys.* **A 606** (1996) 568–606, arXiv:nucl-th/9608040 [nucl-th].

[58] R. Rapp and J. Wambach, "Low mass dileptons at the CERN SPS: Evidence for chiral restoration?," *Eur. Phys. J.* **A 6** (1999) 415–420, arXiv:hep-ph/9907502 [hep-ph].

[59] **NA60** Collaboration, S. Damjanovic *et al.*, "NA60 results on the rho spectral function in In-In collisions," *Nucl. Phys.* **A 783** (2007) 327–334, arXiv:nucl-ex/0701015 [nucl-ex].

[60] R. Rapp, "Dileptons and Medium Effects in Heavy-Ion Collisions," *Nucl. Phys.* **A 782** (2007) 275–282, arXiv:nucl-th/0608022 [nucl-th].

[61] R. Rapp, "In-Medium Vector Mesons, Dileptons and Chiral Restoration," *AIP Conf. Proc.* **1322** (2010) 55–63, arXiv:1010.1719 [nucl-th].

[62] **STAR** Collaboration, F. Geurts, "Dilepton Measurements at STAR," *J. Phys. Conf. Ser.* **458** (2013) 012016, arXiv:1305.5447 [nucl-ex].

[63] **STAR** Collaboration, L. Adamczyk *et al.*, "Dielectron Mass Spectra from Au+Au Collisions at $\sqrt{s_{NN}}$ = 200 GeV," *Phys. Rev. Lett.* **113** (2014) 022301, arXiv:1312.7397 [hep-ex].

[64] **STAR** Collaboration, L. Adamczyk *et al.*, "Measurements of Dielectron Production in Au+Au Collisions at $\sqrt{s_{NN}}$ = 200 GeV from the STAR Experiment," *Phys. Rev.* **C 92** no. 2, (2015) 024912, arXiv:1504.01317 [hep-ex].

[65] **STAR** Collaboration, P. Huck, "Beam Energy Dependence of Dielectron Production in Au + Au Collisions from STAR at RHIC," *Nucl. Phys.* **A 931** (2014) 659–664, arXiv:1409.5675 [nucl-ex].

[66] **STAR** Collaboration, L. Adamczyk *et al.*, "Energy dependence of acceptance-corrected dielectron excess mass spectrum at mid-rapidity in Au+Au collisions at $\sqrt{s_{NN}}$ = 19.6 and 200 GeV," *Phys. Lett.* **B 750** (2015) 64–71, arXiv:1501.05341 [hep-ex].

[67] H. van Hees and R. Rapp, "Dilepton Radiation at the CERN Super Proton Synchrotron," *Nucl. Phys.* **A 806** (2008) 339–387, arXiv:0711.3444 [hep-ph].

[68] R. Rapp, "Dilepton Spectroscopy of QCD Matter at Collider Energies," *Adv. High Energy Phys.* **2013** (2013) 148253, arXiv:1304.2309 [hep-ph].

[69] **PHENIX** Collaboration, A. Adare *et al.*, "Detailed measurement of the e^+e^- pair continuum in $p+p$ and Au+Au collisions at $\sqrt{s_{NN}}$ = 200 GeV and implications for direct photon production," *Phys. Rev.* **C 81** (2010) 034911, arXiv:0912.0244 [nucl-ex].

[70] **PHENIX** Collaboration, A. Adare *et al.*, "Dielectron production in Au+Au collisions at $\sqrt{s_{NN}}$=200 GeV," arXiv:1509.04667 [nucl-ex].

[71] **DLS** Collaboration, R. Porter *et al.*, "Dielectron cross-section measurements in nucleus-nucleus reactions at 1 AGeV," *Phys. Rev. Lett.* **79** (1997) 1229–1232, arXiv:nucl-ex/9703001 [nucl-ex].

[72] **HADES** Collaboration, G. Agakichiev *et al.*, "Dielectron production in C-12+C-12 collisions at 2 AGeV with HADES," *Phys. Rev. Lett.* **98** (2007) 052302, arXiv:nucl-ex/0608031 [nucl-ex].

[73] **HADES** Collaboration, G. Agakishiev *et al.*, "Study of dielectron production in C+C collisions at 1 AGeV," *Phys. Lett.* **B 663** (2008) 43–48, arXiv:0711.4281 [nucl-ex].

[74] **HADES** Collaboration, G. Agakishiev *et al.*, "Origin of the low-mass electron pair excess in light nucleus-nucleus collisions," *Phys. Lett.* **B 690** (2010) 118–122, arXiv:0910.5875 [nucl-ex].

[75] **HADES** Collaboration, G. Agakishiev *et al.*, "Dielectron production in Ar+KCl collisions at 1.76A GeV," *Phys. Rev.* **C 84** (2011) 014902, arXiv:1103.0876 [nucl-ex].

[76] J. Randrup and J. Cleymans, "Maximum freeze-out baryon density in nuclear collisions," *Phys. Rev.* **C 74** (2006) 047901, arXiv:hep-ph/0607065 [hep-ph].

[77] U. W. Heinz and K. S. Lee, "Dileptons from rho mesons as a fast clock for heavy ion collisions," *Nucl. Phys.* **A 544** (1992) 503–508.

[78] **NA60** Collaboration, R. Shahoyan, "Evidence for the production of thermal dimuons with masses above 1-GeV/c**2 in 158A-GeV In-In collisions," *Nucl. Phys.* **A 827** (2009) 353C–355C. [,507(2009)].

[79] **HADES** Collaboration, G. Agakishiev *et al.*, "The High-Acceptance Dielectron Spectrometer HADES," *Eur. Phys. J.* **A 41** (2009) 243–277, arXiv:0902.3478 [nucl-ex].

[80] **CBM** Collaboration, *Progress Report 2013*. https://www-alt.gsi.de/documents/DOC-2014-Mar-16-1.pdf.

[81] P. Sellheim, "Dielektronenrekonstruktion in Au+Au Kollisionen bei 1,23 GeV/u mit HADES," master's thesis, Goethe-Universität Frankfurt(Main), Frankfurt(Main), 2013. https://hades.gsi.de/sites/default/files/web/media/documents/thesis/Master/Dielektronenrekonstruktion_in_Au+Au_Kollisionen_bei_1,23_AGeV_mit_HADES_P_Sellheim.pdf.

[82] T. Galatyuk, *Di-electron spectroscopy in HADES and CBM: from p + p and n + p collisions at GSI to Au + Au collisions at FAIR*. Phd thesis, Goethe-Universität Frankfurt(Main), Frankfurt(Main), 2009. https://hades.gsi.de/sites/default/files/web/media/documents/thesis/PhD/Di-electron_spectroscopy_in_HADES_and_CBM_from_p+p_and_n+p_collisions_at_GSI_to_Au+AU_collisions_at_FAIR_T_Galatyuk.pdf.

[83] **HADES** Collaboration, W. Czyzycki *et al.*, "Electromagnetic Calorimeter for HADES," arXiv:1109.5550 [nucl-ex].

[84] A. Rost, "Optimising the KISS readout concept for calorimeter type detectors," bachelor's thesis, Technische Universität Darmstadt, Darmstadt, 2013. https://hades.gsi.de/sites/default/files/web/media/documents/thesis/Bachelor/Optimising_the_KISS_readout_concept_for_calorimeter_type_detectors_Adrian_Rost_2014-Nov.pdf.

[85] CERN, Geneva, *GEANT3 - Detector description and simulation tool, CERN Program Library Long Write-up W5013*.

[86] **GEANT4** Collaboration, S. Agostinelli *et al.*, "GEANT4: A Simulation toolkit," *Nucl. Instrum. Meth.* **A 506** (2003) 250–303.

[87] I. Frohlich *et al.*, "Pluto: A Monte Carlo Simulation Tool for Hadronic Physics," *PoS* **ACAT2007** (2007) 076, arXiv:0708.2382 [nucl-ex].

[88] I. Frohlich *et al.*, "Design of the Pluto Event Generator," *J. Phys. Conf. Ser.* **219** (2010) 032039, arXiv:0905.2568 [nucl-ex].

[89] "Root - an object oriented data analysis framework." http://root.cern.ch/.

[90] R. Rapp, *private communication*.

[91] O. Buss, T. Gaitanos, K. Gallmeister, H. van Hees, M. Kaskulov, O. Lalakulich, A. B. Larionov, T. Leitner, J. Weil, and U. Mosel, "Transport-theoretical Description of Nuclear Reactions," *Phys. Rept.* **512** (2012) 1–124, arXiv:1106.1344 [hep-ph].

[92] W. Ehehalt and W. Cassing, "Relativistic transport approach for nucleus nucleus collisions from SIS to SPS energies," *Nucl. Phys.* **A 602** (1996) 449–486.

[93] W. Cassing and E. L. Bratkovskaya, "Hadronic and electromagnetic probes of hot and dense nuclear matter," *Phys. Rept.* **308** (1999) 65–233.

[94] S. Bass *et al.*, "Microscopic models for ultrarelativistic heavy ion collisions," *Prog. Part. Nucl. Phys.* **41** (1998) 255–369, arXiv:nucl-th/9803035 [nucl-th].

[95] M. Bleicher *et al.*, "Relativistic hadron–hadron collisions in the ultra-relativistic quantum molecular dynamics model," *J. Phys. G: Nucl. Part. Phys.* **25** no. 9, (1999) 1859–1896.

[96] K. Schmidt *et al.*, "Production and evolution path of dileptons at energies accessible to the HADES detector," *Phys. Rev.* **C 79** (2009) 064908, arXiv:0811.4073 [nucl-th].

[97] S. Endres and M. Bleicher, "Dilepton production at SIS energies with the UrQMD model," *J. Phys. Conf. Ser.* **426** (2013) 012033.

[98] J. Weil and U. Mosel, "Dilepton production at SIS energies with the GiBUU transport model," *J. Phys. Conf. Ser.* **426** (2013) 012035, arXiv:1211.3761 [nucl-th].

[99] E. L. Bratkovskaya and W. Cassing, "Dilepton production and off-shell transport dynamics at SIS energies," *Nucl. Phys.* **A 807** (2008) 214–250, arXiv:0712.0635 [nucl-th].

[100] O. Buss *et al.*, "Transport-theoretical Description of Nuclear Reactions," *Phys. Rept.* **512** (2012) 1–124, arXiv:1106.1344 [hep-ph].

[101] H. W. Barz *et al.*, "Propagation of vector-meson spectral-functions in a BUU type transport model: Application to di-electron production," *Open Nucl. Part. Phys. J.* **3** (2010) 1–15, arXiv:0910.1541 [nucl-th].

[102] R. Rapp, "Theory of Soft Electromagnetic Emission in Heavy-Ion Collisions," *Acta Phys. Polon.* **B 42** (2011) 2823–2852, arXiv:1110.4345 [nucl-th].

[103] L. D. McLerran and T. Toimela, "Photon and Dilepton Emission from the Quark - Gluon Plasma: Some General Considerations," *Phys. Rev.* **D 31** (1985) 545.

[104] J. J. Sakurai, *Currents and Mesons*. University of Chicago Press, Chicago, 1969.

[105] H. T. Ding *et al.*, "Thermal dilepton rate and electrical conductivity: An analysis of vector current correlation functions in quenched lattice QCD," *Phys. Rev.* **D 83** (2011) 034504, arXiv:1012.4963 [hep-lat].

[106] J. I. Kapusta, P. Lichard, and D. Seibert, "High-energy photons from quark - gluon plasma versus hot hadronic gas," *Phys. Rev.* **D 44** (1991) 2774–2788. [Erratum: Phys. Rev.D47,4171(1993)].

[107] E. Braaten, R. D. Pisarski, and T.-C. Yuan, "Production of Soft Dileptons in the Quark - Gluon Plasma," *Phys. Rev. Lett.* **64** (1990) 2242.

[108] B. Schenke, "Music single event isothermal contours," 2010 (accessed September 18, 2015). http://quark.phy.bnl.gov/~bschenke/.

[109] P. Huovinen, M. Belkacem, P. J. Ellis, and J. I. Kapusta, "Dileptons and photons from coarse grained microscopic dynamics and hydrodynamics compared to experimental data," *Phys. Rev.* **C 66** (2002) 014903, arXiv:nucl-th/0203023 [nucl-th].

[110] J. I. Kapusta, "Dileptons and photons from coarse grained microscopic dynamics and hydrodynamics compared to experimental data," *Nucl. Phys.* **A 715** (2003) 709–712, arXiv:nucl-th/0210032 [nucl-th].

[111] S. Endres *et al.*, "Coarse-graining approach for dilepton production at energies available at the CERN Super Proton Synchrotron," *Phys. Rev.* **C 91** no. 5, (2015) 054911, arXiv:1412.1965 [nucl-th].

[112] S. Endres *et al.*, "Dilepton production and reaction dynamics in heavy-ion collisions at SIS energies from coarse-grained transport simulations," *Phys. Rev.* **C 92** no. 1, (2015) 014911, arXiv:1505.06131 [nucl-th].

[113] C. Behnke, "Development of an event generator for dilepton production in heavy ion collisions in the SIS energy regime," master's thesis, Goethe-Universität Frankfurt(Main), Frankfurt(Main), 2011. unpublished.

[114] E. Santini, J. Steinheimer, M. Bleicher, and S. Schramm, "Dimuon radiation at the CERN SPS within a (3+1)d hydrodynamic+cascade model," *Phys. Rev.* **C 84** (2011) 014901, arXiv:1102.4574 [nucl-th].

[115] S. Vogel *et al.*, "How sensitive are di-leptons from rho mesons to the high baryon density region?," *Phys. Rev.* **C 78** (2008) 044909, arXiv:0710.4463 [hep-ph].

[116] D. Oliinychenko, P. Huovinen, and H. Petersen, "Systematic Investigation of Negative Cooper-Frye Contributions in Heavy Ion Collisions Using Coarse-grained Molecular Dynamics," *Phys. Rev.* **C 91** no. 2, (2015) 024906, arXiv:1411.3912 [nucl-th].

[117] D. Oliinychenko, P. Huovinen, and H. Petersen, "Cooper-Frye Negative Contributions in a Coarse-Grained Transport Approach," *J. Phys. Conf. Ser.* **599** no. 1, (2015) 012017, arXiv:1412.2020 [nucl-th].

[118] D. Oliinychenko and H. Petersen, "Deviations of the Energy-Momentum Tensor from Equilibrium in the Initial State for Hydrodynamics from Transport Approaches," arXiv:1508.04378 [nucl-th].

[119] M. Dey, V. L. Eletsky, and B. L. Ioffe, "Mixing of vector and axial mesons at finite temperature: an Indication towards chiral symmetry restoration," *Phys. Lett.* **B 252** (1990) 620–624.

List of Figures

Acknowledgments

At this point I'd like to say thanks to everybody who contributed in one way or the other in the development of this project:

I would like to thankfully acknowledge my thesis advisor, Prof. Dr. Tetyana Galatyuk, who sparked my interest in electromagnetic probes in heavy-ion physics and provided me the opportunity to join her research group with such an interesting project. I could not have made a better choice. Her enthusiasm is a source of inspiration and her advices triggered many interesting discussions. Thanks for converting me into an experimentalist ;)

I am also extremely grateful to Prof. Dr. Joachim Stroth for many discussions and ideas that helped to shape the project.

A special thanks goes to Prof. Dr. Ralf Rapp for the nice time in his group during my stay at the Texas A&M university in College Station. Gig 'em Aggies! The discussions with him and his postdoc Dr. Paul M. Hohler lead to many insights and a continuing collaboration. I also would like to thank him for providing the in-medium ρ and QGP contributions to the thermal spectra for $Au + Au$ at 20 AGeV and the parametrization of the Rapp-Wambach spectral function.

I'd like to thank Dr. Ingo Fröhlich for providing the macro to sample the dileptons in Pluto according to the input histograms produced with this framework.

For the preparation of the freeze-out contributions to the Pluto cocktail at 25 AGeV, I thank Erik Krebs.

Many thanks to Dr. Jochen Markert for the help with software, like ROOT and Pluto, especially in the beginning of my master and many interesting coffee breaks after lunch at GSI.

For the nice hours and lots of discussions, not only about physics, in our offices at GSI and TU Darmstadt, I would like to thank the other members of the ViP-QM group, namely Georgy Kornakov, Adrian Rost, Frédéric Kornas, Federico Scozzi, Szymon Harabasz and Malgorzata Gumberidze.

For the great time on the collaboration meetings, my thanks goes to the young members and all collaborators in HADES and CBM.

For all the support, encouragement, love and advice which made me to the person I am, I gratefully thank my whole family, especially my mom, my dad, and my girlfriend.

Erklärung zur Master-Thesis

Hiermit versichere ich, die vorliegende Master-Thesis ohne Hilfe Dritter nur mit den angegebenen Quellen und Hilfsmitteln angefertigt zu haben. Alle Stellen, die aus Quellen entnommen wurden, sind als solche kenntlich gemacht. Diese Arbeit hat in gleicher oder ähnlicher Form noch keiner Prüfungsbehörde vorgelegen.

Darmstadt, den 30. Oktober 2015

_____

(Florian Seck)